Durham E-Theses

Combined use of powder diffraction and magic-angle spinning NMR to structural chemistry

King, Ian James

Combined Use of Powder Diffraction and Magic-Angle

Spinning NMR to Structural Chemistry

by

Ian James King M.Sci. (Hons. Dunelm)

Grey College

University of Durham

A thesis submitted in partial fulfilment of the requirements for the degree of Doctor of Philosophy

Department of Chemistry   ~ 7 JUL 2003

University of Durham

2003

Summary

A range of 1D and 2D MAS NMR experiments have been carried out in conjunction with X-ray diffraction experiments on a number of materials from the AM_2O_7 family, which exhibit the unusual phenomenon of negative thermal expansion. It has been shown that ZrP_2O_7 and HfP_2O_7 exist with space group $Pbca$ rather than $Pa\bar{3}$ as proposed in the literature, and a full structure solution has been possible for ZrP_2O_7 from a combination of NMR and X-ray and neutron powder diffraction. 2D MAS NMR has been used to differentiate at least 108 unique phosphorus sites within the asymmetric unit of SnP_2O_7, supporting a recent powder diffraction study presented in the literature. PbP_2O_7 has been shown, by NMR, to exist as an incommensurate phase at room temperature. ZrW_2O_8, a material which also shows negative thermal expansion, has been studied here primarily with variable-temperature ^{17}O MAS NMR. The results presented shed important new light on oxygen migration processes occurring at the α/β-phase transition of this material. A full structure solution is presented for 2-[4-(2-hydroxy-ethylamino)-6-phenylamino-[1,3,5]triazin-2-ylamino]-ethanol from powder X-ray data, an organic material investigated as part of a study of ink-jet-dyes.

Memorandum

The research presented in this thesis has been carried out in the department of Chemistry, University of Durham and CRMHT-CNRS, Orléans, France, between October 1999 and September 2002. It is the original work of the author unless otherwise stated. None of this work has been submitted for any other degree.

Acknowledgements

I would like to acknowledge the following people for the help, patience and assistance over the course of my Ph.D.

Firstly I would like to thank my two supervisors in Durham, Prof. Robin K. Harris, and Dr. John S. O. Evans. First, Robin for believing in the first instance that I was capable of doing a Ph.D, and for his general help, assistance and vast knowledge of NMR. Second, John for his advice and support during my Ph.D, and for explaining/answering some of my more stupid questions.

For financial support I must thank the EPSRC, CNRS and the EU.

I also owe a very huge thanks to Prof. Dominique Massiot and Dr. Franck Fayon, and everyone else at the CRMHT-CNRS, Orléans, France. Franck and Dominique gave me a great deal of their time and lots of good advice, for which I am extremely thankful. Special mentions must go to Ioana & Stéphane for finding me a place to live, to Franck for his help and hospitality outside of work and the two Jameses for being around.

My Ph.D wouldn't have been achievable without the other members in the groups who were always around with help, advice and support. I have already mentioned the group in France, but the people in Durham were the people who had to put up with me the most. So a huge thanks to Simon (you are far too clever, thanks for putting up with me for three years), Neil (and I thought I did nothing!), Richard (I know we had our differences at times, but thanks, you were a great help), Clare (stay mad, thanks for being supportive), Coxy (you were only here for a year!), the fourth year project students and of course the NMR group. I must give special thanks to David for all his help and running occasional samples.

I would like to thank Dr. Angelika Sebald, Dr. Mark E. Smith and Xavier Helluy, who have been a source of some very useful discussions during the course of my Ph.D.

I should thank my various housemates over the three years as well as all my friends in Durham: a special thanks goes to the New Inn 'locals/community', Al, Jacquie, Dave E, Brian, Jacko, Alex, Simon Jewitt, Damo, Cameron, Kelly L., Kelly F., Troll, Trollet, Mark & Nicky, Weeman, Dark Horse, Perky, Tony (or Dr. C!!), Dave Hocking and, of course, Katie, thanks guys, you'll never know how much I appreciate all of you; on the subject of the New Inn, a huge thanks to Martin, Lynn and all the New Inn staff, especially those I've worked with; the Woodman pool team, especially Leigh, Ian B, Schaz and Christina. Outside of Durham, there have been a number of friends who have known me since my first days at University, plus one or two others. You have all stuck with me, been good friends, and given good advice, and just generally been

great/there for me, so a huge thanks to you lot; AJ, Andy J, Scally, Pelham, Jon G, Jon May, Tarky, Steph, Rosie, Nigel, Denver and Cat.

Lastly, but certainly not least, my family, Helen, Margaret, Grandma (and Grandpa, always an inspiration, even from beyond the grave!), Bill, James and Chloe, and especially my parents, Ken and Fran. Thanks mum, you made me keep going even when I wanted to quit, and have been a help beyond anything I could have asked for. I love you all.

"...follow the rainbows in your mind..."

Rainbows, Spellbound, Alex & I, 1999

Table of Contents

List of Figures and Tables

Figures

Tables

Chapter 1

Introduction

The field of structural chemistry is an interesting and diverse subject area, ranging from contemporary computational modelling to 'traditional' crystallographic techniques. Advances in this field have allowed increasingly complex structures to be solved, allowing a greater understanding of a vast array of materials. Such understanding has been crucial in developing a member of technologically important materials. In this study a number of techniques have been utilised to investigate a range of materials, with the complete structure solutions of both an inorganic and an organic material being presented. Three main topics are covered in this thesis:

i)   A study of the AM_2O_7 family of materials, a number of which exhibit the interesting phenomenon of isotropic negative thermal expansion (NTE) over a relatively large temperature range. This work has employed multiple techniques, including the use of a number of complex 2D solid-state nuclear magnetic resonance (NMR) experiments.

ii)   Variable temperature magic-angle spinning (MAS) ^{17}O NMR studies of the α/β-phase transition of ZrW_2O_8, a material which also exhibits isotropic NTE over a large temperature range. The phase transition involves oxygen migration at unusually low temperatures, and NMR was seen as the ideal method to probe this. The results presented suggest a new mechanism for the phase transition.

iii)   A structure solution of 2-[4-(2-hydroxy-ethylamino)-6-phenylamino-[1,3,5]triazin-2-ylamino]-ethanol from powder X-ray diffraction (XRD) data. At the time of solving this structure it was one of the more complex organic structures to have had its structure determined using the methods presented.

These topics have the common theme of showing how different structural techniques can be used to complement one another, specifically powder XRD and solid-state NMR. The three pieces of work are sufficiently distinct that no overall introduction is given, but rather an introduction and conclusion presented for each chapter. Experimental details are contained in a number of places, including: a general experimental chapter, giving information such as the source of the materials studied; a chapter relating to the 2D MAS NMR experiments used; and information relating to structure solution from powder XRD data.

XRD and NMR are methods that both work well for microcrystalline powdered samples, and that readily complement one another. XRD relies on both local and long-range order, and gives indirect information on the crystallographic asymmetric unit, while NMR relies primarily on the local environment and gives immediate information on the crystallographic asymmetric unit. NMR is especially useful at distinguishing isoelectronic atoms and giving information about disorder within a material and although XRD is also able to provide these bits of information, it can not always do so readily. Both techniques can be used to distinguish polymorphs, amorphous materials and heterogeneous materials.

One of the main reasons for these two techniques being complementary is different timescales they are able to probe: NMR usually probes short time scale effects, although effects over long time periods (e.g. relaxation times) can be probed; XRD usually probes long timescale effect. This is of importance when distinguishing between such things as static and dynamic disorder. NMR can be used to study mutual exchange and give information on molecular level dynamics, neither of which XRD can probe directly. XRD requires a much smaller amount of a sample to study than NMR, which can be a big factor where difficulties arise in preparing large quantities of a sample to be studied (XRD $\geq$ 10 mg, NMR $\geq$ 300 mg).

It is hoped this thesis, in which a number of materials are studied using a range of techniques, will show that studies on the structures of solid materials should not be confined to only one technique, and that a combined approach, is much more powerful.

Chapter 2

Experimental

2.0 Materials Studied

A number of materials were used in this study, all of which were synthesised by others involved in the individual parts of the work presented. The materials and the sources are given in Table 2.1, with references for the synthesis of the material.

Material	Source	Synthesis
ZrP_2O_7	Dr. John S. O. Evans	As per ref. 1
ZrV_2O_7	Dr. John S. O. Evans	As per ref. 2
HfP_2O_7	Malcolm M. Tait	As per ref. 3
SnP_2O_7	Dr. Richard K. B. Gover	As per ref. 4
PbP_2O_7	Joanna Brindley	As per ref. 5
CeP_2O_7	Malcolm M. Tait	As per ref. 3
$Zr^{17}O_2$	Simon Allen	$ZrCl_4 + H_2^{17}O$
$W^{17}O_3$	Simon Allen	$WCl_6 + H_2^{17}O$
$ZrW_2^{17}O_8$	Simon Allen	$Zr^{17}O_2 + W^{17}O_3$
2-[4-(2-hydroxy-ethylamino)-6-phenylamino-[1,3,5]triazin-2-ylamino]-ethanol	Dr. Helen E. Birkett	As per ref. 6
$^nBu_2SnF_2$	1. Dr. Julian Cherryman 2. ABCR-Gelest	As per ref. 7

Table 2.1. Table of the materials used during the studies presented here with the source of the material and a reference for the synthetic route.

Without these materials my studies would not have been possible, so I would like to thank all those mentioned in table 2.1.

2.1 Nuclear Magnetic Resonance (NMR)

2.1.1 General Overview of NMR

Solid-state NMR possesses problems that do not exist for solutions where molecules are rapidly tumbling and anisotropic interactions are averaged. The first major problem is dipolar coupling, which for a heteronuclear AX spin system would give a spectrum for a microcrystalline powder as shown in fig. 2.1, due to the random distribution of molecular orientations in the magnetic field, i.e. these interactions result in substantial line broadening. This interaction arises due to the interactions of magnetic fields around the nuclei that themselves are present due to the presence of the magnetic field of the NMR experiment.
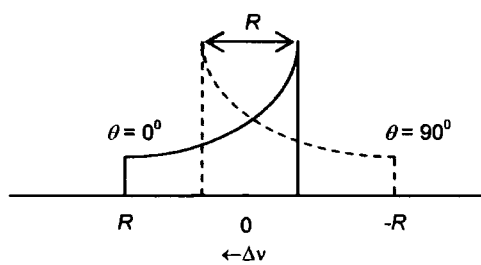
Figure 2.1. A powder pattern arising from dipolar coupling in an AX system, where R is the dipolar coupling constant.

This is removed, using the $^1H/^{13}C$ example here (although dipolar decoupling can be used for other combinations of NMR active nuclei), by applying a second radio frequency to cause the ^1H nuclei to resonate, and hence the ^1H-^{13}C dipolar splittings to collapse, so that a decoupled ^{13}C spectrum is obtained.

A second problem for solids is that the shielding depends on the orientation of the molecule in the magnetic field. In solution rapid tumbling averages this to the isotropic value. This shielding anisotropy, $\Delta\sigma$, also results in line broadening, but it can be shown that, for an axially symmetric system, this broadening depends on eqn. 2.1.

$$\sigma_{zz} = \frac{1}{3}(\sigma_{\parallel} + 2\sigma_{\perp}) + \frac{1}{3}(3\cos^2\theta_{\parallel} - 1)(\sigma_{\parallel} - \sigma_{\perp})$$ (Equation 2.1)

So, if $\theta_{||}$ = 54°44' (the so-called 'magic-angle') $3\cos^2\theta_{||}$-1 reduces to zero. This can also be achieved by averaging, employing rapid sample spinning, known as magic-angle spinning (MAS).[8] (Theoretically this also works to collapse dipolar coupling, but the spinning speeds needed are > 50 kHz which is not commonplace, yet!) Associated with this is the presence of spinning sidebands in the spectrum which arise when shielding effects are not fully averaged. These are symmetrically placed either side of the isotropic resonance, and separated from this by integer multiples of the spinning speed.

The last major problem in the solid state is the spin-lattice relaxation times, which can be very long. After a radio-frequency (r.f.) pulse is applied, $5T_1$ should be left (for a 90° pulse) before applying another pulse to get full relaxation, where T_1 is the time it takes the magnetisation to relax back to its equilibrium position along the z-axis, i.e. along B_0 (the direction of the magnetic field). In some cases T_1 can be an hour or more,[9] and so experiments would be either be very, very long or have a low sensitivity. The problem is overcome, in certain cases, using the method of cross-polarisation (CP) in which, for example, ^{13}C magnetisation is derived from ^1H magnetisation (fig. 2.2). After the ^1H 90° pulse, the ^{13}C channel is switched on and the magnetic field amplitude, B_{1C}, is varied so that the Hartmann-Hahn condition, eqn. 2.2, is fulfilled.

$$\gamma_H B_{1H} = \gamma_C B_{1C}$$ (Equation 2.2)
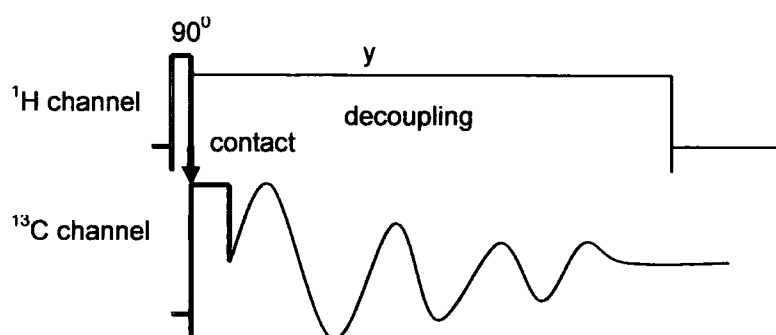
Figure 2.2. Cross-polarisation experiment

This implies the ^1H and ^{13}C frames of reference precess at the same rate with comparable effective energies. This then allows rapid transfer of magnetisation from H to C, which improves the sensitivity by a factor γ_H/γ_C. Moreover, ^1H has a T_1 that is a lot shorter than that of ^{13}C, so the number of transients acquired in a given time is dramatically increased.

These three techniques of dipolar decoupling, MAS and CP are used together, so the spectra of solid-state samples are now comparable to those of solutions, although the line widths are still larger for solids. It is also the case that CP is mainly used only for materials with H in the structure, although it could, for example, be used between ^{31}P and ^{15}N. In the studies presented here, this is only the case for one material, 2-[4-(2-hydroxy-ethylamino)-6-phenylamino-[1,3,5]triazin-2-ylamino]-ethanol (HEB2), for which the NMR spectra were recorded as part of another study,[6] while dipolar decoupling is only used when two NMR accessible nuclei with strong dipolar couplings are present. Again, this was not the case in this study, so only MAS was available as a 'standard' method of spectral enhancement. 2D NMR experiments are increasingly becoming accessible for spectral resolution and to probe the coupling that are accessible via NMR (dipolar-couplings [through-space] and *J*-couplings [through-bond]), and four such experiments are presented and discussed in chapter 3.

2.1.2 Spectrometers

Four solid-state Nuclear Magnetic Resonance (NMR) spectrometers were used in this study, including a Chemagnetics CMX 200, a Varian Infinity Plus 300, a Bruker DSX 300 and a Bruker DSX 400, although the majority of work was carried out on the two Bruker spectrometers. Working at different fields can allow different information to be obtained: at higher fields line separations (in hertz) are usually increased so that couplings are reduced on the parts per million (ppm), chemical shift, scale; more spinning sidebands are obtained within the same shielding anisotropy manifold. This last factor can be a disadvantage, as it may cause spinning sidebands and isotropic peaks to overlap, although this may be overcome by employing increased magic angle spinning (MAS) frequencies. Descriptions are given below for each of the spectrometers used, with a longer description being given for the Bruker DSX 300.

2.1.2.1 Bruker DSX 300

This double-channel wide-bore spectrometer has a magnetic field of 7.04 T, and is controlled by the Bruker XWINNMR software suite. The spectrometer operates using a High Power 1 kW American Microwave Technology (AMT) amplifier, which has a tuning range of 0-200 MHz,

maximum power 'on' time of 20 ms, and is controlled by software. The spectrometer uses probes with pencil rotors (see section 2.1.3). The experimental set-up of the spectrometer is shown in fig. 2.3. The applied frequency pulse from the amplifier passes straight through the crossed diodes and any relevant filters (often used to reduce noise), into the probe. The returning, low-voltage, signal is directed to the pre-amp and receiver, via a $\lambda/4$ cable, by the crossed diodes, and the signal is mixed with a reference frequency allowing the free induction decay (FID) to be recorded in the receiver. An earthed diode is used at the end of the $\lambda/4$ cable to act as a stop.

This spectrometer was used for the majority of the ^{31}P MAS NMR studies in this thesis, as well as for recording a number of ^{17}O MAS spectra at different MAS spin rates.
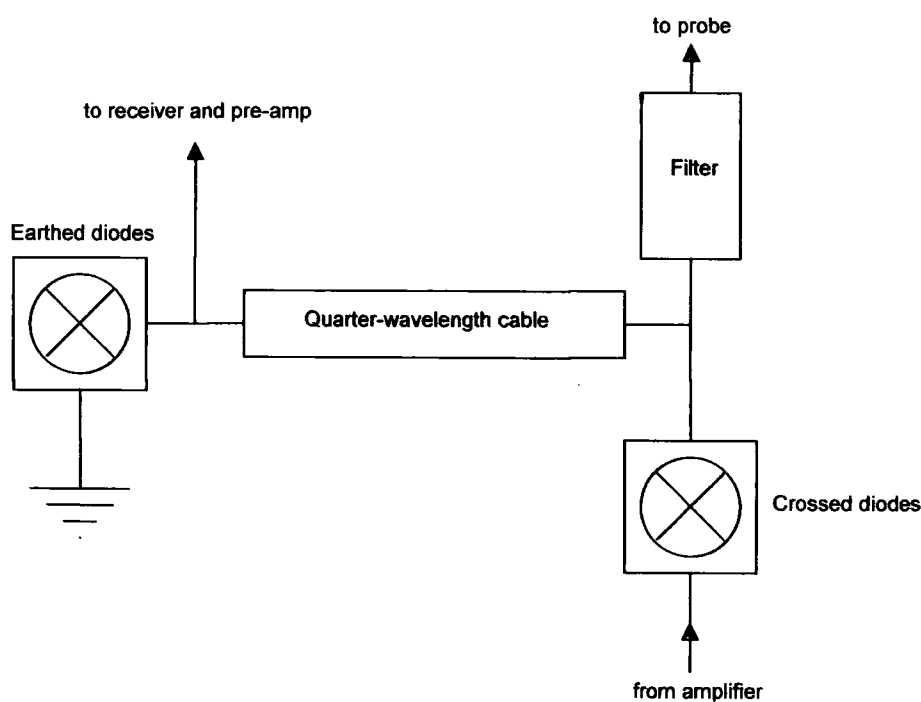
Figure 2.3. Experimental set-up of the Bruker DSX 300.

2.1.2.2 Bruker DSX 400

The Bruker DSX 400 has the same set-up as the Bruker DSX 300, but uses a higher magnetic field, of 9.4 T. This spectrometer was used to record variable temperature (VT) ^{17}O MAS NMR spectra, and a few ^{31}P MAS NMR spectra.

2.1.2.3 Varian Unity Plus 300

This spectrometer is maintained by UDIRL (University of Durham Industrial Research Laboratories) and is also a double-channel, wide-bore system, operating at 7.1 T, with Doty probes being used. A Varian console with VNMR software controls the system. Initial ^{17}O MAS NMR spectra were recorded on this spectrometer (by Dr. David Apperley).

2.1.2.4 Chemagnetics CMX 200

This spectrometer was used for initial ^{31}P MAS NMR studies, and by Birkett for the ^{13}C MAS NMR study of the HEB2 system. This system operates at 4.7 T, has a triple channel set-up and is also wide-bore. Experimental details for the NMR relating to the HEB2 system are given elsewhere.[6] The system is controlled from a Sun work station using the Spinsight software.[10]

2.1.3 Probes

The majority of the NMR spectra presented in this work were recorded using a standard 4 mm Bruker probe, which can be used to obtain both MAS (maximum spin rate 15 kHz) and static spectra, and has a tuning range of 44-122 MHz for the Bruker DSX 300 spectrometer, and 40-163 MHz for the Bruker DSX 400 spectrometer. The probe is tuned to the desired frequency by altering the capacitance of a capacitor within the probe. Like other MAS probes, the Bruker probe is fitted with a spinning module that can be set to the magic-angle. The spinning module will house 4 mm outer diameter zirconia rotors (rotors formed from other materials are available, but were not used here), which comprise the rotor itself and a fluted Kel-F $((CF_2CFCl)_n)$ end-cap.

The magic-angle is conveniently set using the ^{79}Br signal of KBr. KBr has an imperfect cubic lattice structure so that quadrupolar interaction does not disappear but lead to rotational echoes in the spectrum under MAS conditions. The magic angle, of 54' 44° to the magnetic field, is set correctly when rotational echoes are maximised in the FID.

The probe was tuned and power levels for the 90° pulse set following standard procedures.

2.1.4 Shimming

It is usual that B_0, the magnetic field of the spectrometers, contains inhomogeneities, so a range of precessions are created, as different parts of the sample see different magnetic fields, which can lead to broad, unsymmetrical peaks being obtained. To compensate for this, the current along the shim coils (situated in the bore of the magnet) are altered, while observing the effect this has on a standard material, such as 85% phosphoric acid for ^{31}P. Two types of shims are present in the magnet, superconducting and room temperature, with the latter being adjusted as described, and the former being adjusted when the magnet is initially run up to field.

2.1.5 Referencing

To allow the spectra of different samples and spectra recorded on different systems to be compared, reference materials are used. The references used in this study are shown in table 2.2, along with the NMR frequencies of the nuclei for a 2.3 T field.

Nucleus	Reference	NMR frequency at 2.3 T
^{31}P	85% H_3PO_4 at 0 ppm	40.48
^{17}O	Tap water at 0 ppm	13.56

Table 2.2. The reference samples used in this study, along with NMR frequencies of the nuclei.

After referencing, the sample being studied is placed into the probe, and the 'tune' and 'match' adjusted in the standard way, and parameters such at recycle delay and resonance frequency optimised.

2.1.6 Variable-Temperature Set-Up

Variable-temperature (VT) MAS NMR experiments were carried out on the Bruker DSX 400 spectrometer. The operation of VT MAS NMR is regulated by the three gases entering the probe, two (the bearing and drive gases) controlling spinning, and the third adjusting the

temperature of the rotor, and hence the sample. Nitrogen is used to control the temperature by heating/cooling it and running it over the rotor. The bearing and drive gases are pressurised air inside the 0°C-100°C temperature range, while outside this range they are switched to nitrogen. The temperature is measured before the nitrogen reaches the rotor, so a calibration must be undertaken to obtain the actual sample temperature for a given temperature reading. This is done using the ^{207}Pb chemical shift in lead nitrate (Pb(NO$_3$)$_2$), for which the variation of chemical shift with temperature is well documented in the literature,[11,12] with the temperature curve used in this study given in Appendix 1. To reach a temperature equilibrium over the sample, 20 minutes is allowed after any temperature adjustment before a spectrum is recorded at that temperature.

2.1.7 Pulse Sequences

1D MAS NMR spectra were recorded using a simple single-pulse experiment, which consist of a single pulse followed by an acquisition and a recycle delay. The 2D MAS NMR pulse sequences are described in chapter 3.

2.1.8 Quadrupolar Nuclei

Quadrupolar nuclei is the name given to NMR active nuclei with I > ½ (e.g. ^{17}O). The NMR spectra of these nuclei are complicated as, unlike spin ½ nuclei, more than one energy level transition is possible giving rise to spinning sidebands, quadrupolar splitting and broadened resonances, which themselves often are unsymmetrical in shape due to quadrupolar coupling effects. The quadrupolar coupling is present due to an electric quadrupolar moment which interacts with the local electric field gradient. These interactions also give rise to quadrupolar relaxation effects, so that quadrupolar relax to an equilibrium position relatively quickly after an rf pulse is applied. These effects are discussed further in chapter 6.

2.2 Powder X-ray Diffraction (XRD)

2.2.1 General Overview

X-ray diffraction (XRD) is a technique used in both structure solution and the investigation of properties relating to the structure of a material, such as the effect of temperature on a structure and sample purity. It relies on the generation and collection of X-rays. X-rays are generated by bombarding a metal with electrons of sufficient energy to cause K-shell electrons to be emitted. This creates a vacancy, which is filled by L-shell and M-shell electrons. This process emits energy, with the different electrons giving rise to K_α and K_β lines respectively. The X-rays are then aimed at the sample. As the wavelength of X-rays is of the same order of magnitude as interatomic spacings within crystals, diffraction phenomena occur. The diffraction can be considered in terms of reflections from the planes of atoms. Diffraction maxima will only occur when there is a condition for constructive interference, known as the Bragg Condition:

$$\lambda = 2d(\sin\theta) \qquad\qquad \text{(Equation 2.3)}$$

When this occurs, 'reflections' are seen from different planes (fig. 2.4) and the diffracted X-rays are collected by a detector.
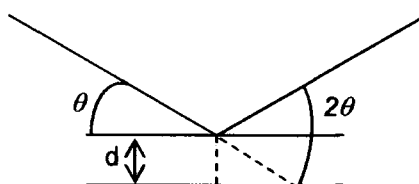
Figure 2.4. Reflection of X-rays by plane.

This then gives a unique diffraction map for single crystals and a powder pattern for powdered samples. In favourable cases such data can then be used for structure solution, for comparison to database data to check for impurities, to study structural parameters, etc.

2.2.2 Diffractometers

Two X-ray diffractometers (a Siemens D5000 and a Bruker D8) and one synchrotron diffractometer (beamline x7a of the National Synchrotron Light Source at Brookhaven National Laboratory, USA) were used in this study; each is discussed below.

2.2.2.1 Siemens D5000

The Siemens D5000 has a CuK_α radiation source, and a graphite diffracted beam monochromator, giving an average $K_{\alpha/\beta}$ wavelength of 1.5418Å, and is equipped with a sample changer, allowing a number of samples to be run in succession. The diffractometer was mainly used for the collection of initial data, to check sample purity and sample crystallinity. All data collected on this diffractometer were recorded in reflection mode (see section 2.2.2.2).

2.2.2.2 Bruker D8

The Bruker D8 diffractometer has a variety of set-ups, allowing a greater range of information to be collected than in the case of the Siemens D5000. The diffractometer is equipped with an incident beam curved Ge(111) monochromator, giving a wavelength of 1.540598 Å, and a MBraun linear position-sensitive detector. A number of set-ups were used on this diffractometer, including reflection mode, flat plate transmission mode and capillary transmission mode. Variable temperature (VT) XRD data were also collected in reflection mode. Each of these is discussed below:

i)   Reflection mode: In this mode the sample is mounted upon a Si plate or as a bulk powder, so that X-rays are diffracted off the surface and collected by a detector. One problem that can occur with this mode is an enhancement of preferred orientation. For example, when samples containing flat crystallites, are dropped onto a flat plate many fall in such a way that one axis is normal to the plate. This can perhaps be likened to dropping pieces of paper onto a desk, and will cause an artificial enhancement of certain reflections in the powder XRD.

ii)   Transmission mode: A mode often used for samples that exhibit preferred orientation. In this set-up samples are mounted on Mylar foil, so that transmitted X-rays are diffracted from a thin film of the sample and collected by the detector. This mode also suffers from preferred orientation but gives preference to the collection of reflections 'disfavoured' in reflection mode.

iii)   Capillary mode: This is the best method for the removal of preferred orientation effects, and for the investigation of air-sensitive materials, as this mode involves the sample being housed in a sealed capillary tube. This mode reduces/removes preferred orientation as packing of the samples in a capillary tube gives a more random orientation of crystallites.

iv)   Variable temperature mode: Data at temperatures between of 78 K to 1500 K can be collected on the Bruker D8 using an Anton Paar TTK450 cryofurnace (78 K to 750 K) and an Anton Paar HTK1200 environmental furnace (room temperature to 1500 K). In both of these data are obtained in reflection mode, with samples sprinkled on an Al plate (cryofurnace) or on an amorphous SiO_2 disc (furnace). The cryofurnace works by using a controlled flow of liquid N_2 to cool down the Al plate, and hence the sample, while the furnace works by heating the atmosphere around the sample.

2.2.2.3 Synchrotron

A synchrotron is an intense source of radiation, generated from accelerated charges produced from a synchrotron storage ring, which consists of an electron beam. Charges produce electromagnetic radiation when accelerated, and as electrons are constantly accelerating when travelling in a circle they generate radiation.[13] These sources are only usually available at national facilities due to their size and running costs. In this study data were collected on beamline x7a of the National Synchrotron Light Source at Brookhaven National Laboratory (USA) at a wavelength of 0.7452 Å.

2.2.3 XRD Experiments

On both the Siemens D5000 and Bruker D8 diffractometers, PC-based Bruker Diffrac Plus software was used to control XRD experiments, with the user inputting a 2θ range over which to collect data, a step size (in degrees) and any temperature settings required. Samples are mounted on an appropriate plate, according to the diffractometer and set-up being used, and in the case of Si discs and glass slides Vaseline is used to ensure the sample remains attached to the slide as it is rotated in the diffractometer (fig. 2.5). The height the sample is at in the diffractometer affects the 2θ positions recorded, so it is important that samples sit at the correct height. This can be calibrated using a standard such as Y_2O_3 or Si, for which the positions of reflections are known to a high degree of accuracy.

Variable-temperature experiments were carried out by recording powder diffraction patterns on both heating and cooling of the sample (or cooling and heating for the cryofurnace), with 5 minutes being given at each temperature to equilibrate the sample temperature, and scans were recorded at each temperature over 20 to 30 minutes, to ensure reasonable quality of the data collected. Again, as in VT NMR experiments, calibration of the actual sample temperature as compared to the set temperature was required. Again, a standard sample is used for which the positions of reflections are accurately known over a wide temperature range. In this work the temperatures were calibrated relative to the expansion data of Al_2O_3 given by Taylor.[14] A calibration curve is shown in Appendix 2.

2.2.4 Rietveld Method[15-17]

An X-ray powder pattern is a set of intensities at different 2θ values over the recorded angular range, from which information, such as unit cell parameter and atomic positions, can be extracted. The most widely used method for this is the Rietveld method[15-17] in which least squares refinements are carried out simultaneously on a number of parameters (table 2.3) in order to achieve the best fit between experimental and calculated powder patterns. The parameters are refined to minimise the weighted square difference between the model and the experimental data.

Parameters refined for each individual phase in XRD powder pattern	Global parameters
Atomic position coordinates Atomic thermal factors (either isotropic or anisotropic) Peak shape Lattice parameters Scale factor Preferred orientation	Background terms Instrument profile Sample displacements 2θ zero-point Absorption correction

Table 2.3. List of parameters commonly refined in the Rietveld method.

For this method to be of use it is important that any fit obtained can be quantified, and in the Rietveld method this is commonly given by two residual factors (*R*-factors), which the least squares fitting minimises. These *R*-factors are R_{wp} (weighted *R*-factors) and R_B (the Bragg factor), R_{wp} being the most meaningful as the numerator is the actual residual being minimised (equation 2.4). R_B (equation 2.5) is of use as it is insensitive to misfits in the pattern that do not involve Bragg intensities of the phase being modelled (where the Bragg intensity is the intensity of a reflection), and it is also less influenced by factors such as high experimental background which can often lead to very low values of R_{wp}, despite the quality of the structural fit being poor.

$$R_{wp} = \left\{ \frac{\sum \omega_i \left(y_i(obs) - y_i(calc)\right)^2}{\sum \omega_i \left(y_i(obs)\right)^2} \right\}^{1/2}$$ (Equation 2.4)

$$R_B = \frac{\sum \left| I_K('obs') - I_K(calc) \right|}{\sum I_K('obs')}$$ (Equation 2.5)

In these equations ω_i is a weighting factor, often assumed to be the reciprocal of y_i, the observed intensity at the *i*th step, though for more complex diffractometers such as synchrotron and neutron instruments, related directly to the uncertainty of y_i, at each point in the pattern. I_K is the intensity assigned to the *K*th Bragg reflection at the end of the refinement cycles.

It should be noted that this method is a structure refinement method, and a good starting model is required. It is not a structure solution method, although it is usually applied following the final steps of structure solution (see chapter 6).

2.3 Electron Diffraction

The electron diffraction patterns presented in this thesis were recorded by Prof. Ray L. Withers & co-workers (Australian National University, Canberra, Australia), using JOEL 100CX and Philips EM430 transmission electron microscopes (TEMs), with samples dispersed onto holey-carbon coated molybdenum grids. Variable-temperature electron diffraction was carried out on the JEOL 100CX TEM, using an EM-SHTH2 double tilt heating holder.

2.4 References

(1)   Korthuis, V.; Khosrovani, N.; Sleight, A. W.; Roberts, N.; Dupree, R.; Warren, W. W. *Chemistry of Materials* 1995, *7*, 412-417.

(2)   Khosrovani, K.; Sleight, A. W.; Vogt, T. *Journal of Solid State Chemistry* 1997, *132*, 355-360.

(3)   Tait, M. M.; *4th year Project Report*, Durham University, 2002.

(4)   Gover, R. K. B.; Withers, N. D.; Allen, S.; Withers, R. L.; Evans, J. S. O. *J. Solid State Chem.* 2002, *166*, 42-48.

(5)   Brindley, J., University of Durham, 2001.

(6)   Birkett, H. E.; *PhD Thesis,* Chemistry Department, University of Durham, UK, 2000.

(7)   Cherryman, J.; *PhD Thesis*, Department of Chemistry, University of Durham, UK, 1998.

(8)   Andrew, E. R.; Bradbury, A.; Eades, R. G. *Nature* 1958, *182*, 1659.

(9)   Harris, R. K. *Nuclear Magnetic Resonance Spectroscopy*, 2nd ed.; Longman: Harlow, 1986.

(10)   Chemagnetics; Version 3.5.2 ed.; Otsuka Electonics (USA) Inc.

(11)   Bielecki, A.; Burum, D. P. *J. Magn. Res.* 1995, *A116*, 215-220.

(12)   van Gorkom, L. C. M.; Hook, J. M.; Logan, M. B.; Hanna, J. V.; Wasylishen, R. E. *Magn. Reson. Chem.* 1995, *33*, 791-795.

(13)   Atkins, P. W. *Physical Chemistry*, 5th ed.; Oxford University Press: Oxford, 1994.

(14)   Taylor, D. *Br. Ceram. Trans. J.* 1984, *83*, 92-98.

(15)   Rietveld, H. M. *Acta Cryst.* 1967, *22*, 151-152.

(16)   Rietveld, H. M. *J. Appl. Cryst.* 1969, *2*, 65-71.

(17)   Young, E. R. A. *The Rietveld Method*; Oxford Science Publications: Oxford, 1996.

Chapter 3

2D Pulse Sequences and Spectra Interpretation

3.0 Introduction

In this chapter a description of each of the pulse sequences used in chapter 5 to obtain 2D NMR spectra will be given, as well as an explanation of how to interpret these spectra.

As has already been stated in chapter 2, high-quality solid-state NMR spectra can often be difficult to obtain, due to factors such as the relative lack of motion in the solid-state (leading to long relaxation times), quadrupolar interactions and structural imperfections. To overcome these problems a number of techniques, ranging from physical solutions (e.g. magic angle spinning [MAS]), to complex pulse sequences (e.g. such as multiple-quantum MAS to overcome quadrupolar effects), are used.

As part of this study four different 2D solid-state NMR experiments were used to gain increased resolution and to probe through-space [dipolar] interactions and through-bond [J] interactions. For many 2D NMR experiments a mixing time is incorporated into the pulse sequence, and it is in this time that through-space and/or through bond interactions are reintroduced. So, at shorter mixing times shorter range interactions are seen, while at longer mixing times longer range interactions are seen. A mixing time is employed for the four experiments seen here, those being the RFDR, POST-C7, POST-C9 and refocused-INAQDEQUATE pulse sequences. The pulse sequences will be discussed individually below, with an explanation of how to interpret the spectra obtained given at the end for all four pulse sequences.

3.1 2D Pulse Sequences

3.1.1 Phase Cycling

Phase cycling is an important part of many 2D NMR experiments, and is the process of repeating a pulse sequence many times with a systematic variation of the relative phases within the sequence. Phase cycling is used to select a particular sequence of events, caused by numerous radio-frequency pulses in the sequence. When an experiment uses multiple pulses there will be a number of ways in which an observable signal can be achieved, and it is therefore important to be able to discriminate between these, which is where the use of phase cycling comes in. For example, both the RFDR and POST-C7 experiments (sections 3.1.2 and 3.1.3 respectively) essentially contain three-pulse sequences, but the use of different phase cycles allows different information to be obtained/omitted from the spectra recorded.

As stated above, calculation of the phase cycle for a given pulse is important, and an example is given, in this case for a 2D exchange experiment (fig. 3.1).
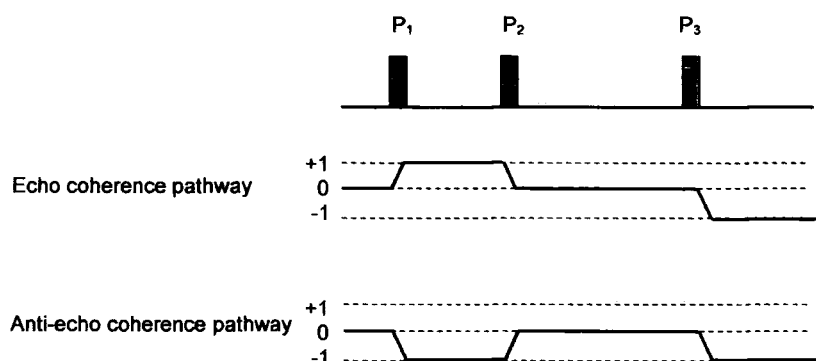
Figure 3.1. 2D exchange experiment: pulse sequence and its respective coherence pathways[1] (the two possible pathways are shown separately in this figure for clarity).

For this study the States[1] mode was used, which allows a pure absorption-mode lineshape to be obtained in both frequency dimensions. The advantages of using this method are that improved signal-to-noise is achieved, narrower linewidths are obtained, and in crowded regions

---

[1] On application of an r.f. field at the resonance frequency (known as the Larmor frequency) the spins of an NMR sample resonate and a state of phase coherence is obtained. If this phase coherence is generated by a single-quantum transition it is known as a single-quantum coherence, which is identical to transverse magnetisation (in the xy plane). The path by which this coherence is transferred between quantum levels from the start to the finish in an NMR experiment is called the coherence pathway.

31

of 2D spectra prominent overlap features seen in magnitude spectra disappear when the pure-phase method of States is used.

A full review of this and related methods has been given by Keeler & Neuhaus.[2]

So, using the States mode, the echo and anti-echo pathways are involved, where;

and,

$$Echo = S_x + iS_y \qquad \text{(Equation 3.1)}$$

$$Anti\text{-}echo = S_x - iS_y \qquad \text{(Equation 3.2)}$$

As can be seen in fig. 3.1 this is a three-pulse experiment. It is known that the phase of the receiver, ϕ_R, is given by

$$-\phi_R = \sum_i \Delta P_i . \phi_i = \Delta P_1 \phi_1 + \Delta P_2 \phi_2 + \Delta P_3 \phi_3 \qquad \text{(Equation 3.3)}$$

Therefore the echo and anti-echo pathways are given by

Echo:

$$\Delta P_1 = +1; \quad \Delta P_2 = -1; \quad \Delta P_3 = -1$$

$$-\phi_R = \phi_1 - \phi_2 - \phi_3 \qquad \text{(Equation 3.4)}$$

Anti-echo:

$$\Delta P_1 = -1; \Delta P_2 = +1; \Delta P_3 = -1$$

$$-\phi_R = -\phi_1 + \phi_2 - \phi_3 \qquad \text{(Equation 3.5)}$$

The phase increment, $\Delta\phi$, is given by:

$$\Delta\phi < \frac{2\pi}{-\Delta P_{min} + \Delta P_{max}} \qquad \text{(Equation 3.6)}$$

Therefore;

$$\phi_1 : \Delta\phi_1 < \frac{2\pi}{2} \qquad \text{(Equation 3.7)}$$

$$\phi_2 : \Delta\phi_2 < \frac{2\pi}{2} \qquad \text{(Equation 3.8)}$$

$$\phi_3 : \Delta\phi_3 < \frac{2\pi}{2} \qquad \text{(Equation 3.9)}$$

For m pulses, $(m-1)$ phase cycles are needed. In this case $m = 3$, so $(m-1) = 2$.

For P_1, $\Delta\phi_1 < 180°$, so $\Delta\phi_1 = 90°$ was used, and was P_1 cycled.

For P_2, $\Delta\phi_2 < 180°$, so $\Delta\phi_2 = 90°$ can be used, but only 2 pulses need to be cycled, so $\Delta\phi_2 = 0$ was used, i.e. this pulse was not cycled.

For P$_3$, $\Delta\phi_3$ < 180°, so $\Delta\phi_3$ = 90° was used and P$_3$ was cycled.

So, for the echo, equation 3.4 can be written $\phi_R = -\phi_1 + \phi_2 + \phi_3$, but ϕ_2 = 0, therefore,

$$\phi_R = \phi_3 - \phi_1 \qquad \text{(Equation 3.10)}$$

While for the anti-echo equation 3.5 can be written;

$$\phi_R = \phi_1 + \phi_3 \qquad \text{(Equation 3.11)}$$

As $\Delta\phi_1$ = 90° and $\Delta\phi_3$ = 90° tables 3.1 and 3.2 can be constructed;

ϕ_1				ϕ_3	ϕ_R $(=\phi_3-\phi_1)$			
0°	90°	180°	270°	0°	0°	270°	180°	90°
				90°	90°	0°	270°	180°
				180°	180°	90°	0°	270°
				270°	270°	180°	90°	0°

Table 3.1. 2D exchange echo phase cycle table.

From these two tables it is possible to construct a phase cycle that will select the required pathway, as shown in fig. 3.1. For this to be the case the phase cycle must be such that both the required echo and anti-echo pathways are selected.

ϕ_1				ϕ_3	ϕ_R $(=\phi_1+\phi_3)$			
0°	90°	180°	270°	0°	0°	90°	180°	270°
				90°	90°	180°	270°	0°
				180°	180°	270°	0°	90°
				270°	270°	0°	90°	180°

Table 3.2. 2D exchange anti-echo phase cycle table.

From tables 3.1 and 3.2 it can be seen that the echo and anti-echo phase cycles show common (S$_x$) parts and opposite (S$_y$) parts. The hyper-complex method[1] used here requires the recording of these common and opposite parts and the reconstruction of the echo and anti-echo

signals during the processing of the spectra. Thus for S_x a phase cycling can be constructed as shown in table 3.3.

ϕ_1^{SX}		ϕ_3^{SX}	ϕ_R^{SX}	
0°	180°	0°	0°	180°
		90°	90°	270°
		180°	180°	0°
		270°	270°	90°

Table 3.3. S_x phase cycling.

So the phase cycling for S_x is,

$$\phi_R^{SX}: (0°\ 180°)\ (90°\ 270°)\ (180°\ 0°)\ (270°\ 90°)$$

For the opposite parts, S_y, a phase cycle table can be constructed, as shown in table 3.4.

ϕ_1^{SY}		ϕ_3^{SY}	ϕ_R^{SY}	
90°	270°	0°	270°	90°
		90°	0°	180°
		180°	90°	270°
		270°	180°	0°

Table 3.4. S_y phase cycling.

For S_y the phase cycling is,

$$\phi_R^{SY}: (90°\ 270°)\ (180°\ 0°)\ (270°\ 90°)\ (0°\ 180°)$$

However, for $-S_y$, the phase list has a -270° shift, so the phase cycle becomes;

$$\phi_R^{-SY}: (0°\ 180°)\ (90°\ 270°)\ (180°\ 0°)\ (270°\ 90°)$$

Note this phase list is identical to that of S_x. It is possible to choose to acquire either S_y or $-S_y$, (eqn. 3.1 and eqn. 3.2) with the two resulting 2D spectra being mirror images w.r.t. the F1 dimension. Experimentally it is more convenient to use the same phase list for both common

and opposite parts, so in this case -S$_y$ is chosen. Therefore eight steps are present in the phase cycle, so the number of acquisitions must be 8n, where n = an integer.

This process can be followed for all 2D pulse sequences, although the process may be more complicated for complex pulse sequences.

3.1.2 2D Radio Frequency-driven Dipolar Recoupling (RFDR)[3]

The Radio Frequency (rf)-driven Dipolar Recoupling (RFDR) experiment is a useful tool in solid-state NMR. The experiment utilises through-space dipolar interactions to look at both short range and long range interaction, depending on the value of the mixing time. This experiment shows no interactions between atoms from different crystallites, allowing a test of purity.

The experiment involves the exchange of magnetisation due to dipolar coupling. The pulse sequence used is shown in fig. 3.2, along with its coherence pathway. In this experiment the States[1] hyper-complex acquisition mode was used to obtain pure absorption phase 2-D spectra.
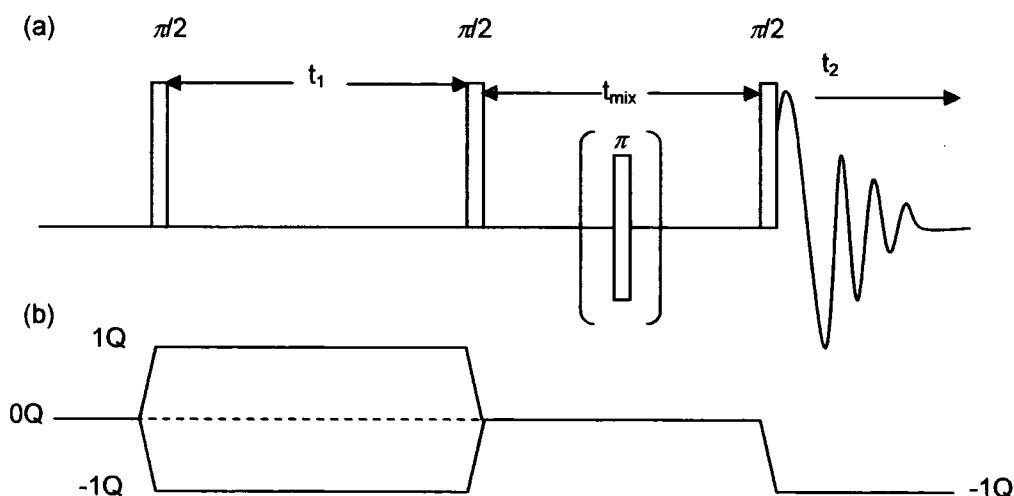
Figure 3.2 (a) The RFDR pulse sequence and (b) the related coherence pathway.

The phase cycle used for this pulse sequence is:

$$\phi_R^{-sy}: (0° \ 180°) \ (90° \ 270°) \ (180° \ 0°) \ (270° \ 90°)$$

This was worked out as shown in section 3.1.1.

The full RFDR pulse sequence, along with the other pulse sequences presented in this chapter and as used to collect the spectra in Chapter 5, on a Bruker DSX 300, is shown in Appendix 3.

In the pulse sequence (fig. 3.2), the first pulse is used to create 1Q coherence, which evolves during t_1. The second pulse then stores magnetisation along the z-axis during the mixing time, t_{mix}. During t_{mix} magnetisation transfer is driven by dipolar interactions that are removed by MAS conditions. To overcome this, rotor synchronised π-pulses are applied, with a super-cycle that spans [n x 8 x (1/spinning speed)], to reintroduce the dipolar interactions and allow the magnetisation transfer to occur. The last pulse then creates observable 1Q coherence.

3.1.3 2D POST-C7[4,5]

The C7 pulse sequence was first presented by Lee et al.[4] The experiment involved seven phase-shifted rf pulse cycles, which spanned two rotor periods, and double-quantum (DQ) coherences to efficiently reintroduce dipolar coupling under MAS conditions. Later an improved version of this pulse sequence, the Permutationally Offset Stabilized C7 (POST-C7), was introduced by Hohwy et al.[5] This improved version gives a better tolerance towards isotropic and anisotropic chemical shift offset and rf inhomogeneity. It was this latter pulse-sequence that was used in this study, although the original sequence will be discussed briefly first. The pulse sequence, common to both, is shown in fig. 3.3.

The aim of the C7 pulse sequence is to reintroduce homonuclear dipolar coupling under MAS conditions, with the use of DQ filtration. This latter condition means that nuclear magnetisation is passed through DQ coherence, which is a quantum state of correlated transverse spin polarisations. DQ filtration readily distinguishes between pairs of spins and isolated spins, as single spins cannot support DQ coherence (for $I = \frac{1}{2}$). In the C7 experiment a C7 sequence of duration τ_{exc} converts z-magnetisation into DQ coherence, then, after a time t_1 in which dipolar interactions evolve, a second C7 sequence, also of duration τ_{exc} reconverts the DQ coherence into longitudinal magnetisation. A final 90° pulse transforms this longitudinal magnetisation into transverse magnetisation, which induces an NMR signal. The POST-C7 experiment is carried

out in the same manner, but with a different C7 sequence which gives the improvements

mentioned above. In the original C7 experiment the C7 sequence is a cycle of seven rf pulses,

each consisting of two 2π pulses, with phase differing by π. The seven cycles are timed to

occupy two rotor periods. The reconversion sequence has an additional phase shift of ($\pi/2$, π,

$3\pi/2$, 0) in consecutive experiments, which Lee et al. state as standard practice for selecting

NMR signals passing through double-quantum coherence.[4]

The POST-C7 pulse sequence works in the same manner, but with a different C7 DQ excitation

and reconversion sequence, so that instead of the cycles consisting of two 2π pulses with

differing phases, they consist of three elements of $\pi/2$, 2π, and $3\pi/2$, with the middle pulse

differing in phase relative to the other two by π.
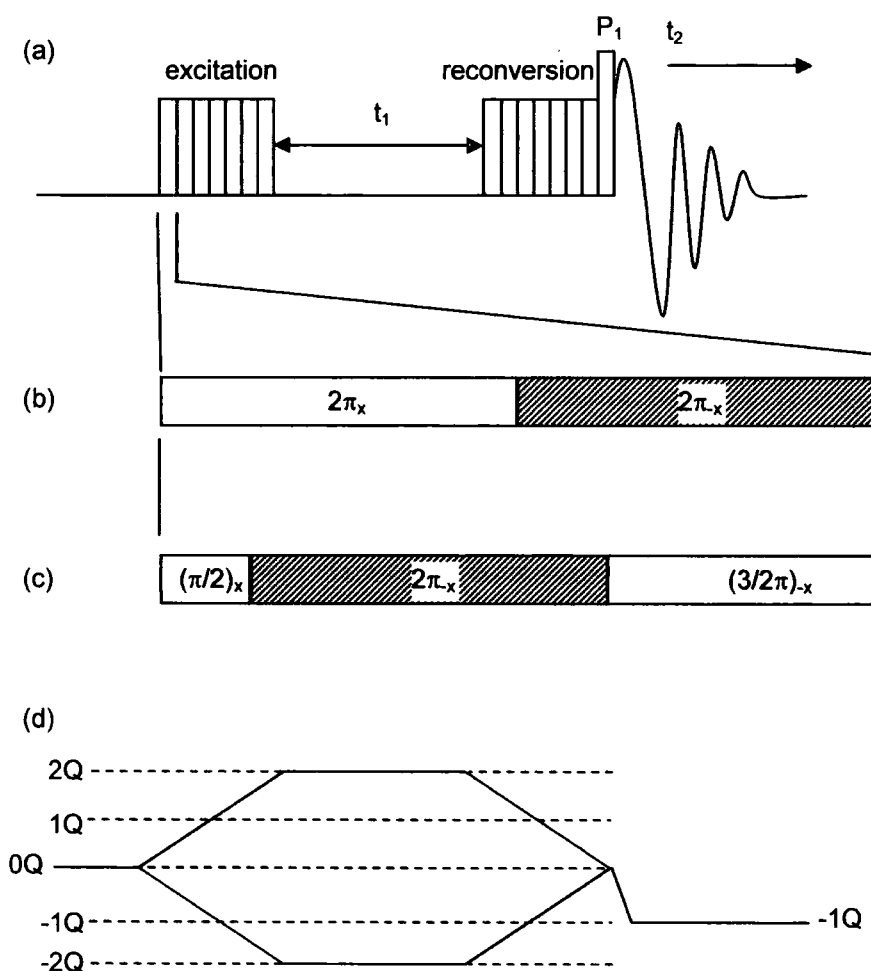
Figure 3.3. (a) The pulse sequence for the C7 and POST-C7 experiments, with (b) and (c) showing the pulses used in each of the C7 reconversion and excitation cycles for the C7 and POST-C7 experiments respectively. (d) The coherence pathway for the double quantum C7 experiment.

Again, as in the case of the RFDR experiment (section 3.1.2), the States method was used, and using the theory in section 3.1.1 it can be shown that the necessary phase cycling is

$$\phi_R{}^{Sx} = (180° \ 0° \ 180° \ 0°) \ (270° \ 90° \ 270° \ 90°) \ (0° \ 180° \ 0° \ 180°) \ (90° \ 270° \ 90° \ 270°)$$

$$\phi_R{}^{-Sy} = (0° \ 180° \ 0° \ 180°) \ (90° \ 270° \ 90° \ 270°) \ (180° \ 0° \ 180° \ 0°) \ (270° \ 90° \ 270° \ 90°)$$

Again, $-S_y$ is used, and in this case a minimum of 16 steps is required, so $16n$ acquisitions are required for this pulse sequence.

One feature of spectra that result from pulse sequences containing DQ filtration is that they do not contain the 1D spectrum along the diagonal, giving enhanced resolution. This will be discussed below in section 3.2.

3.1.4 2D POST-C9[6,7]

The POST-C9 experiment[6,7] is one which utilises through-bond interactions, i.e. J-couplings. J-couplings are weak interactions when compared to dipolar-couplings, e.g. typically in $P_2O_7{}^{4-}$ units the J-coupling for $^2J|(P–O–P)| \sim 20$ Hz, while for intra-unit dipolar coupling $d|(P–P)| \sim 700$ Hz. The advantage of experiments showing only through-bond interactions is that they usually give greater resolution as they contain less information than those utilising through-space interactions. These types of experiments can aid in spectral assignment, as will be shown below in sections 3.2.3 and 3.2.4.

The POST-C9 pulse sequence and coherence pathway is shown below in fig. 3.4. A first pulse is applied to the sample under MAS conditions to create 1Q coherence, which evolves during t_1. A second pulse is then applied, storing the magnetisation along the z-axis during a mixing time. It is in this mixing time that the POST-C9 sequence is applied. This POST-C9 sequence suppresses resonance offsets, and promotes magnetisation transfer driven by isotropic J-coupling. A third pulse is finally applied which creates the observable 1Q coherence. The phase cycling used for this experiment is;

$$\phi_R{}^{Sx} = (0° \ 180° \ 90° \ 270°) \ (180° \ 0° \ 270° \ 90°)$$

$$\phi_R^{-Sy} = (0°\ 180°\ 90°\ 270°)\ (180°\ 0°\ 270°\ 90°)$$

Here a minimum of 8 steps is required, so there are $8n$ acquisitions.
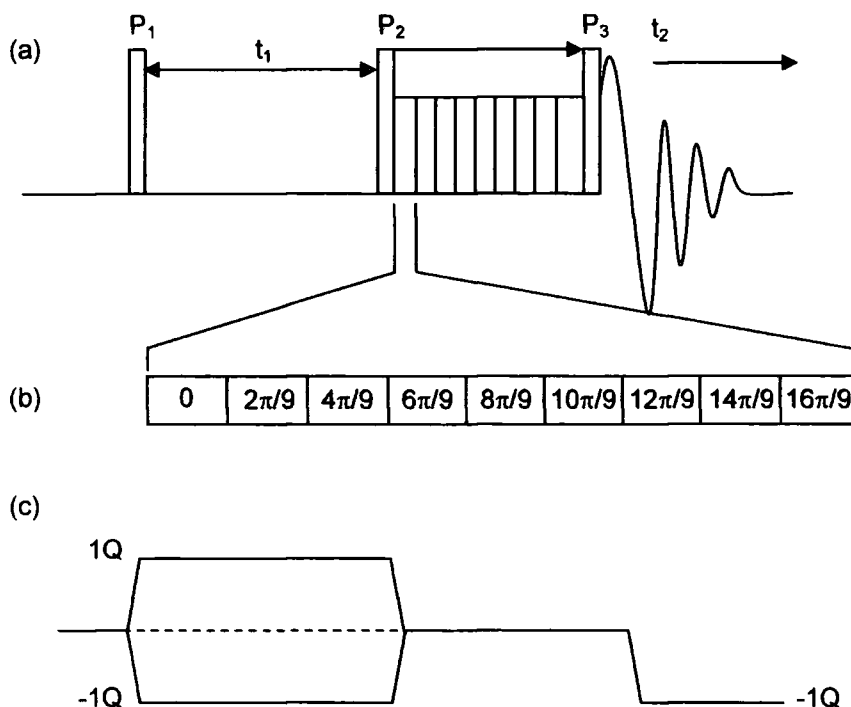
Figure 3.4. (a) The POST-C9 pulse sequence, with (b) the rf phase in each of the C9 cycles shown. (c) The coherence pathway used for the POST-C9 pulse sequence.

3.1.5 2D refocused-INADEQUATE[8]

The refocused-INADEQUATE experiment[8] is a pulse sequence that probes through-bond connectivities, and combines this with a DQ filter, giving a resolution advantage over the POST-C9 experiment, as the filter will remove the 1D MAS spectrum from the diagonal. The pulse sequence used here, along with the coherence pathway, is shown in fig. 3.5. The first pulse allows J-coupling to evolve during the 2τ delay. The dipolar coupling is removed by MAS and the 180° pulse refocuses the chemical shift. The next 90° pulse creates the DQ coherence, which evolves during t_1, and is converted back into the anti-phase transverse coherence by the last 90° pulse. The second $\tau-\pi-\tau$ delay converts the anti-phase component back into an in-phase signal.

If the delay, τ, is synchronised with the spinning frequency, then the efficiency of this experiment is shown by Lesage et al.[8] to depend on the efficiency of the DQ coherence and the decay of magnetisation during the τ delays.
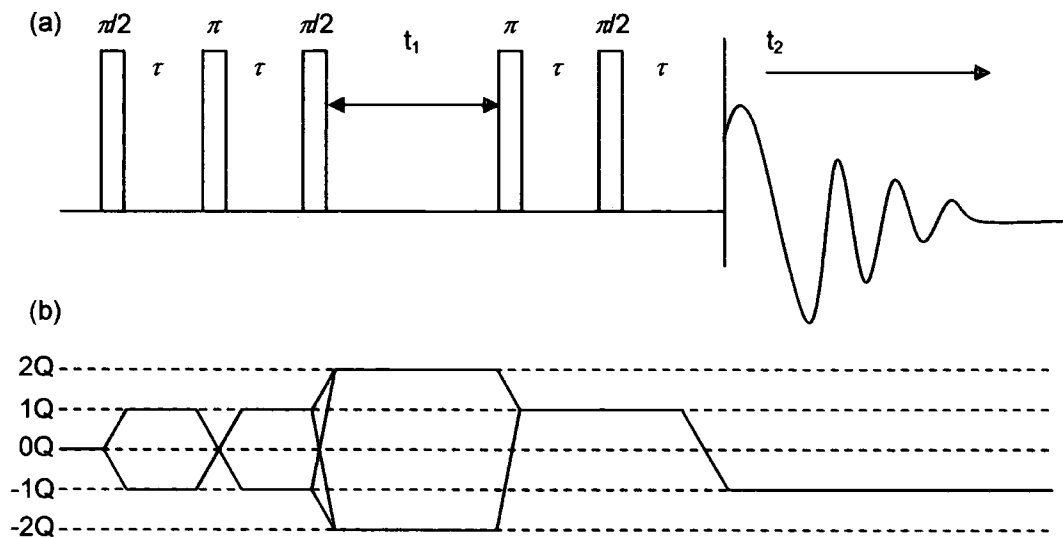
Figure 3.5. (a) The refocused-INADEQUATE pulse sequence, and (b) the related coherence pathway.

The phase cycling used for this experiment was;

ph2; (90° 180° 270° 0°) (180° 270° 0° 90°) (270° 0° 90° 180°) (0° 90° 180° 270°)

$\phi_R{}^{Sx}$; (90° 180° 90° 180°) (180° 90° 180° 90°)

$\phi_R{}^{-Sy}$; (90° 180° 90° 180°) (180° 90° 180° 90°)

where ph2 is the first π pulse.

3.2 Experimental Set-up

In all of these 2D MAS NMR experiments $\pi/2$ and/or π-pulses are applied, and it is important that these are firstly measured and optimised.

3.2.1 2D RFDR

Since this is a magnetisation exchange experiment, the most important parameter in the RFDR pulse sequence is the mixing time, t_{mix}. During this mixing period rotor synchronised π-pulses are applied with a super-cycle that spans n x 8 x t_{rot}, where t_{rot} is the time of rotation (or the inverse of the MAS frequency, u_{rot}). So, by varying the spinning rate, the mixing time can be controlled, allowing different strengths of dipolar couplings to be probed. The highest efficiency is achieved for this experiment when $t_{mix} \approx (1/D)$, where D is the dipolar coupling constant.

3.2.2 2D POST-C7

The POST-C7 sequence reintroduces dipolar couplings through double-quantum excitation and reconversion. The pulse sequence requires the rotary resonance condition of $\omega_1 = 7$ x ω_{rot}. To get this required condition the rf field at a fixed spinning rate is optimised by varying the power level. Varying the excitation time allows different strengths of dipolar couplings to be probed.

3.2.3 2D POST-C9

Like the RFDR experiment, the POST-C9 experiment involves magnetisation-exchange, but differs from the RFDR experiment in the pulse sequence applied during the mixing time. This change of pulse sequence gives a spectrum showing J-couplings rather than the dipolar couplings seen in an RFDR spectrum. In this experiment the rotary resonance condition is $\omega_1 = 6$ x ω_{rot}, and again this requires the optimisation of the power level at a set spinning rate.

3.2.4 2D refocused-INADEQUATE

The key parameter requiring optimisation for this pulse sequence to be successfully implemented is τ, the delay used in the excitation and reconversion periods. Neglecting T_2 relaxation effects (where T_2 is the relaxation time of magnetisation in the xy plane), the maximum efficiency is obtained for $\tau = 1/(4J)$ (where J is the J-coupling constant). Altering τ allow greater and weaker J-couplings to be probed.

3.3 2D Spectral Interpretation

Although the theory and pulse sequences used for 2D NMR are usually complicated, the interpretation of 2D NMR spectra can often be relatively simple. This is shown here for a number of pulse sequences using the examples of mixed phase α/β-$Zn_2P_2O_7$ and α/β-$Mg_2P_2O_7$. A 1D MAS NMR spectrum is shown in fig. 3.6 for a mixture of α and β-$Mg_2P_2O_7$. Both of these compound mixtures contain three different phosphorus sites, two arising from one polymorph (the α-polymorph) and one from the second polymorph (the β-polymorph). In both cases the resonance from the polymorph containing a single phosphorus site lies in between the two resonances arising from the polymorph containing two phosphorus sites.

All the 2D experiments used here produce spectra which have 'off-diagonal' peaks, also known as cross-correlation peaks, showing correlations between different sites that are either relatively close in space (through-space dipolar couplings) or connected through bonds (J-couplings), depending on the experiment concerned.
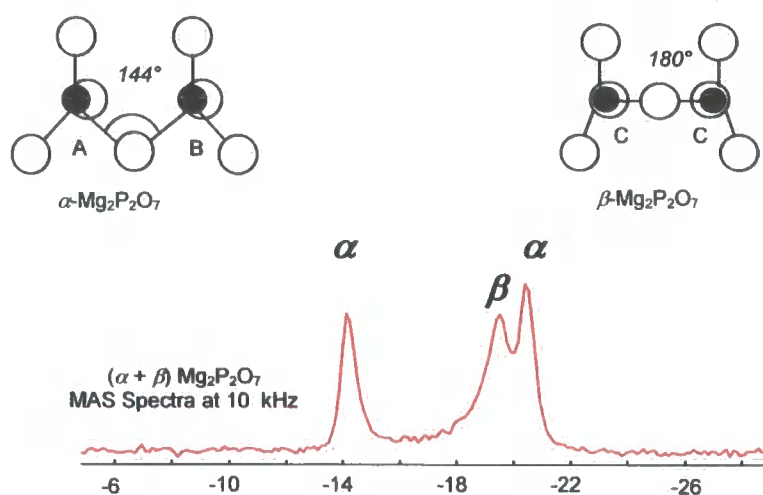
Figure 3.6. 1D MAS spectrum of a mixture of α-$Mg_2P_2O_7$ and β-$Mg_2P_2O_7$.

For experiments utilising dipolar coupling, all the dipolar interactions are first removed and are then selectively reintroduced during a mixing time, T_{mix}. The length of T_{mix} determines which dipolar interactions are seen. With a short T_{mix} shorter range, strong interactions are seen. With a long T_{mix} longer range, weaker, interactions are also seen. Therefore, the value of T_{mix} allows the spectroscopist to control which interactions are studied. It should be noted that for experiments utilising dipolar couplings it is usual for J-couplings to still be present in spectra, but

as these are relatively weak (it is usual for the associated splittings not to be resolvable within the line-widths of 1D spectra) in comparison to dipolar couplings between nearby nuclei, these have no observable influence on the spectra obtained.

The following is a short explanation of what is shown by the spectra of the various experiments used here, and how these experiments are interpreted.

3.3.1 2D RFDR

The 2D RFDR experiment utilises through-space dipolar coupling interactions, with only interactions between atoms in the same crystallographic phase being probed, meaning this is especially useful for studying the purity of samples via NMR. An RFDR spectrum is a correlation of a 1D spectrum with itself, and therefore has the 1D MAS spectrum along the diagonal. In simple cases such as that of a mixture of α/β $Mg_2P_2O_7$ it would be expected that three peaks would be seen along the diagonal, with two correlation peaks seen off the diagonal, arising from dipolar interactions between the two phosphorus sites in the α-polymorph. No correlation peaks would be expected between the resonances from the different polymorphs as these arise from distinct phases. This is illustrated by the spectrum shown in fig. 3.7.
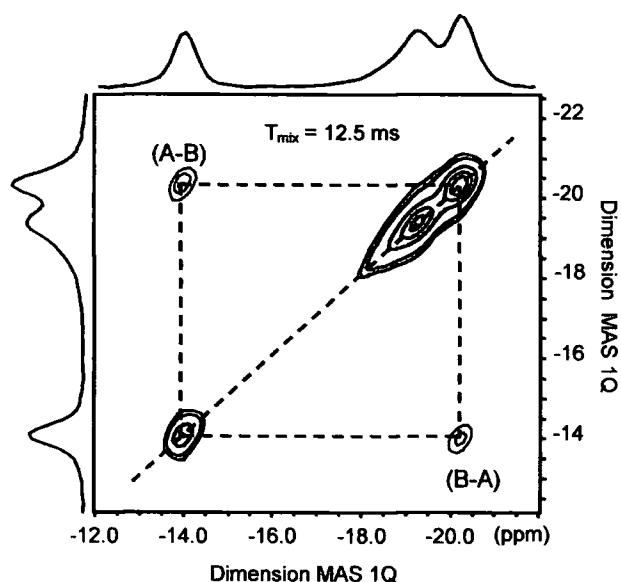
Figure 3.7. 2D RFDR spectrum of a mixture of α-$Mg_2P_2O_7$ and β-$Mg_2P_2O_7$, with A and B referring to the different phosphorus sites of α-$Mg_2P_2O_7$ as shown in fig. 3.6. Note that off diagonal peaks only occur between resonances in the same crystallographic phase.

This spectrum clearly highlights the lack of correlation peaks from different phases, and shows how RFDR spectra are interpreted, with lines being drawn horizontally and vertically from the off-diagonal peaks to the points where they intercept the diagonal, showing which peaks are correlated to one another.

3.3.2 2D POST-C7

Like the RFDR experiment, this experiment also utilises through-space dipolar couplings. However, there are a number of important differences to the RFDR experiment. Firstly this experiment uses double-quantum excitation and reconversion. Double-quantum excitation can only be achieved by a strongly coupled pair of spins (i.e. close in space), so that this effectively works as a filter from resonances due to single spins. This means that the full 1D MAS spectrum does not appear along the diagonal and fewer off-diagonal peaks are present, giving a 'cleaner' spectrum. It should be noted here that although the 1D MAS spectrum does not appear along the diagonal, autocorrelation peaks which arise when a given atom in an asymmetric unit is close in space to the analogous atom in another asymmetric unit do appear. The 2D POST-C7 spectrum for $Mg_2P_2O_7$ is shown in fig. 3.8.
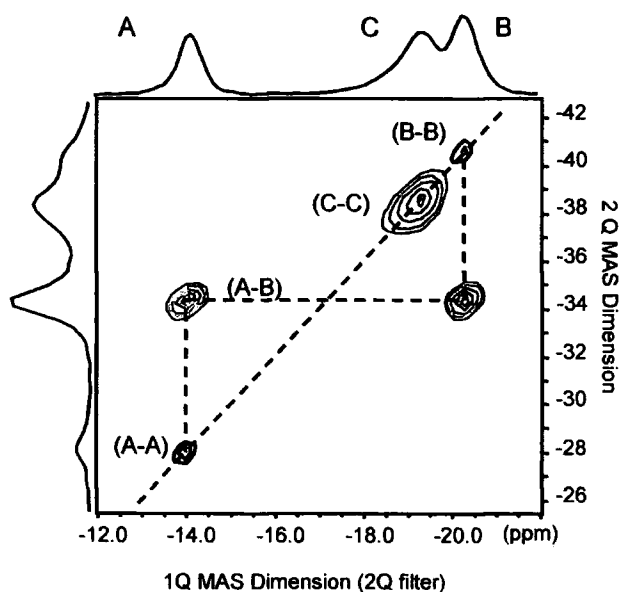
Figure 3.8. 2D POST-C7 spectrum of a mixture of α-$Mg_2P_2O_7$ and β-$Mg_2P_2O_7$, which is described in the text. $T_{mix} = 600$ μs.

As can be seen in fig. 3.8 correlation peaks are seen between the two phosphorus sites of α-$Mg_2P_2O_7$, while an autocorrelation peak is seen along the diagonal for the single phosphorus site of β-$Mg_2P_2O_7$ (C–C). Autocorrelations are seen for the two α-$Mg_2P_2O_7$ phosphorus sites, as

one site A is close to another site A in the structure and the same is true for site B. Another difference between the POST-C7 spectrum and the RFDR spectrum is the way they are read. For the POST-C7 spectrum horizontal lines are drawn to show which resonances are close in space. In the case of P_2O_7 groups phosphorus atoms in the same group are 3 Å apart with an associated dipolar coupling of ~700 Hz, with phosphorus atoms in different groups being at least 4 Å apart and having dipolar couplings of ~300 Hz. By drawing vertical lines on the spectrum through peaks, the number of unique sites can be found, in this case three. However, as will be seen later, in complicated cases determining the number of unique sites unambiguously may not be as easy as this.

3.3.3 2D POST-C9

The POST-C9 experiment utilises through-bond J-couplings by first removing both the dipolar and J-couplings and then selectively reintroducing the J-couplings. The spectra obtained are similar to those given by RFDR experiments, utilising a 1D MAS-1D MAS correlation and therefore producing a 1D MAS spectrum along the diagonal. Lines drawn horizontally and vertically from the off-diagonal peaks to the points where they intercept the diagonal show which peaks are correlated to one another. The advantages of experiments which use through-bond couplings are that these categorically show that the different atoms are in the same molecule or ion, and so they can be used to complement any conclusions from the experiments using through-space couplings. Intermolecular or inter-ionic peaks would not occur (except, perhaps, through hydrogen bonds), and so simpler spectra are obtained than when dipolar interactions are seen.

3.3.4 2D refocused-INADEQUATE

Like the POST-C9 experiment, the refocused INADEQUATE experiment is also a through-bond J-coupling experiment. It uses double-quantum excitation as a filter, so that the 1D MAS spectrum does not appear along the diagonal, meaning fewer resonances are present in the spectra obtained from a refocused INADEQUATE experiment when compared to the POST-C9 experiment. As can be seen below in fig. 3.9, the refocused INADEQUATE experiment gives much clearer results than the POST-C7 experiment, though less information. Like the POST-

C7 experiment, couplings are seen from close sites (although here actual bonding interactions are shown to exist), but unlike the POST-C7 the refocused INADEQUATE spectrum does not show longer-distance non-bonded couplings. The refocused INADEQUATE spectra show pairs of atoms that are in the same chemically bonded group, with the resonances lying on the same horizontal line. Again autocorrelations lie along the diagonal. This experiment is especially useful for complicated cases where a simplification (which frequently appears as an enhancement of resolution) is needed over experiments such as POST-C7.
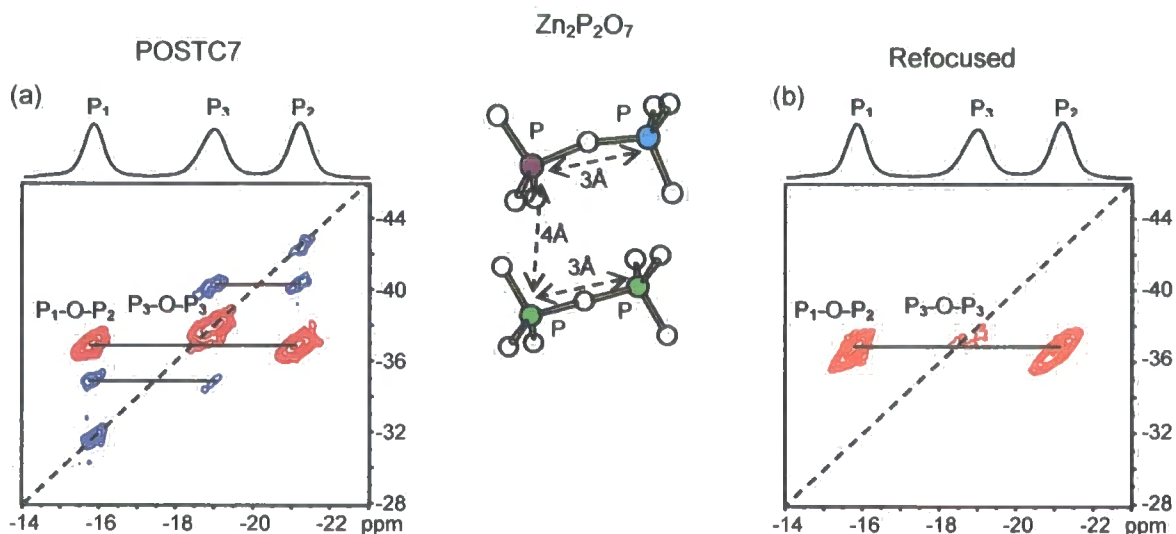
Figure 3.9. The 2D (a) POST-C7 and (b) refocused INADEQUATE spectra of $Zn_2P_2O_7$ as discussed in the text.

47

3.4 2D Conclusions

Four 2D solid-state NMR experiments have been presented above, each giving a different type of spectrum. The information given is perhaps best summarised in diagrammatic form, as in fig. 3.10. This figure shows the types of interaction seen using the various experiments, and whether the chemical shifts of individual atoms are seen, i.e. if the 1D MAS spectrum appears along the diagonal of the 2D spectrum. Many other 2D NMR experiments exist, each with their own relative merits, but the experiments given here were used because each gives an extra bit of information, required to solve the problems presented in Chapter 5.

3.5 Acknowledgements

I would like to thank Dr Franck Fayon and Prof Dominique Massiot for all the time, effort, help and knowledge they gave in setting up the 2D pulse sequences presented in this chapter.
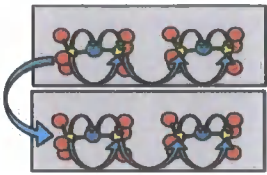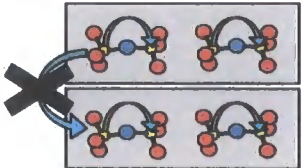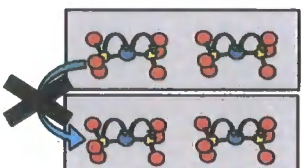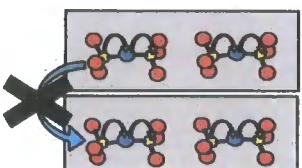
	All the interactions that are present in a static one pulse solid-state NMR experiment.
	RFDR experiments show through-space dipolar interactions, but not dipolar interactions between different crystallites. Resonances from single atoms are seen with this experiment (i.e. the 1D MAS spectrum is seen along the diagonal). *J*-couplings are not removed by this experiment, but their relative magnitude means they have no effect on the spectra obtained.
	POST-C7 experiments show through-space dipolar interactions, with a DQ filter 'removing' resonances from single atoms. In theory interactions between different crystallites can be seen, but only relatively short range interactions are seen, so in practice inter-crystallite interactions are not seen. Again, *J*-couplings are not removed (see the RFDR experiment above).
	POST-C9 experiments show through-bond *J*-couplings. These couplings are weak, so only short range interactions are seen. This experiment also gives rise to resonances from single atoms (see the RFDR experiment above).
	Refocused-INADEQUATE experiments show through-bond *J*-couplings. Again, these interactions are weak, and so only short range interactions are seen. Like the POST-C7 experiment this experiment also contains a DQ filter to remove resonances from single atoms, so the 1D MAS is not seen along the diagonal.

Figure 3.10. A table of the different information given by different pulse sequences used in this work.

3.6 References

(1)   States, D. J.; Haberkorn, R. A.; Ruben, D. J. *J. Magn. Res.* 1982, *48*, 286-292.

(2)   Keeler, J.; Neuhaus, D. *J. Magn. Res.* 1985, *63*, 454-472.

(3)   Bennett, A. E.; Ok, J. H.; Griffin, R. G.; Vega, S. *J. Chem. Phys.* 1992, *96*, 8624-8627.

(4)   Lee, Y. K.; Kurur, N. D.; Helmle, M.; Johannessen, O. G.; Nielsen, N. C.; Levitt, M. H. *Chem. Phys. Lett.* 1995, *242*, 304 - 309.

(5)   Hohwy, M.; Jakobsen, H. J.; Edén, M.; Levitt, M. H.; Nielsen, N. C. *J. Chem. Phys.* 1998, *108*, 2686-2694.

(6)   Heindrichs, A. S. D.; Geen, H.; Giordani, C.; Titman, J. J. *Chem. Phys. Lett.* 2001, *335*, 89-96.

(7)   Hardy, E. H.; Verel, R.; Meier, B. H. *J. Magn. Res.* 2001, *148*, 459-464.

(8)   Lesage, A.; Bardet, M.; Emsley, L. *J. Am. Chem. Soc.* 1999, *121*, 10987-10993.

Chapter 4

AM_2O_7 Materials – Literature Review

4.0 Introduction

Since the discovery and description of unusual thermal expansion in $ZrV_{2-x}P_xO_7$ and related phases[1-3] there has been considerable interest in compounds of the general type AM_2O_7 (A = Ti, Zr, Hf, Mo, W, Re, Si, Ge, Pb, Sb, Ce, Th, Np and Pu, M = V, P and As). [4-6] The first study of these materials was carried out by Levi and Peyronel on ZrP_2O_7, who concluded that this material existed with a simple cubic structure at room temperature, as shown in fig. 4.1.[7]
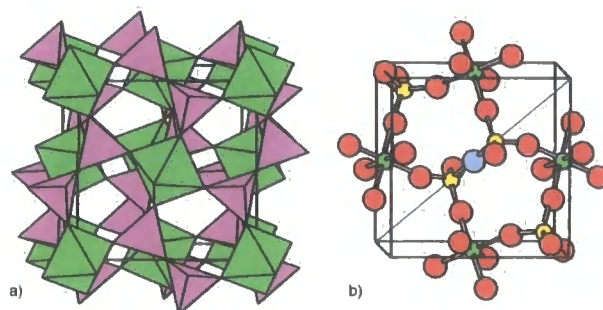
Figure 4.1. The basic cubic structure that all AM_2O_7 materials were initially believed to have.[7] (a) AO_6 octahedra corner sharing with MO_4 tetrahedra; (b) ball and stick model (A, M and O) with the bridging oxygen shown in blue.

This 'ideal' structure can be related to the structure of NaCl, with AO_6 groups centred on the Na site and the bridging O of the M_2O_7 group on the Cl site. The symmetry of the M_2O_7 group lowers the overall symmetry from $Fm\bar{3}m$ to $Pa\bar{3}$. This structure can also be described simply as corner sharing AO_6 octahedra and MO_4 tetrahedra, with the tetrahedra themselves sharing one corner to form M_2O_7 units. In this structure the bridging oxygen of the A_2O_7 group lies on a $\bar{3}$ site, constraining the A–O–A angle to be 180°. However it was realised by several workers that this 'ideal' structure would lead to unrealistically short M–O–M bridging bond lengths. Vollenke *et al.* gave the first solution to this problem, which was that a number of these systems had a superstructure with a cell edge three times greater than the smaller cubic cell.[8] The driving force for this is that the 180° angle is not energetically favourable, with the normal range for such angles being 130°-160° and invariably considerably less than 180°. The energy gained from achieving these non linear bond angles is the driving force for the formation of the

superstructure. For a number of these materials the reflections, in the X-ray powder pattern, from the superlattice have an intensity which is only ~1% of those of the strongest subcell peaks. The reason for these reflections being so weak is that the superlattice reflections arise principally from the lighter atoms present in the structure (O), while the heavy atoms (V, Zr) are in essentially the same position as they are at high temperature, i.e. it is the heavy atoms which give rise to the strong subcell reflections.

For the majority of the AM_2O_7 materials, heating (i.e. adding energy to the system) results in at least one phase transition with the high temperature structure believed to be the basic cubic structure, as was originally proposed by Levi and Peyronel.[7] However, the nature of the superstructures of these materials is unclear. Owing to their relative complexity and the weak supercell reflections, only a few have had their full structures determined: ZrV_2O_7 by single crystal methods (section 4.2.2);[9] SiP_2O_7 by ^{31}P solid-state NMR and single-crystal methods (section 4.1.1);[10-12] TiP_2O_7 by single crystal, powder XRD and ^{31}P solid-state NMR methods (section 4.2.1).[5,13,14] All three of these superstructures have space group $Pa\bar{3}$ (the same space group as the ideal high temperature form). This fitted in with the apparent assumption in the literature that all of these materials existed with space group $Pa\bar{3}$. However, recent work by Losilla and co-workers[4] questioned this, reporting that the structure of γ-GeP_2O_7 was pseudo-cubic and so of lower symmetry than $Pa\bar{3}$. This has also been shown to be the case for ZrP_2O_7, HfP_2O_7 and SnP_2O_7 in this study, and will be discussed later (section 5.1, 5.2 and 5.3 respectively).[15,16] This shows that, although these materials are all structurally related, changing the A^{4+} metal ion results in a subtly different structure. This is perhaps highlighted by fig. 4.2, which shows a plot of the subcell cell edge against the radius of the M^{4+} metal ion. In this figure it can be seen that as the atomic radius of the metal increases the cell parameter of the AM_2O_7 material increases. However, the dependence of the cell parameter on $r(M^{4+})$ is not simple. It can be seen, for example, that there is a clear difference between materials containing group 14 metals, group 3-5 metals and the rest of these materials.
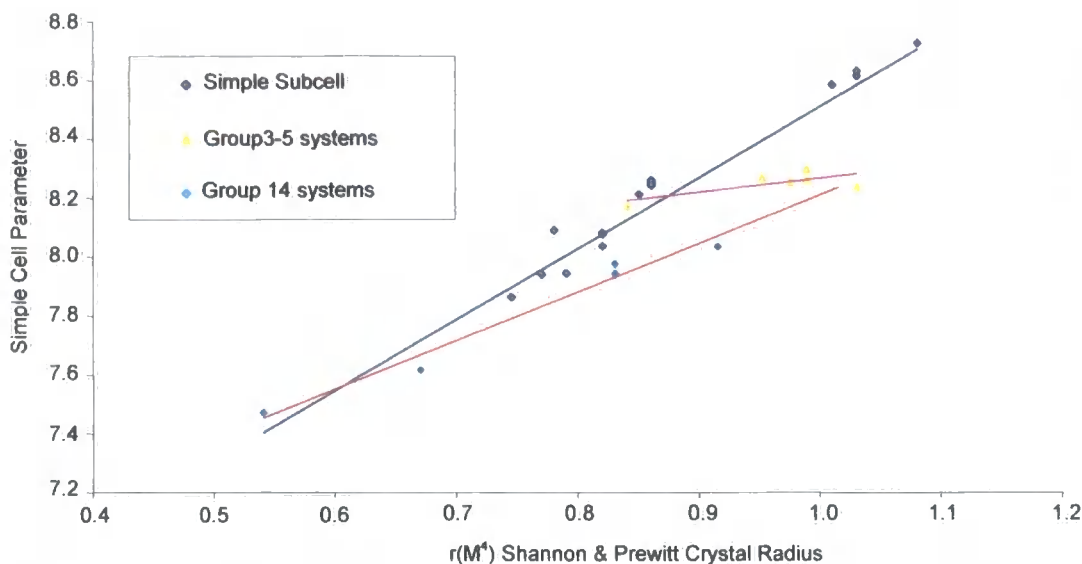
Figure 4.2. A plot showing the dependence of cell parameter on r (M^{4+}) with a plot of the subcell cell parameter vs. metal 4+ ion radii. It can be seen three separate trends are present as described in the text. Group 14 elements (Si, Ge, Sn, Pb) and $M^{3+}M^{5+}$ systems ($Sb^{3+}Sb^{5+}$, $Sb^{3+}Ta^{5+}$, $Bi^{3+}Sb^{5+}$, $Bi^{3+}Nb^{5+}$, $Bi^{3+}Ta^{5+}$, $Nd^{3+}Ta^{5+}$, $Eu^{3+}Nb^{5+}$, $Eu^{3+}Ta^{5+}$) have been separated.

In terms of the three materials which have presently had their structures elucidated the phase transition from the ideal high temperature cubic form to the room temperature 3x3x3 superstructure preserves the point group, but destroys 26/27 of the translational symmetry elements and 2/3 of the threefold axis. This symmetry reduction allows four of the six crystallographically unique M_2O_7 groups in the unit cell to bend away from 180° (fig. 4.3).
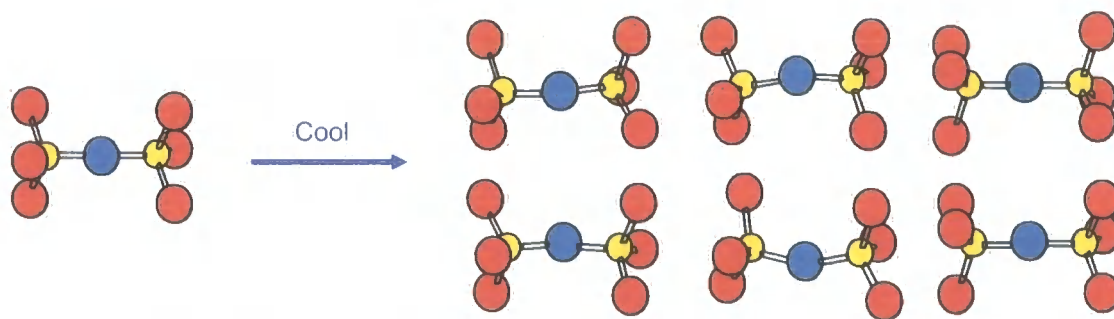
Figure 4.3. The $V_2O_7^{4-}$ groups of ZrV_2O_7. At high temperature only one type exists in the structure with a V–O–V bond angle of 180°. On cooling six distinctive groups exist with bond angles ranging from 159.3° to 180 °.

This transition leads to the space group symmetry being retained, i.e. $Pa\bar{3}$ throughout (as stated above this is not the case for all of these materials as will be seen below in the review of literature on these materials). The superstructure that results is shown below in fig. 4.4. Using symmetry arguments it is possible to construct a chart (fig. 4.5) of possible space groups for the

low temperature structure. This shows that the 3 x 3 x 3 superstructure could exist in one of twelve possible space groups. For each of these space groups the number of unique phosphorus sites can be calculated and this has been used in a number of ^{31}P NMR studies, such at that by Losilla *et al.*,[4] to show which space group the superstructure exists in. [5,11,12,15] These studies, along with others, will be discussed further below.
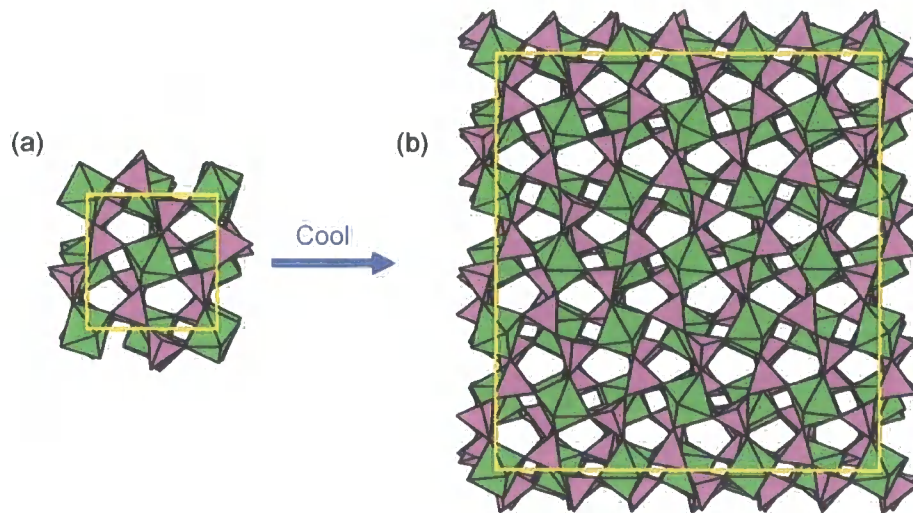
Figure 4.4. A schematic of the (a) cubic high temperature ideal structure of AM₂O₇ materials and (b) the room temperature superstructure.
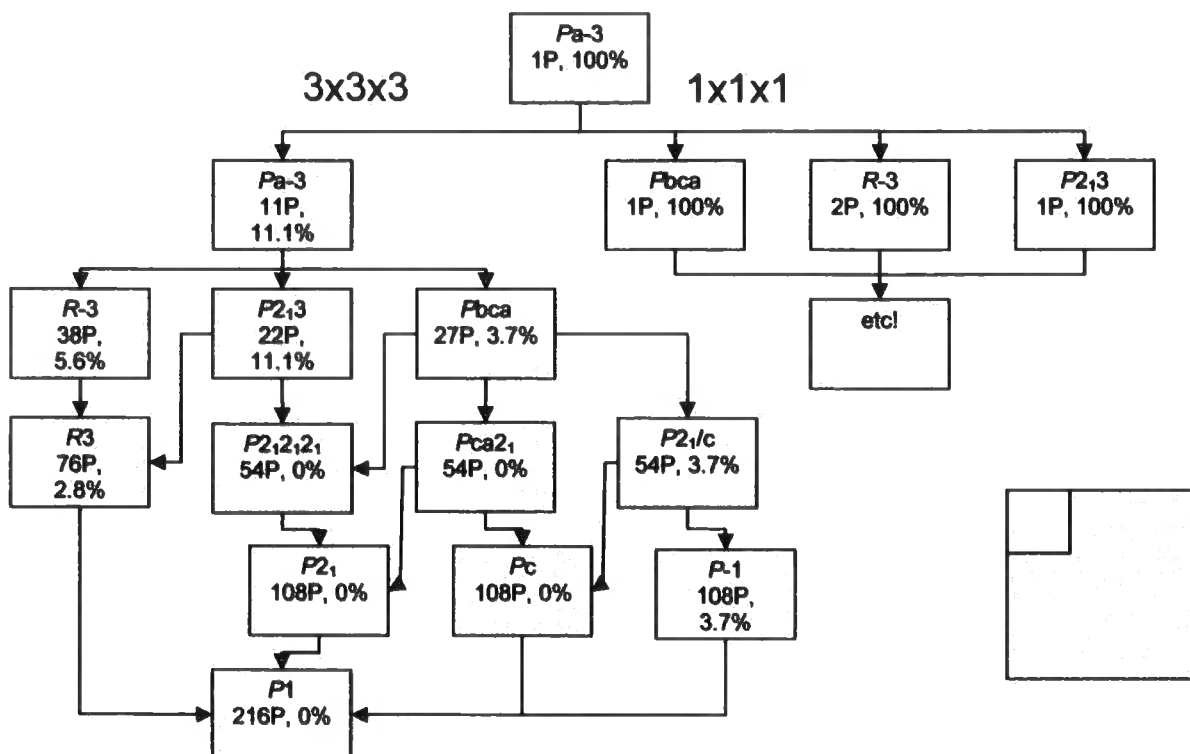
Figure 4.5. Table of allowed space groups for both the   and the [3 × 3 × 3 supercell], showing the number of unique phosphorus sites in the asymmetric unit, and the percentage of these that are in a $P_2O_7^{4-}$ unit with a 180° P–O–P bond angle.

4.0.1 Negative Thermal Expansion (NTE)

It is common knowledge that for the vast majority of materials, expansion will be observed as they are heated. In simple terms this can be described in terms of the asymmetric shape of a typical interatomic potential well (fig. 4.6). So, for a simple diatomic molecule as the temperature is increased higher energy vibrational levels are populated leading to an increase in interatomic distance. For larger systems, such as most inorganic solids, the entire phonon density of states as a function of temperature must be considered, but the simple picture is still true in general: the population of higher energy vibrational levels leads to positive thermal expansion. However there are certain groups of materials that exhibit the unusual property of Negative Thermal Expansion (NTE). In these materials other factors in their structures dominate the thermal expansion of chemical bonds.
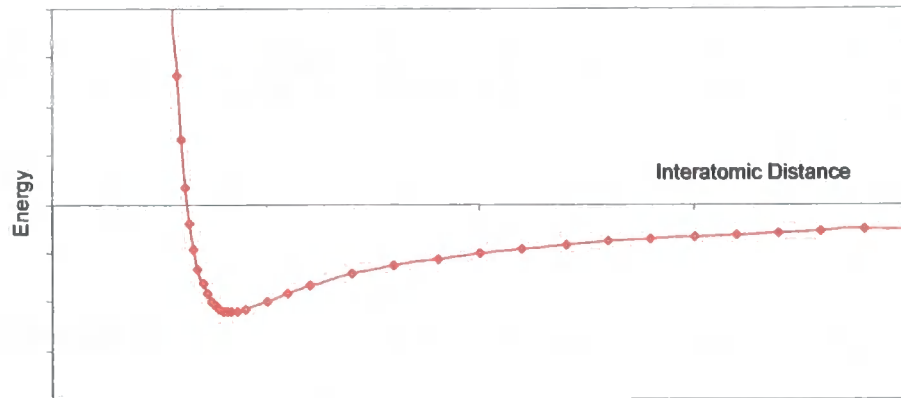
Figure 4.6. Potential energy curve for a typical chemical bond.

The coefficients of thermal expansion are defined below in equations 4.1 and 4.2:

$$\alpha_l = \frac{l_T - l_0}{l_0(T - T_0)}$$
(Equation 4.1)

$$\alpha_v = \frac{(V_T - V_0)}{V_0(T - T_0)}$$
(Equation 4.2)

Where, T_o and T are the start and end limits of the temperature range measured, and l_o, l_T, V_o and V_T are the cell parameters and volumes associated with those temperatures.[3]

NTE materials have a number of possible potential uses, mainly when used as part of a composite material displaying either zero or controlled thermal expansion.[17,18] Possible uses include zero-expansion heat sinks, printed circuit boards to match the properties of silicon, dental applications and substrates for high precision optical applications.[2,19,20]

The origins of NTE and the mechanisms which allow some materials to display this property are discussed below for the AM$_2$O$_7$ family.

4.0.2 Origins of Negative Thermal Expansion

There are at least four mechanisms which can bring about negative thermal expansion, with these four being discussed in this section:

(i) NTE due to phase transition, using tetragonal $PbTiO_3$ as an example. At temperatures above 490°C $PbTiO_3$ is cubic, being made up of regular PbO_{12} and TiO_6 polyhedra. In the tetragonal form (below 490°C) the TiO_6 octahedra contain alternate short and long bonds, extending in linear chains along the c-axis, which can perhaps be considered as single and double bonds, and bonds of equal length along the a and b axes. Above 490°C all of these Ti–O bonds are of equal length. Work by Brown[21] and O'Keefe,[22] which was an extension of Pauling's work, has shown that the contribution to the overall valence sum for a given bond can be approximated by equation 4.3;

$$v = \exp\left[\frac{(r_0 - r)}{0.37}\right]$$ (Equation 4.3)

where r_0 is a constant for a given E–X combination of elements. This gives a bond length - bond strength relationship as shown in fig. 4.7.
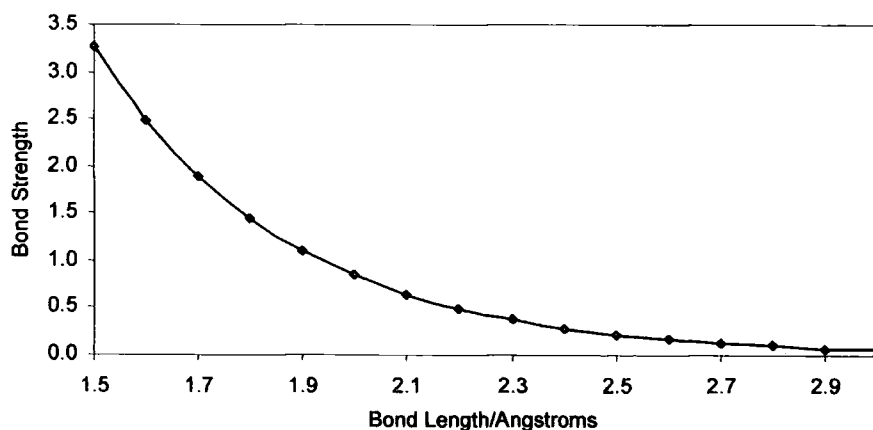
Figure 4.7. The form of a typical bond length-bond strength plot.

From this it is clear that as unequal bonds in a polyhedron become equal, their mean bond length decreases. It is obvious then that the c-axis (which is longer than the a and b axes below

490°C), will become shorter with increasing temperature, i.e. the average bond distance of a single and triple bond is longer than that of a double bond. In $PbTiO_3$ positive thermal expansion always occurs along the *a* and *b* axes but the NTE along the c-axis outweighs this causing a small volume contraction up to the phase transition.

(ii) Phonons. When heat is applied to a substance longitudinal vibrations increase causing an increase in bond length, however, upon heating transverse vibrations also increase. In some cases, the structure can be such that the overall contribution to thermal expansion from the transverse vibrations can outweigh the longitudinal vibrations, and can result in NTE. Using an M–O–M set-up for an example, it is clear that if the M–O distance stays essentially the same then the non-bonded M–M distance will decrease as a result of a transverse vibration (fig. 4.8), as opposed to an increase from longitudinal vibrations.
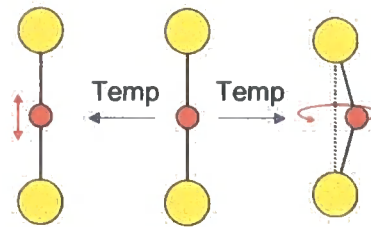
Figure 4.8. An M–O–M bond showing longitudinal and transverse vibrational modes.

This relationship between phonons and thermal expansion is put on a formal basis by the Gruneisen relationship (equation 4.4) which relates the volume coefficient of thermal expansion of a material (eqn. 4.2) to its volume (V), specific heat at constant volume (C_v) and isothermal compressibility (K).[23,24]

$$\alpha_v = \frac{\gamma C_v K}{V}$$

(Equation 4.4)

The Gruneisen parameter, γ, typically lies in the range one to three and is related to the anharmonicity of a typical crystal potential,[3] with;

$$\gamma = \frac{-d(\ln v)}{d(\ln V)}$$

(Equation 4.5)

Taking this into account it is clear that if the frequency, v, of a vibrational mode of a material decreases with volume decrease, the mode will possess a negative Gruneisen parameter, and, from equation 4.4, this will lead to a negative contribution to the overall thermal expansion. Transverse vibrational modes are generally of lower energy than longitudinal vibrational modes, and are preferentially excited at lower temperature, and can be the main factor contributing to the overall Gruneisen parameter at lower temperature, leading to NTE. The most commonly known example of a NTE material due to transverse vibrational modes is hexagonal ice, which displays NTE at very low temperatures.[25]

(iii) Magnetic transitions can give rise to materials with very low thermal expansion. Materials with significant magnetoelastic coupling can have large contractions associated with changes to their magnetic structure, which outweigh the normal phonon driven thermal expansion. Such materials include Lu_2Fe_{17} and Y_2Fe_{17}.[26]

(iv) Rigid Unit Modes (RUMs). Megaw[27] was the first to give the explanation of coupled rotation of relatively rigid corner sharing polyhedra for the temperature dependence of the unit cell volume for an inorganic structure. This theory was later developed further in a number of studies,[28-36] and culminated in Dove & co-workers' definition of rigid unit modes (RUMs)[28-32] that are rocking motions of polyhedra that do not change shape, and quasi-rigid modes (qRUMs) that are rocking motions of polyhedra where small changes in polyhedral shape occur. These can be best described by using the picture of a framework lattice made up of corner-sharing polyhedra, as shown in fig. 4.9.
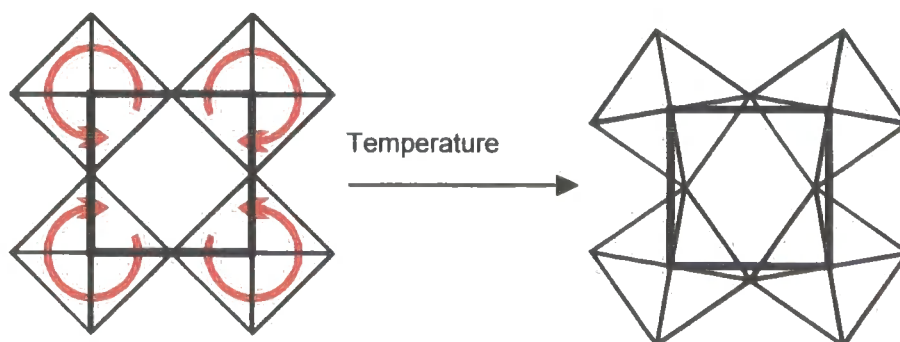
Figure 4.9. Diagrammatic representation of a framework lattice made up of corner-sharing polyhedra.

Again, using the example of an M–O–M linkage, the volume of the 2D structure in fig. 4.9 will be largest when the M–O–M bond angles are 180°. Rocking of the polyhedra bends the M–O–M linkages away from 180° and leads to a volume reduction of the structure. In RUMs this is brought about with no change to any of the bond lengths or bond angles within the polyhedra. In qRUMs this rocking of the polyhedra brings about small changes to bond lengths and bond angles within the polyhedra. The polyhedra in such structures contain strong M–O bonds and relatively short O–O distances, with the polyhedra being connected by relatively 'soft' M–O–M hinges (the bending potential of these linkages can be as much as 100 times weaker than the stiffness of individual polyhedra).[3] The methodology of Welche et al.[33] shows that the area of a unit cell (using the polyhedra shown in fig. 4.9 as an example) for a tilt angle, θ, is given by;

$$A(\theta) = A_0 \cos^2 \theta \approx A_0 (1 - \eta_A \theta^2) \qquad \text{(Equation 4.6)}$$

where η_A is a geometrical constant specific to a given mode of rotation and A_0 is the area of the cell for $\theta = 0$. If the angular fluctuations are then considered around an ideal high symmetry structure the thermal average of the distortion angle, $<\theta^2>_T$, will increase with increasing temperature, so that the overall unit cell area can be given by equation 4.7.

$$A(T) = A_0 (1 - \eta_A < \theta^2 >_T) \qquad \text{(Equation 4.7)}$$

so there is a negative contribution to the overall coefficient of thermal expansion. If one assumes a simple harmonic type motion, $A(T)$, can be related to the temperature, T, the moment of inertia of the rigid body, I, and the vibrational frequency, v, by equation 4.8;[33]

$$A(T) = A_0 \left(1 - \eta_A \frac{k_B T}{I v^2} \right) \qquad \text{(Equation 4.8)}$$

where k_B is the Boltzmann constant.

The ZrW_2O_8 family (chapter 6) is an example of structures that exhibits NTE that can be accounted for due to RUMs and qRUMs.

4.1 The Chemistry of Group 14 (A = Si, Ge, Sn, Pb) AM₂O₇ Phases

A review of the literature for each of the known AM_2O_7 materials is given below; starting with the AM_2O_7 materials containing group 14 metals. The structural chemistry of the materials is remarkable due to the large variety of possible phase transitions they can undergo, and it is hoped that this will become apparent in this review.

4.1.1 SiP₂O₇

SiP_2O_7 has been shown to possess a number of polymorphs, with monoclinic, tetragonal, hexagonal and cubic forms having been prepared.[37-40] The polymorph of relevance in our discussion of NTE materials is the cubic form which was the first member of the AM_2O_7 family to have its structure determined from single crystal data. This was done by Tillmanns et al. in 1973, using a combination of X-ray diffraction data and distance least-squares (DLS) modelling to describe the structure.[10] However, due to computational limitations and the relatively poor data available, only an isotropic refinement could be achieved. The Tillmanns et al. study showed the cubic form to have a room temperature 3x3x3 superstructure, with a space group $Pa\bar{3}$, and a cell edge, a = 22.418 Å. It was noted that a strong correlation was found between the P–O–P bond lengths and the P–O–P bond angles.

The cubic phase of SiP_2O_7 is also the first of these materials to have been studied extensively via 2D solid-state NMR.[5,11,12] Hartmann et al. studied a mixture of silicon phosphates via ^{31}P MAS and 2D exchange NMR.[11] The exchange experiment utilised dipole-dipole interactions to identify the neighbourhoods of non-equivalent phosphorus atoms, allowing the identification of different phases within the spectrum, and analysis of each one. For the cubic form of SiP_2O_7 it showed the presence of 11 different phosphorus environments, supporting the diffraction findings of a $Pa\bar{3}$ space group. In this space group two $P_2O_7^{4-}$ groups exist in which the apparent P–O–P bond angle is 180°, with one of these two groups containing inequivalent phosphorus atoms and the other containing two equivalent phosphorus atoms. These bond angles are said to be 'apparently' 180° because, as mentioned earlier, it is thought this bond angle is a time averaged effect and that the O atom of the P–O–P groups is oscillating around a central position.

A 2D TOBSY (Total Through-Bond-correlation SpectroscopY) experiment was performed by Iuliucci and Meier in a study to determine which three proposed reasons for the linearity of 11% of the P–O–P units, seen in these materials when the space group is $Pa\bar{3}$, was correct.[12] The three proposed reasons were: (i) a statistically disordered arrangement of locally bent configurations, (ii) a dynamic disorder where the units interconvert between bent structures on a time scale much slower than the (inverse) vibrational frequencies, and (iii) a linear structure, possibly with an extended thermal motion. The 2D TOBSY sequence[41] is a 2D exchange experiment which can be used to measure the angle between two CSA tensors (^{31}P in this case,[12] although the experiment is not exclusive to ^{31}P).[41] This is done by exploiting the knowledge about the orientation of the CSA tensor to the molecular frame, such that the bond angle can then be evaluated. To be able to obtain such results it is necessary that a certain amount of spectral resolution is present in the ^{31}P spectrum and that each individual shift can be resolved. In the case of SiP_2O_7, with its $Pa\bar{3}$ space group, 11 ^{31}P sites were expected (as had been shown to be the case by Hartmann et al.[11]) and seen experimentally, with all of the individual sites clearly resolved in the 2D TOBSY experiment, within a ^{31}P chemical shift range of -49 to -72 ppm (w.r.t. 85% aq H_3PO_4). The experiment showed the presence of two different types of P–O–P groups. Three groups were shown to have bent P–O–P angles, of around 148°, while one group was shown to have an angle of about 180°, i.e. it was linear. One group was omitted from the analysis as it contained degenerate resonances. This leaves one pair, which contained two phosphorus atoms crystallographically related to each other through an inversion centre, therefore having a bond angle of 180°. The study ruled out the possibility of a static disorder of bent bonds leading, on average, to a linear structure in the diffraction studies. This leaves the possibility of either a dynamic disorder with an exchange rate, at ambient temperature, of $k \gg 5000$ s^{-1} or a structure that is close to linear, possibly with an extended vibrational motion of the bridging oxygen. This later conclusion is given as the most probable as for the former one would expect a partial averaging of the CSA tensors, and this was not seen for the two phosphorus atoms in question. Helluy et al. also carried out a 2D NMR experiment which showed 11 unique phosphorus sites and were able to assign individual peaks to specific phosphorus sites.[5]

4.1.2 GeP₂O₇

GeP_2O_7 was first reported to have a cubic 3x3x3 unit cell with space group $Pa\overline{3}$.[8] Like SiP_2O_7, GeP_2O_7 has more than one polymorph, in this case three (the α, β and γ-forms). The α-form is prepared by heating α-$Ge(HPO_4)_2 \cdot H_2O$, and is then converted to the β-form through further heating, which yields the γ-form through yet further heating. However this last phase has proved very difficult to prepare in pure form, with this only having been achieved by heating α-GeP_2O_7 at 1000°C and 20 kbar. The α-form has very low crystallinity and its unit cell is not known, while the β-form is triclinic, with its crystal structure having been determined via single-crystal diffraction.[42] The cubic γ-GeP_2O_7 form is the polymorph of interest, and has been studied by Losilla *et al.* via powder X-ray diffraction and 1D MAS NMR.[4] Losilla *et al.*[4] showed that the powder XRD pattern of γ-GeP_2O_7 contains a number of reflections exhibiting splitting, which cannot be explained by the previously reported cubic 3 x 3 x 3 unit cell.[8,43] This splitting indicates that the true symmetry of this phase is monoclinic, or lower. This was confirmed by the ^{31}P NMR which resolved more than 35 peaks (in the range -42 to -62 ppm w.r.t. 85% aq. H_3PO_4), with many more being unresolved, and 'hidden' in the spectrum. A space group of $P2_1/c$ was proposed, although a lower symmetry space group could not be ruled out from the data, meaning a unit cell containing at least 270 crystallographically unique atoms (26 Ge, 54 P and 190 O). Cell parameters were given as, $a = 22.8647$ Å, $b = 22.8783$ Å, $c = 22.9429$ Å and $\beta = 90.328°$. It should be noted here that this monoclinic 3x3x3 cell was not a product of the high pressure synthesis, as the ambient pressure preparation also showed splitting of reflections and the ^{31}P NMR was also reported to be similar. High pressures were only employed to prevent P loss during synthesis.

γ-GeP_2O_7 was shown to remain monoclinic up to at least 750°C, and to expand with a positive thermal expansion coefficient, α_v, of 33×10^{-6} K^{-1}, with slight anisotropy. Even at high temperature γ-GeP_2O_7 is not seen to go to the simple cubic substructure observed for many of the AM_2O_7 compounds.

4.1.3 SnP₂O₇

Again, more than one polymorph of this structure has been seen, with Huang reporting two structure types.[6] These were described as types I and II where, type I contains P_2O_7 groups that are oriented randomly and, type II contains P_2O_7 groups that are ordered. Similar polymorphism was reported by Chaunac,[44] though in neither paper can the data be described as definitive. A recent study of what probably corresponds to the type II structure (which from here will simply be referred to as SnP₂O₇) by Gover *et al.* highlights the complexities of these structures and provides the starting point for the NMR data presented in section 5.3. Like GeP_2O_7, SnP_2O_7 is shown to expand upon heating, in this case up to the temperature at which it decomposes. An expansion rate between 305 and 1001 K of 1.25×10^{-5} K^{-1} has been quoted by Gover *et al.*[16] At room temperature X-ray, neutron and electron diffraction show the presence of reflections due a 3x3x3 superstructure. However, it appears this is not a cubic superstructure. The electron diffraction patterns show no extinction condition on the (hk0)* reflections, meaning that the expected *a*-glide of the $Pa\bar{3}$ space group is not present. A microdiffraction pattern was also presented, which revealed the presence of a 2_1 axis along both *a** and *b**. This suggested that the room temperature superstructure exists with a space group of $P2_13$ (or possible $P2_12_12_1$). This is the only AM_2O_7 material to have been reported with this (or a compatible lower symmetry) space group. The subcell reflections at room temperature correspond to a cell edge, $a = 7.9444$ Å. Upon heating SnP₂O₇ is seen to undergo two phase transitions by diffraction techniques, however, DSC shows no significant events, suggesting the transitions are of second order, or higher. The first of these transitions is at ~550 K, and is accompanied by a broadening/splitting of subcell reflections in the diffraction patterns, while a number of supercell reflections undergo a significant change. The subcell for this intermediate phase was described in terms of a triclinic cell ($a = 7.9804$ Å, $b = 7.9708$ Å, $c = 8.003$ Å, $\alpha = 90.08°$, $\beta = 90.38°$, $\gamma = 90.10°$). A full structure determination was not attempted with the data. A second phase transition was seen at ~830 K, and the subcell described in terms of a rhombohedral cell ($a = 8.0132$ Å and $\alpha = 90.18°$). It was not possible for Gover *et al.* to discount the possibility of incommensurate phases in the intermediate temperature regime. Even in the high temperature phase supercell reflections were reported, and at no point did the SnP₂O₇ structure revert to the simple cubic form. Upon cooling a hysteresis effect was seen, which was reported as being

independent of the cooling rate. This was not seen to indicate an irreversible transition, though, as cell parameters before heating and after cooling experiments remained the same, and the supercell peaks return to the same positions. The structural transitions reported by Gover *et al.* are different to any reported to date for other members of this family of materials.

It is of interest to note that the room temperature XRD pattern could be fitted to a cubic cell, but the neutron diffraction pattern showed small (but probably significant) discrepancies, which suggested a lower symmetry than cubic. This perhaps highlights the complexities of these systems, and shows a number of techniques need to be used, in conjunction with one another, to get a full structural picture. In section 5.3 solid-state NMR experiments, with this aim, are described.

4.1.4 PbP_2O_7

Very little has been reported in the literature in relation to PbP_2O_7. Vollenke *et al.* reported a room temperature superstructure, with $a = 24.10$ Å.[8] Huang *et al.* suggested that PbP_2O_7 be grouped with GeP_2O_7 and SnP_2O_7 due to a plot of the a-cell parameter *vs.* r (M^{4+}), which shows the points relating to the Pb, Ge and Sn pyrophosphates lie well below the straight line observed for others in the family (a being the value of the cubic cell edge, and r (M^{4+}) being the ionic radius of the metal in its 4+ state), see fig. 4.2. They suggested this was due to the fact the Ge, Pb and Sn have a d^{10} configuration, where the other M^{4+} metal ions do not formally contain electrons beyond their inert-gas cores. Recent studies by Tait[45] and Brindley[46] have shown PbP_2O_7 to exist at room temperature with a subcell of edge $a = 8.0374$ Å, and with an incommensurate superstructure. This material has been further studied here, see section 5.4.

4.2 The Chemistry of Group 4 (A = Ti, Zr, Hf) AM_2O_7 Materials

4.2.1 TiP_2O_7

TiP_2O_7 is perhaps the best understood of the transition metal pyrophosphates and has been studied with a number of techniques, including X-ray and neutron diffraction and solid-state 1D MAS and 2D ^{31}P NMR.[5,13,14,47] Soria et al.[47] presented 1D ^{31}P NMR spectra, in which nine phosphorus sites were resolved. They assumed a space group of $Pa\bar{3}$, and hence that two sites were obscured in their spectrum by peak overlap. A later study by Sanz et al.[14] used a combination of powder X-ray diffraction and ^{31}P 1D MAS NMR to study structural disorder in TiP_2O_7. It was found the ^{31}P NMR shift range was -35 to -55 ppm, and nine sites were again resolved, with intensity ratios which corresponded to those expected for a $Pa\bar{3}$ space group (which was again implicitly assumed). As for the Tillmann et al.[10] study of SiP_2O_7, the DLS method was used to obtain starting coordinates for structural refinement. Three models were derived and the best of these was then further refined by the Rietveld method using the GSAS set of programs.[48] Several bond distances were constrained with soft constraints. The lattice parameter was given as a = 23.6383 Å, similar to that found by McMurdie et al.[49] The study by Sanz et al. is of special interest in regard to P–O–P bond angles in the two groups containing oxygen atoms on a three-fold axis, requiring a bond angle of 180°. In their discussion they present data (in the form of chemical shift values) showing the oxygen atoms lying on the threefold axes have P–O–P bond angles of 150°. In their final conclusion they state 'The position of NMR lines is mainly given by the P–O–P angle, which has permitted us to deduce for all pyrophosphate groups P–O–P angles between 139° and 150°.' They also conclude that statistical disorder is the preferred reasoning for the anomalous thermal parameter deduced for the two oxygen atoms on the three fold axes, which is contrary to the study by Iuliucci and Meier on the SiP_2O_7 system.[12] Subsequent papers by Helluy et al. (1D MAS and 2D ^{31}P NMR) and Norberg et al. (X-ray diffraction) have given a more detailed account of the TiP_2O_7 superstructure, with the latter having constrained the two 'special' $P_2O_7^{4-}$ groups to P–O–P bonds with 180°.[5,13]

Helluy et al. have presented 1D MAS ^{31}P NMR spectra along with three different 2D ^{31}P NMR spectra for TiP_2O_7 (and SiP_2O_7) allowing a full spectral assignment of all 11 phosphorus sites.[5]

The 1D ^{31}P MAS NMR spectrum had eight clear resonances, as opposed to the Soria *et al.* and Sanz *et al.* studies which showed nine, and it was seen that altering the MAS spinning rate resulted in the splitting of the one broad resonance. In this study, no space group was assumed at the outset, but rather the space group was determined from the results obtained. It was found that the relative intensities of the resonances observed could be consistent with either a $Pa\bar{3}$ or a $P2_13$ space group. One way to distinguish between these space groups would be to look at the number of unique $P_2O_7^{4-}$ units; six would be present for the $Pa\bar{3}$ space group, eleven for the $P2_13$ space group. These can be 'observed' by utilising homonuclear J-coupling interactions, in this case $^2J_{iso}(^{31}P, {}^{31}P)$. This was done using the TOBSY pulse sequence, which gave a 2D spectrum (fig. 4.10) showing four clear P–P J couplings (A–E, B–D, C–F and I–J), plus one resonance (H) which although not fully resolved appeared to show the presence of a fifth pair, leaving one resonance (G) along the diagonal which would account for the sixth pair.
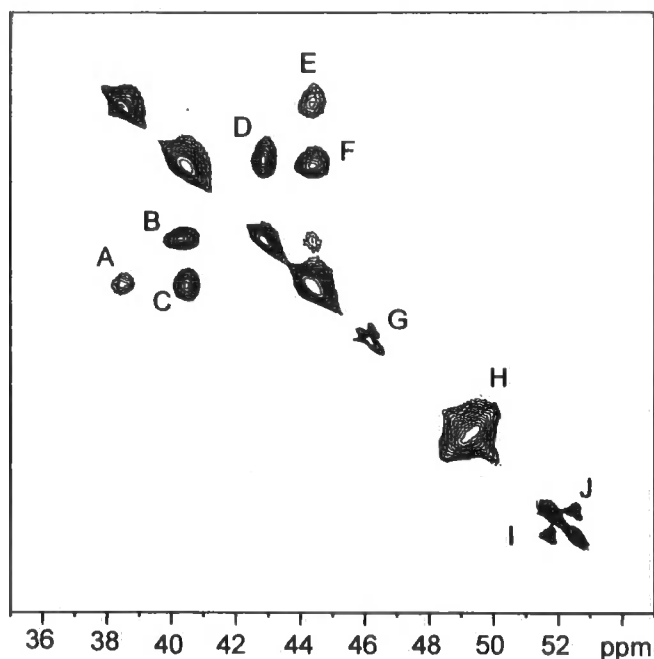
Figure 4.10. 2D TOBSY spectrum from fig. 3 of Helluy *et al.* [5] Reproduced with kind permission of the authors, ref 6.

This last pair was assigned as belonging to the P–O–P pair with the oxygen on a $\bar{3}$ site, so that the two phosphorus sites are equivalent, accounting for the lack of cross peaks. This was consistent with the $Pa\bar{3}$ space group. To obtain a full assignment of the peaks in the NMR spectrum, 2D ^{31}P ZQT RIL[50] (zero quantum transfer in the rotating inverse-laboratory), and SQ-

DQ^5 (single quantum–double quantum) correlation MAS NMR spectra, employing the $C7^{51}$ sequence for excitation and reconversion of double-quantum coherences, were recorded. These experiments work by removing all through-space dipolar interactions and selectively reintroducing the dipolar interactions of interest. The experiments were used in conjunction with knowledge of the nearest and next nearest neighbours in the structure, by using information from the isostructural SiP_2O_7. These experiments can then be used to look at short range interactions, intra-$P_2O_7^{4-}$ group, and longer range interactions, inter-$P_2O_7^{4-}$ group. By varying the mixing time (the time in which dipolar interactions are reintroduced) different range interactions are seen. For the ZQT RIL experiment a number of spectra were recorded, with increasing mixing times. The build up of cross peak intensity was then plotted as a function of mixing time (build up curves), and compared to build up curves calculated from the known structure of SiP_2O_7. However, the amount of overlap in the spectra makes it difficult to assign the individual peaks to specific ^{31}P sites. The SQ-DQ MAS experiment was carried out with excitation/reconversion periods that gave a spectrum that again showed not only short range ^{31}P–^{31}P interactions, but also longer range interactions, from nearest neighbour interactions (not intra- $P_2O_7^{4-}$ group). This allowed a full assignment of the 11 peaks to the eleven ^{31}P sites in the asymmetric unit. As stated in 4.1.1 this was also carried out for SiP_2O_7. Helluy et al.[6] also stated that ^{31}P resonance assignment should not be carried out on the basis of P–O–P bond angles, "local symmetry" arguments or similar, contrary to Sanz et al.[4,14] Helluy et al.'s viewpoint has been shown to hold for $Cd_3(PO_4)_2$.[52]

The $Pa\overline{3}$ space group has recently also been confirmed by single-crystal analysis.[13] This has shown that a room temperature 3x3x3 superstructure exists, but that it is more distorted relative to the high temperature cubic structure than the room temperature structure of ZrV_2O_7 (section 4.2.2). This is shown by the intensity of supercell reflections, the highest of which is reported to be 30% the intensity of the strongest subcell reflection, compared to just ~1% in the case of ZrV_2O_7. This is due to the TiO_6 octahedra and the PO_4 tetrahedra being slightly more displaced from their ideal high symmetry sites than the ZrO_6 octahedra and VO_4 tetrahedra of ZrV_2O_7, as well as relative scattering effects due to different metals being present in the different materials. This is most obvious in the M–O–M (M = P or V) bond angles involving the bridging oxygen in the $M_2O_7^{4-}$ groups but not the oxygen on a threefold axis. All Ti–O bond lengths were found to

be in the range 1.8884-1.9453 Å, and O–Ti–O angles were in the range 86.75°-92.81°. P–O$_{Ti}$ bonds were in the range 1.4893-1.5069 Å. The PO₄ tetrahedra have bond angles in the range 104.16°-113.61°. The four groups containing bent P–O–P groups have P–O–P bond angles ranging from 141.21° to 144.51°, and P–O$_P$ bond lengths of 1.575 Å, compared to 1.536 Å for the two P₂O₇$^{4-}$ groups containing P–O–P bond angles which are constrained to 180°. The two oxygen atoms from these latter groups show enlarged displacement parameters compared to the other oxygen atoms in the structure, indicating possible structural disorder, in keeping with the findings of Sanz et al.[14]

4.2.2 ZrV₂O₇

ZrV₂O₇ is one of the few vanadates known for these materials, and has had its structure fully solved from single crystal data (fig. 4.11).[9] It was shown by this study that ZrV₂O₇ fits the general theory relating to the structures of these materials, as explained earlier in section 4.0.

The space group of the room temperature phase was reported as being the same as that of the high temperature form, i.e. Pa3̄. This is shown in the single crystal data by systematic absences at 0kl, when k = 2n, although it should perhaps be noted that some relatively weak 'violations' of this were seen. These were accounted for as arising from multiple diffraction effects.

One feature of the room temperature structure is the remarkably narrow range of metal-oxygen distances. The average Zr–O is 2.0695 Å with a standard uncertainty of 0.0075 Å, and the range of Zr–O distances is only 2.055-2.084 Å. The average V–O$_{Zr}$ distance is 1.6757 Å with a
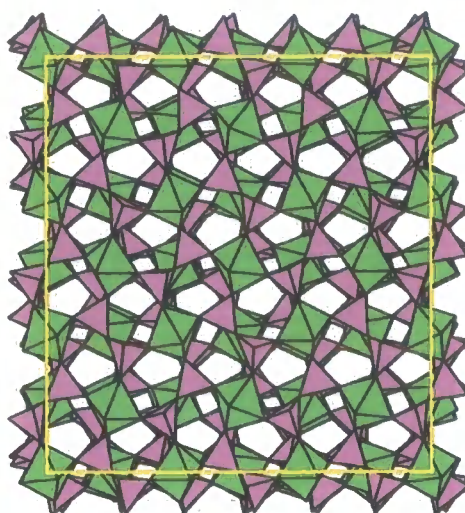
Figure 4.11. The room temperature 3x3x3 superstructure of ZrV$_2$O$_7$, made up of ZrO$_6$ octahedra and VO$_4$ tetrahedra.

standard uncertainty of 0.0046 Å, and a range of 1.665-1.682 Å. The internal bond angles of the ZO$_6$ and VO$_4$ polyhedra show minimal departure from ideal octahedral and tetrahedral values. The 72 ZrO$_6$ 90° angles show a range of 88.0-92.0° with a standard uncertainty of 1°, and the 66 VO$_4$ tetrahedral angles show a range of 108.3-110.6° with a standard uncertainty of 0.47°. The difference between the tetrahedral angles involving bridging O atoms (i.e. O$_v$–V–O$_{Zr}$) and nonbridging O atoms (i.e. O$_{Zr}$–V–O$_{Zr}$) is small, with an average difference of just 0.2°. The dependence of both Zr–O and V–O$_{Zr}$ distances on the Zr–O–V angle is small. This would suggest that the Zr–O–V bridges can be viewed as ideally flexible and little distortion of individual bond distances occurs as the bond is bent.

The bridging V–O$_v$ bonds of the V$_2$O$_7$ groups are systematically longer than the V–O$_{Zr}$ bonds, having an average distance of 1.7525 Å (uncertainty of 0.0076 Å). The range of bond distances is 1.740-1.762 Å, and it has been shown that this bond distance is dependent on the V–O–V bond angle, with linear bonds being shorter than bent bonds, as is shown in fig. 4.12. This can be related to the Si–O case, where the bond distance varies between 1.638 and 1.596 Å, as the bond angle varies between 120 and 180°. This has been attributed to increased d-orbital π-bonding contributions as the bond angle goes to 180°. In the case of ZrV$_2$O$_7$ the 3d orbitals are likely to be relevant in bonding, so that it may be assumed, using this argument, that as the V–O–V bond approaches 180° the V–O$_v$ bond distance will decrease. Another theory is that these effects are due to increased thermal motion in the bridging O atoms of the V$_2$O$_7$ groups, due to

the larger displacement parameters seen for oxygen atoms in V–O–V groups compared to those in V–O–Zr groups.
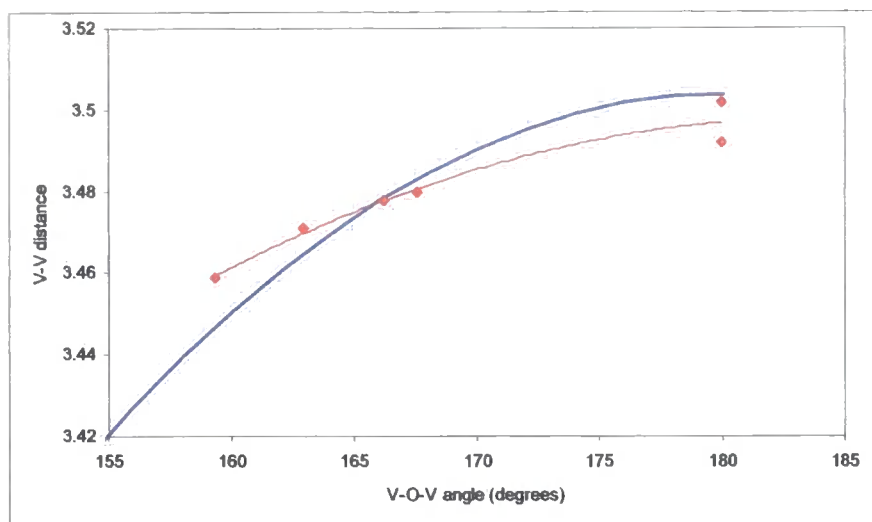
Figure 4.12. A plot showing the dependence of V–V bond distance with V–O–V bond angle. Reproduced from ref. 11 with permission from the authors.

The displacement parameters for the oxygen atoms on the threefold axis were not found to be significantly different to those of other oxygen atoms in V–O–V groups. Evans *et al.* considered deviations of the V–V vector from the threefold axis, the V–O–V bond angle and the torsion angle of the O_{Zr} atoms. The results suggested that the superstructure contains highly regular, essentially undistorted, octahedra. Therefore the major structural changes at phase transitions must involve rotations of these coupled polyhedra.

It is interesting to note the structure found experimentally by Evans *et al.* was a close match to that determined by 'purely geometric factors'.[9] So, as mentioned above, the true structure can be derived from the ideal structure by a coupled 3-D rotation of relatively undistorted polyhedral units. Some small distortions of the ZrO_6 and the VO_4 polyhedra are required by the structure topology, and it seems that many of the properties of ZrV_2O_7 are influenced by these small distortions.[3]

The single-crystal study by Evans *et al.* was supported by an electron diffraction study, which showed the presence of an *a*-glide plane in the room temperature superstructure, which is consistent with the $Pa\bar{3}$ space group seen.[9,53] Variable temperature studies were also conducted, which showed that ZrV_2O_7 undergoes two reversible phase transitions upon heating.

This was observed both from electron and neutron diffraction data, as shown by fig. 4.13. This plot was obtained from neutron data, as it is not possible to measure accurately the local temperature in electron diffraction studies. It can be seen from this that two phase transitions occur, the first at 77°C and the second at 102°C, with the material expanding with temperature through the first two phases, and then contracting as the temperature is increased when in its high temperature form. The low temperature phase is the 3x3x3 superstructure discussed above. On going through the first phase transition superstructure reflections are still seen by electron diffraction.[53] However, it appears this 'middle' phase is no longer a simple 3x3x3 superstructure, but actually an incommensurate superstructure. An incommensurate phase is one in which atoms in the unit cell do not repeat in exact integers, e.g. at the phase transition for ZrV$_2$O$_7$ the structure changes from a 3 x 3 x 3 superstructure to an incommensurate ~3 x ~3 x ~3 superstructure. This can be clearly seen in fig. 4.14, which shows the electron diffraction patterns for both the room temperature superstructure and the incommensurate superstructure. A close inspection shows that for the room temperature phase the low intensity (superstructure) maxima are evenly spaced (fig. 4.14a), while for the incommensurate phase (fig. 4.14b) it is clear that these superstructure maxima are not evenly spaced. The electron diffraction pattern for the high temperature phase showed that the low intensity reflections from the superstructure were no longer present. Similar work on ZrP$_2$O$_7$ is shown in section 5.1.3.
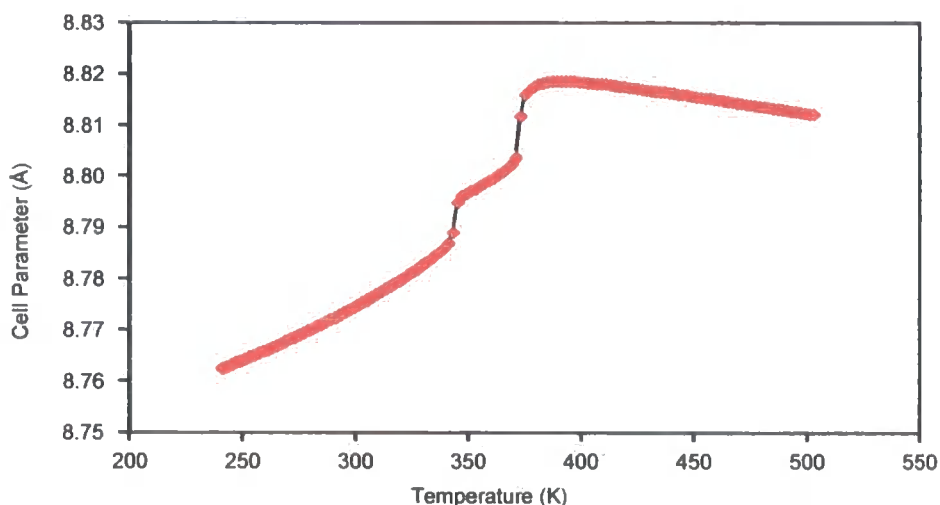
Figure 4.13. Plot of subcell cell parameter vs. temperature for ZrV$_2$O$_7$, derived from neutron powder diffraction.

Korthuis *et al.*[1] presented a ^{51}V MAS NMR spectrum for ZrV_2O_7. However due to the large amount of overlap of peaks the only definite conclusion that can be drawn from this spectrum is that the room temperature structure is not an ideal simple cube, as more than one vanadium site is seen. The spectrum has similarities to that presented in the same work for ZrP_2O_7, but there appears to be considerably more overlap in the ZrV_2O_7 spectrum, so it is not possible to attempt any correlation of the two structures on the basis of the NMR spectra. However, perhaps the most interesting ^{51}V NMR results presented by Korthuis *et al.*[1] are those at high temperature. Results at temperatures exceeding that of the second phase transition of ZrV_2O_7 apparently showed not one peak, as would be expected for the $Pa\overline{3}$ space group, but two peaks. Korthuis *et al.* remark that this is a characteristic of an axially symmetric quadrupole powder pattern and is consistent with observed first-order quadrupole satellite transitions (and so due to one unique ^{51}V site in the structure). Recent work by Hodgkinson and co-workers[54] on a sample of high crystallinity has seen the same effect, but their work suggests the possibility of the (apparent) two peaks being due to the presence of two sites in the high-temperature form. However, these latter studies are at an early stage, and further investigations are required before any conclusions can be drawn.

^{51}V NMR data collected as part of this study will be presented for ZrV_2O_7 in section 5.6.
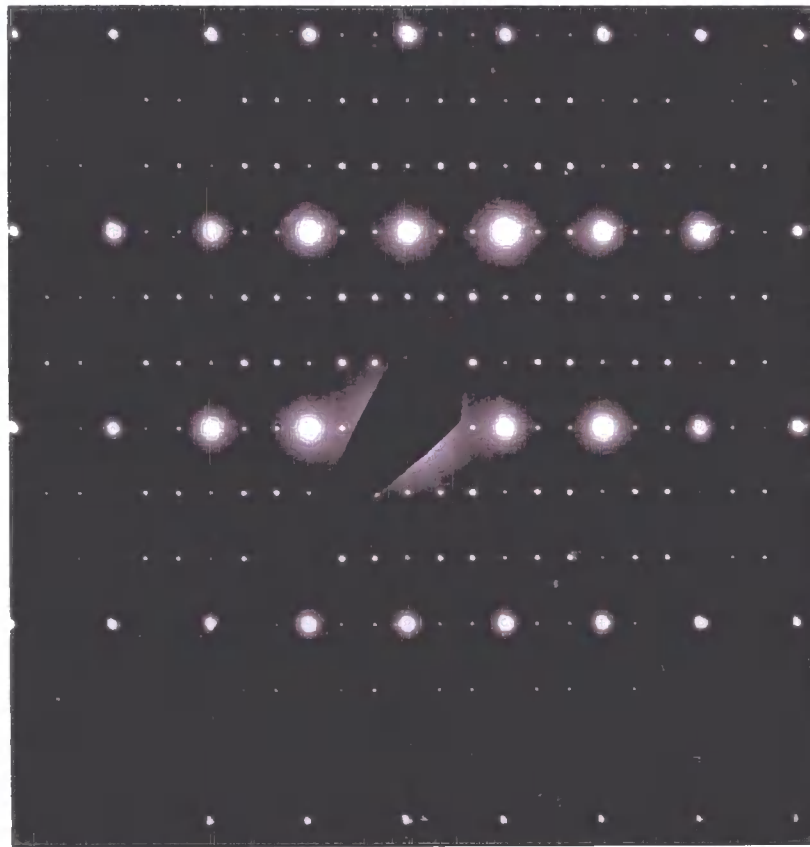
(a)
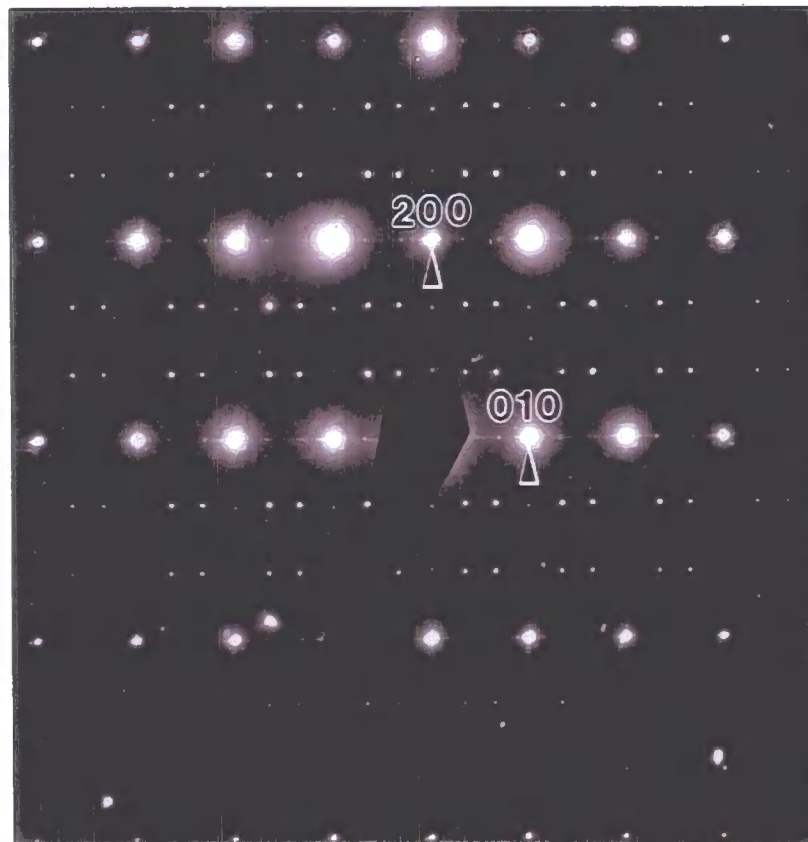
(b)

Figure 4.14. Electron diffraction maps of (a) the room temperature phase and (b) the intermediate incommensurate phase of ZrV_2O_7. (Reproduced from reference 11 with the kind permission of the authors.)

4.2.3 ZrP₂O₇

ZrP_2O_7 is the most studied of this family of materials,[1,7,8,15,43,44,55,56] and was in fact the first of all of them examined.[7] Vollenke *et al.* (1963) were the first to note the presence of a room temperature superstructure for this material, assigned a space group of $Pa\overline{3}$, and reported a cell edge $a = 24.72$ Å.[8] This space group has since been supported by a number of studies. Hagman and Kierkegaard (1969) noted a space group $Pa\overline{3}$, with subcell cell edge $a = 24.7422$ Å, and a further paper with a full single crystal analysis of ZrP_2O_7 was mentioned, but it appears this was never forthcoming.[43] Chaunac (1971) again confirmed the presence of a superstructure, again noting a space group $Pa\overline{3}$, with a cell edge $a = 24.735$ Å. Korthuis *et al.* used a multi-technique approach (X-ray and neutron diffraction and ³¹P MAS NMR) in looking at ZrP_2O_7, as part of a wider study of the $ZrV_{2-x}P_xO_7$ series.[1] They again cited a space group $Pa\overline{3}$, with the 1D ³¹P MAS NMR spectrum being interpreted in terms of 11 P sites arising from ZrP_2O_7, as would be expected for $Pa\overline{3}$, plus one impurity peak; a similar spectrum to that seen by Korthuis *et al.* is shown in fig. 4.15. This peak, at ~ -45 ppm, was not adequately accounted for, as there were no impurities visible in the X-ray diffraction pattern of this sample and only three very small reflections unaccounted for in the neutron diffraction pattern (the 'impurity peak' in the NMR accounts for ~7% of the spectrum and so would be expected to give rise to more than three minor reflections in diffraction), giving rise to the possibility that the space group assignment was incorrect in this case.

Further to this study, a structural refinement was presented from neutron data, assuming the $Pa\overline{3}$ space group, as [incorrectly] deduced from the ³¹P MAS NMR.[57] One phase transition was seen at 290°C. Below this temperature a superstructure was observed, and above this was seen to disappear. The high temperature phase was shown to have very low positive thermal expansion (3.5×10^{-6} K⁻¹), a space group $Pa\overline{3}$, and a cell edge $a = 8.2899$ Å (at 290°C). Zr and O2 are at the special positions (0, 0, 0) and (0.5, 0.5, 0.5) respectively.
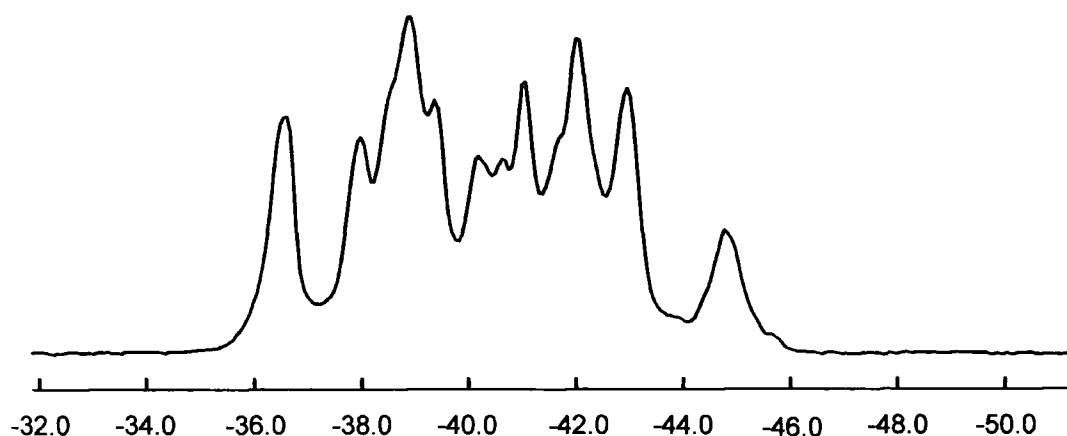
Figure 4.15. A ^{31}P MAS NMR spectrum of ZrP_2O_7. Similar to that seen by Korthuis et al.[1]

The oxygen atoms show large thermal vibration parameters perpendicular to the bonds: Zr–O1–P and P–O2–P, with O2 showing unusually large vibration. An attempt at structural solution of the low temperature superstructure was first done by refining the data using the coordinates published for SiP_2O_7.[10] This proved unsuccessful, so a DLS approach was used. This yielded an R_{wp} = 0.0887 for a fit to the $Pa\bar{3}$ space group, with cell edge a = 24.7424 Å. However, two recent publications, as part of this study, have shown that the assignment of the $Pa\bar{3}$ space group is incorrect, and these will be discussed further in section 5.1.[15,56]

4.2.4 HfP_2O_7

There is very little literature on HfP_2O_7. It has been shown to have a superstructure at room temperature, with cell edge a = 24.63 Å. Korthuis et al.[1] and Huang et al.[6] also reported studies on these systems, but these were very limited. A recent study by Tait has shown HfP_2O_7 has a unit cell edge at room temperature a = 24.64 Å, and exhibits low thermal expansion between 728 K and 978 K.[45]

Results regarding the structure of HfP_2O_7 will be presented as part of these studies in section 5.2.

4.2.5 HfV_2O_7

This structure was first studied by Baran who noted the presence of a room temperature superstructure, with cell edge a = 26.3 Å.[58] Korthuis et al. noted it displayed negative thermal expansion, but gave no details.[1] Turquat et al.[59] recently presented a full structural study of

HfV$_2$O$_7$, which showed it is not isostructural with ZrV$_2$O$_7$, but, like ZrV$_2$O$_7$, it is seen to exhibit two phase transitions. It was shown by electron diffraction that an a-glide plane is present in HfV$_2$O$_7$, although like the ZrV$_2$O$_7$ case, some forbidden reflections are seen.[59] Again, this was accounted for by the occurrence of double diffraction. Some reflections such as the (030) reflection, which is forbidden, appear and cannot be accounted for by double diffraction. However, a small tilt of the incident beam with respect to the crystallographic axis allows this reflection, and others to be understood. The (050) reflection in the supercell reflections cannot be accounted for by double diffraction when the structural model proposed for ZrV$_2$O$_7$ is used, with Zr replaced by Hf. Therefore it was concluded from the electron diffraction that a difference in structure must exist, although both have the same space group. X-ray diffraction showed the subcell had a cell edge a = 8.7530 Å, with average bond lengths V–O(1) = 1.64 Å, V–O(2) = 1.73 Å, and Hf–O(1) = 2.05 Å, though these were obtained from an unrealistic model. Two phase transitions were seen by DSC on heating. The first occurred at 340 ± 2 K and a second at 369 ± 2 K, while on cooling these two transitions were seen at 326 ± 2 K and 368 ± 2 K respectively, so a hysteresis effect exists for the first transition, suggesting it is a first-order transition. The DSC and X-ray diffraction findings were confirmed by variable temperature neutron diffraction. No conclusions regarding the middle phase (i.e. the phase between 340 and 369 K) were suggested, due to quality of data, although it is thought (by analogy to ZrV$_2$O$_7$) that this phase is an incommensurate superstructure.

4.3 The Chemistry of Other Transition Metal (A = Nb, Mo, W, Re) AM₂O₇ Phases

4.3.1 NbP₂O₇

The structural chemistry of NbP_2O_7 is more complex, due to the fact that it could potentially contain a mixture of Nb(IV) and Nb(V). Thus this gives rise to the question as to whether it is actually $Nb(IV)P_2O_7$, $Nb(V)P_2O_{7.5}$ or $Nb_{1-x}P_{2-y}O_{7+z}$. Added to the difficulties in making pure phase NbP_2O_7 it is no surprise to find this has been little studied,[60,61] with most of the literature actually referring to $Nb(V)P_2O_{7.5}$ and $Nb_{1-x}P_{2-y}O_{7+z}$.[60,62-65] Haider suggested the presence of $P_2O_7^{4-}$ groups via IR spectra, although this was reported for the compound $Nb_2O_5.2P_2O_5$ (i.e. $NbP_2O_{7.5}$), suggesting the presence of the Nb^{5+} cation.[62] A later study by Haider, using X-ray studies, indexed the cell as cubic, and found it to be isomorphous to ZrP_2O_7.[63] A cell edge $a = 8.073$ Å was found. Levin and Roth suggested that NbP_2O_7 was not cubic, but rather pseudocubic, with an approximate cell edge $a = 8.066$ Å.[64] In all of these studies niobium has been presumed to be in a pentavalent state. However, a recent study by Fukuoka et al. has shown NbP_2O_7 can be prepared with niobium in a tetravalent state, and that it exists with a space group $Pa\bar{3}$, with cell edge $a = 8.0809$ Å, and has a 3x3x3 superstructure. The presence of Nb^{4+} is revealed by the brown colour of the compound prepared and from magnetic measurements. UV spectroscopy shows one absorption band, which is apparently due to the d-d transition of the Nb^{4+} ion (d^1). This would not be seen for the Nb^{5+} (d^0). The Fukuoka et al. study highlights the problem of trying to obtain a pure sample of NbP_2O_7. In this case there were difficulties in removing the phosphoric acid used in its preparation, and it was shown that the average oxidation state of niobium in the structure is above +4 but below +5. Therefore some defects must have been present in the samples studied. Three possibilities are possible to account for these defects: (i) excess oxygen; (ii) niobium defect; (iii) phosphorus defect. The first model was stated as unlikely as the ZrP_2O_7 type structure has no room for the excess oxygen. This model would also lead to some Nb^{5+} cations being surrounded by seven oxygen atoms, which is highly unlikely due to the small size of this cation, and would see the formation of a square pyramid-like structure (though the veracity of this statement is questionable – see below). This was not consistent with the data. The niobium defect model also did not give a good fit to the data, meaning the phosphorus defect model must account for the observed

average niobium oxidation state. This model could be fitted well to the data. It was noted that when all the niobium ions are oxidised to Nb^{5+} the stress caused sees the disappearance of the superstructure, and the formation of a pseudocubic structure. However, due to the complexity of the problem and approximations used in its analysis these results can not be seen as definitive. In particular their statement that there is no room for excess oxygen in the structure is questionable. Sites do exist in this lattice at ~ 0.25, 0.25, 0.25 and are similar to the site occupied by the "extra" oxygen in the ZrW_2O_8 structure type.

4.3.2 MoP₂O₇

A single crystal study of MoP_2O_7 was presented by Leclaire *et al.*, in which the space group $Pa\bar{3}$ was assigned, with a cell edge a = 7.944 Å.[66] No evidence of a supercell was given, although high thermal factors were obtained for the oxygen atom of the P–O–P linkage, which is perhaps actually due to the presence of a superstructure. Haushalter *et al.* have subsequently shown the existence of weak reflections in the single crystal X-ray pattern of MoP_2O_7 indicative of a superstructure.[67] The superstructure appeared orthorhombic, rather than cubic, with *mmm* Laue symmetry, with a cell edge ~ 24 x ~24 x ~24 Å. The powder pattern presented by Lezama *et al.* would appear to support the presence of a superstructure, although this is not noted in the article.[68]

4.3.3 WP₂O₇

Teweldemedhin *et al.* have reported WP_2O_7 as existing with a space group $Pa\bar{3}$, and cell edge a = 7.947 Å, with no evidence of a superstructure.[69] The lack of a superstructure is also supported by the powder XRD pattern presented by Lezama *et al.*[68] This latter study was of WP_2O_7 and MoP_2O_7 which looked at their uses as potential catalysts due to relatively open structures of these materials. WP_2O_7, like MoP_2O_7, has the potential of being used for redox intercalation reactions, as tungsten can be either reduced or oxidised.

4.3.4 ReP$_2$O$_7$

It would appear only one study exists in the literature with respect to ReP$_2$O$_7$.[70] This shows that

this material has a cubic superstructure at room temperature, with a = 23.82 Å. No space group

was given, but it was noted as being isomorphous with ZrP$_2$O$_7$, and at the time of publication

this was assumed to be in space group $Pa\overline{3}$.

4.4 The Chemistry of Lanthanoids and Actinoids (A = Ce, Th, U, Np, Pu) AM₂O₇ Phases

4.4.1 CeP₂O₇

CeP_2O_7 was reported as part of a study by Vollenke et al.,[8] and was shown to exist with a space group $Pa\overline{3}$, having a room temperature superstructure, with a = 25.74 Å, although this material was not obtained as a pure phase. It would seem that since this publication no further structural study has appeared for this material. A recent study by Tait and co-workers has shown CeP_2O_7 exists with a cubic subcell, a = 8.5648 Å.[45] However a supercell could not be confirmed due to the relatively high background of the powder XRD patterns. One phase transition was seen at 450 K, which was shown by DSC not to be first order. Its thermal expansion properties were noted as being similar to those of ZrP_2O_7 and UP_2O_7. NMR data will be presented as part of this study in section 5.5.

4.4.2 ThP₂O₇

This material has been shown to exist at room temperature in two forms (α and β). The α-form has a cubic cell, with edge a = 8.721 Å.[71] This form undergoes a reversible phase transition to α' at 95°C. The β-form has an orthorhombic cell with cell parameters a = 11.612 Å, b = 12.750 Å, c = 7.121 Å.[71] It can thus be concluded from this that the β-form is not part of the AM₂O₇ family.

4.4.3 UP₂O₇

Again, this material was reported in a study by Vollenke et al., and was again suggested to exist in space group $Pa\overline{3}$, with a cell edge a = 25.88 Å.[8] The presence of a superstructure was confirmed by Hagman et al., who noted a subcell cell edge a = 8.2474 Å.[43] More recently a study by Cabeza et al. again found UP_2O_7 to exist with a space group $Pa\overline{3}$, with a cell edge a = 8.6311 Å.[72] Although no superstructure was seen in this last study, this is perhaps not surprising, as it is possible uranium will dominate the XRD powder pattern to such an extent that the supercell peaks (whose intensity is largely due to shifts of light oxygen atoms) would be

rather weak. It is noted that neutron data may be needed to see the superstructure in this case.[72]

4.4.4 NpP₂O₇

It would appear only one short study has been undertaken on this material.[73] The study stated that NpP_2O_7 exists with a cubic unit cell, with cell edge $a = 8.565$ Å.

4.4.5 PuP₂O₇

PuP_2O_7 has been found to have a cubic unit cell, with $a = 8.560$ Å, by Bjorklund.[74] It would appear no further work has been done on this material.

4.5 Mixed Cations [$M^{3+}_{0.5}$ $M'^{5+}_{0.5}$] (M = Sb, Bi, Nd, Eu; M' = Sb, Nb, Ta)

Table 4.1 below shows the mixed cation materials studied by Oyetola & co-workers, giving the structure type noted and the cell parameters.[75,76]

$M^{III}M^{IV}$	Structure Type	Cell Parameters
SbTa	cubic	a = 8.171 Å
BiSb	$Pna2_1$	a = 8.061 Å, b = 16.398 Å, c = 8.117 Å
BiNb	cubic	a = 8.236 Å
BiTa	$P2_1/c$	a = 8.276 Å, b = 16.376 Å, c = 8.417 Å
	cubic, $Pa\bar{3}$	a = 8.253 Å
NdTa	cubic	a = 8.269 Å
EuNb	pseudocubic	$a \approx$ 8.26 Å
EuTa	cubic	a = 8.297 Å

Table 4.1. A table showing the materials studied by Oyetola *et al.*, and the data they gave for the cell type and the related parameters.

The mixed cation AM$_2$O$_7$ materials presented in table 4.1 are of three basic structure types: α-SbP$_2$O$_7$ type (monoclinic, (Bi$_{0.5}$Ta$_{0.5}$)P$_2$O$_7$); β-SbP$_2$O$_7$ (orthorhombic, (Bi$_{0.5}$Sb$_{0.5}$)P$_2$O$_7$); cubic or pseudo-cubic. The results presented by Oyetola *et al.* are unclear apart from what is presented in table 1, and others have found these results difficult to reproduce.[77] The structures of α-SbP$_2$O$_7$ and β-SbP$_2$O$_7$ were reported by Verbaere *et al.* who described α-SbP$_2$O$_7$ as having a space group $P2_1/c$ with a = 8.088 Å, b = 16.0153 Å, c = 8.135 Å, β = 90.17°, Z = 4 and β-SbP$_2$O$_7$ as having a space group $Pna2_1$ with a = 8.018 Å, b = 16.134 Å, c = 8.029 Å, Z = 4. In both of these structures the Sb^{III} polyhedra are described as octahedra (though very distorted), so that the structures can be described as being built of SbO$_6$ octahedra corner sharing with P$_2$O$_7$ groups, with the structures being a 3D framework closely related to the literature structure of ZrP$_2$O$_7$.[44] In the β-SbP$_2$O$_7$ structure, if the Sb^{III}O$_6$ and Sb^{V}O$_6$ are assumed to be equivalent, the arrangement of the octahedra and P$_2$O$_7$ groups is nearly the same as that of ZrP$_2$O$_7$. The α-SbP$_2$O$_7$ structure is much more distorted, although the comparison to ZrP$_2$O$_7$ is still

possible.[75] In the β-structure only one type of connection is present between one octahedron and its nearest neighbours, whereas in the α-structure three types exist.[75] So the α-SbP$_2$O$_7$ structure is not simply a distortion of the β-SbP$_2$O$_7$ structure.

It appears that no other mixed oxide structures in this family have been reported to date.

4.6 Conclusion

The literature reviewed here shows the large number of the AM_2O_7 family studied to date, and also shows large gaps in knowledge regarding these materials. These materials are clearly interesting, as although all have related structures, the subtle differences bring with them changes in thermal expansion properties, a property which has been a strong driving force for much of the recent research in this field.

4.7 References

(1)   Korthuis, V.; Khosrovani, N.; Sleight, A. W.; Roberts, N.; Dupree, R.; Warren, W. W. *Chemistry of Materials* 1995, *7*, 412-417.

(2)   Sleight, A. W. *Curr. Opin. Solid State Mat. Sci.* 1998, *3*, 128-131.

(3)   Evans, J. S. O. *J. Chem. Soc. Dalton Trans.* **1999**, 3317-3326.

(4)   Losilla, E. R.; Cabeza, A.; Bruque, M. A.; Aranda, M. A. G.; Sanz, J.; Iglesias, J. E.; Alonso, J. A. *J. Solid State Chem.* 2001, *156*, 213-219.

(5)   Helluy, X.; Marichal, C.; Sebald, A. *J. Phys. Chem. B* 2000, *104*, 2836 - 2845.

(6)   Huang, C. H.; Knop, O.; Othen, D. A.; Woodhams, F. W. D.; Howie, R. A. *Can. J. Chem.* 1975, *53*, 79-91.

(7)   Levi, L. R.; Peyronel, G. *Z. Krist* 1935, *92*, 190 - 209.

(8)   Vollenke, H.; Wittmann, A.; Novotny, H. *Montash. Chemie* 1963, *94*, 956-963.

(9)   Evans, J. S. O.; Hanson, J. C.; Sleight, A. W. *Acta Crystallographica Section B-Structural Science* 1998, *54*, 705-713.

(10)   Tillmanns, E.; Gerbert, W.; Baur, W. H. *J. Solid State Chem.* 1973, *7*, 69-84.

(11)   Hartmann, P.; Jana, C.; Vogel, J.; Jäger, C. *Chem. Phys. Lett.* 1996, *258*, 107-112.

(12)   Iuliucci, R. J.; Meier, B. H. *J. Am. Chem. Soc.* 1998, *120*, 9059-9062.

(13)   Norberg, S. T.; Svensson, G.; Albertsson, J. *Acta Crystallographica Section C-Crystal Structure Communications* 2001, *57*, 225-227.

(14)   Sanz, J.; Iglesias, J. E.; Soria, J.; Losilla, E. R.; Aranda, M. A. G.; Bruque, S. *Chemistry of Materials* 1997, *9*, 996-1003.

(15)   King, I. J.; Fayon, F.; Massiot, D.; Harris, R. K.; Evans, J. S. O. *Chemical Communications* **2001**, 1766-1767.

(16)   Gover, R. K. B.; Withers, N. D.; Allen, S.; Withers, R. L.; Evans, J. S. O. *J. Solid State Chem.* 2002, *166*, 42-48.

(17)   Fleming, D. A.; Johnson, D. W.; Kowach, G. R.; J., L. P.US Patent 6258743, 2001.

(18)   Sleight, A. W. US Patent 5514360, 1995.

(19)   Evans, J. S. O.; Mary, T. A.; Sleight, A. W. *Physica B* 1997, *241*, 311-316.

(20)   Sleight, A. W.; Thundathil, A.; Evans, J. S. O. US Patent 5514360, 1996.

(21)   Brown, I. D.; Altermatt, D. *Acta Cryst.* 1985, *B41*, 244-247.

(22)   Brese, N. E.; O'Keefe, M. *Acta Cryst.* 1991, **B47**, 192-197.

(23)   Gruneisen, E. *Handb. Phys.* 1926, **10**, 1.

(24)   Elliot, S. *The Physics and Chemistry of Solids*; Wiley: Bath, 1998.

(25)   Röttger, K.; Endriss, A.; Ihringer, J.; Doyle, S.; Kuhs, W. F. *Acta. Cryst.* 1994, **B50**, 644-648.

(26)   Gignoux, D.; Givord, D.; Givord, F.; Lemaire, R. *J. Magn. Magn. Mater.* 1979, **10**, 288.

(27)   Megaw, H. D. *Crystal Structures a Working Approach*; Philadelphia:, 1973.

(28)   Dove, M. T. *Phase Transitions* 1997, **61**, 1.

(29)   Dove, M. T.; Gambhir, M.; Hammonds, K. D.; Heine, V.; Pryde, A. K. A. *Phase Transitions* 1996, **58**, 121.

(30)   Hammonds, K. D.; Dove, M. T.; Giddy, A. P.; Heine, V.; Winkler, B. *Am. Mineral.* 1996, **81**, 1057-1079.

(31)   Dove, M. T.; Heine, V.; Hammonds, K. D. *Miner. Mag.* 1995, **59**, 629-639.

(32)   Giddy, A. P.; Dove, M. T.; Pawley, G. S.; Heine, V. *Acta Cryst.* 1993, **A49**, 697-703.

(33)   Welche, P. R. L.; Heine, V.; Dove, M. T. *Phys. Chem. Miner.* 1998, **26**, 63-71.

(34)   Tautz, F. S.; Heine, V.; Dove, M. T.; Chen, X. *J. Phys. Chem. Miner.* 1991, **18**, 326.

(35)   Dove, M. T. *Am. Mineral.* 1997, **82**, 213-244.

(36)   Hammonds, K. D.; Heine, V.; Dove, M. T. *Phase Transitions* 1997, **61**, 155-.

(37)   Makart, H. *Helv. Chim. Acta.* 1967, **50**, 399-405.

(38)   Liebau, F.; Bissert, G.; Koppu, N. *Z. Anorg. Allg. Chem.* 1968, **359**, 113.

(39)   Poojary, D. M.; Borade, R. B.; Campbell III, F. L.; Clearfield, A. *J. Solid State Chem.* 1994, **112**, 106-112.

(40)   Bissert, G.; Liebau, F. *Acta Cryst., Section B* 1970, **26**, 233.

(41)   Baldus, M.; Meier, B. H. *J. Magn. Res.* 1996, **121**, 65 - 69.

(42)   Kaiser, U.; Glaum, R. *Z. Anorg. Allg. Chem.* 1994, **610**, 1755.

(43)   Hagman, L.; Kierkegaard, P. *Acta Chem. Scand.* 1969, **23**, 327-328.

(44)   Chaunac, M. *Bull. Soc. Chim. Fr.* **1971**, 424-429.

(45)   Tait, M. M., *4th year undergraduate thesis*, University of Durham, 2002.

(46)   Brindley, J. , *4th year undergraduate thesis*, University of Durham, 2001.

(47)   Soria, J.; Iglesias, J. E.; Sanz, J. *J. Chem. Soc. Faraday Trans.* 1993, **89**, 2515.

(48)   Larson, A. C.; Dreele, R. B. V. In;; Los Alamos Internal Report LA-UR-86-748, 1994.

(49)   McMurdie, H. F.; Morris, M. C.; Evans, E. H.; Paretzkin, B.; Wong-Ng, W.; Zhang, Y. *Powder Diffr.* 1987, *2*, 41.

(50)   Baldus, M.; Tomaselli, M.; Meier, B. H.; Ernst, R. R. *Chem. Phys. Lett.* 1994, *230*, 329 - 336.

(51)   Lee, Y. K.; Kurur, N. D.; Helmle, M.; Johannessen, O. G.; Nielsen, N. C.; Levitt, M. H. *Chem. Phys. Lett.* 1995, *242*, 304 - 309.

(52)   Dusold, S.; Kümmerlen, J.; Schaller, T.; Sebald, A.; Dollase, W. *J. Phys. Chem. B* 1997, *101*, 6359.

(53)   Withers, R. L.; Evans, J. S. O.; Hanson, J.; Sleight, A. W. *J. Solid State Chem.* 1998, *137*, 161-167.

(54)   Hodgkinson, P. H.; Evans, J. S. O.; Hampson, M. R., ZrV_2O_7 - ^{51}V variable temperature NMR studies.

(55)   Pascard, R.; Chaunac, M.; Grison, E. *Bull. Soc. Chim. Fr.* **1971**, 429-435.

(56)   Withers, R. L.; Tabira, Y.; Evans, J. S. O.; King, I. J.; Sleight, A. W. *J. Solid State Chem.* 2001, *157*, 186-192.

(57)   Khosrovani, N.; Korthuis, V.; Sleight, A. W.; Vogt, T. *Inorg. Chem.* 1996, *35*, 485-489.

(58)   Baran, E. J. *J. Less Common Met.* 1976, *46*, 343.

(59)   Turquat, C.; Muller, C.; Nigrelli, E.; Leroux, C.; Soubeyroux, J. L.; Nihoul, G. *European Physical Journal-Applied Physics* 2000, *10*, 15-27.

(60)   Fukuoka, H.; Imoto, H.; Saito, T. *J. Solid State Chem.* 1995, *119*, 98 - 106.

(61)   Gover, R. K. B. "NbP_2O_7 Experiment," ISIS Report, 2001.

(62)   Haider, S. Z. *Anal. Chim. Acta* 1961, *24*, 250-253.

(63)   Haider, S. Z. *Proc. Pak. Acad. Sci.* 1964, *1*, 19-28.

(64)   Levin, E. M.; Roth, R. S. *J. Solid State Chem.* 1970, *2*, 250-261.

(65)   Zah-Letho, J. J.; Verbaere, A.; Jouanneaux, A.; Taulelle, F.; Piffard, Y.; Tournoux, M. *J. Solid State Chem.* 1995, *116*, 335-342.

(66)   Leclaire, A.; Borel, M. M.; Grandin, A.; Raveau, B. *Eur. J. Solid State Inorg. Chem.* 1988, *25*, 323-328.

(67)   Haushalter, R. C.; Mundi, L. A. *Chem. Mater.* 1992, *4*, 31-48.

(68)   Lezama, L.; Rojo, J. M.; Mesa, J. L.; Rojo, T.; Olazcuaga, R. *J. Solid State Chem.* 1995, *115*, 146-151.

(69)   Teweldemedhin, Z. S.; Ramanujachary, K. V.; Greenblatt, M. *Mater. Res. Bull.* 1993, *28*, 427-433.

(70)   Banks, E.; Sacks, R. *Mater. Res. Bull.* 1982, *17*, 1053-1055.

(71)   Burdese, A.; Borlera, M. L. *Le Ricerca Scientifica* 1960, *30*, 1343-1345.

(72)   Cabeza, A.; Aranda, M. A. G.; Fernando, M. C.; Lozano, D.; Martínez- Lara, M.; Bruque, M. A. *J. Solid State Chem.* 1996, *121*, 181-189.

(73)   Nectoux, F.; Tabuteau, A. *Radiochem. Radioanal. Letters* 1981, *49*, 43-48.

(74)   Bjorklund, C. W. *J. Am. Chem. Soc.* 1958, *79*, 6347-6350.

(75)   Verbaere, A.; Oyetola, S.; Guyomard, D.; Piffard, Y. *J. Solid State Chem.* 1988, *75*, 217-224.

(76)   Oyetola, S.; Verbaere, A.; Guyomard, D.; Crosnier, M. P.; Piffard, Y.; Tournoux, M. *Eur. J. Solid State Inorg. Chem.* 1991, *28*, 22-36.

(77)   Gover, R. K. B., Personal Communication.

Chapter 5

AM$_2$O$_7$ Materials - Results and Discussions

5.0 General

Data were collected as part of this study for the ZrP_2O_7, HfP_2O_7, SnP_2O_7, PbP_2O_7, CeP_2O_7 and ZrV_2O_7 members of the AM_2O_7 family. A combination of X-ray, neutron and electron diffraction has been used with solid state $^{31}P/^{51}V$ NMR studies. Part of the motivation for this study was to gain a greater understanding of the structures of these materials, to gain more information on what causes some of these materials to exhibit NTE (e.g. ZrV_2O_7),[1] while others show low thermal expansion tending to zero (e.g. ZrP_2O_7)[2] and yet others give positive thermal expansion at all temperatures (e.g. SnP_2O_7).[3]

5.1 ZrP$_2$O$_7$

As stated above, ZrP_2O_7 is the most studied of this family of materials. It has been mainly examined by powder X-ray and neutron diffraction, with one study also combining this with solid-state NMR.[4-9] All of the studies, prior to this one, have shown ZrP_2O_7 to exist with a room temperature 3 x 3 x 3 superstructure and space group $Pa\bar{3}$. It has also worth noting that only one phase transition has been observed by X-ray diffraction for the material, at ~ 290°C. More details are given below in 5.1.2

For this study powder X-ray and neutron diffraction studies and electron diffraction have been combined with 1D and 2D solid-state NMR techniques. Diffraction was used to study the phase transition as well as the room temperature structure. Solid-state NMR has been used to study the room temperature superstructure only.

5.1.1 Diffraction Studies of the Phase Transition

From the literature it was believed that ZrP_2O_7 is isostructural with ZrV_2O_7, which has been shown to undergo two clear phase transitions upon heating. The first is from a room temperature 3 x 3 x 3 superstructure to an incommensurate superstructure phase, before a second phase transition to the ideal high temperature 'simple' cubic structure. In the case of ZrP_2O_7 only a single phase transition has been seen by either diffraction or DSC experiments (fig. 5.1).
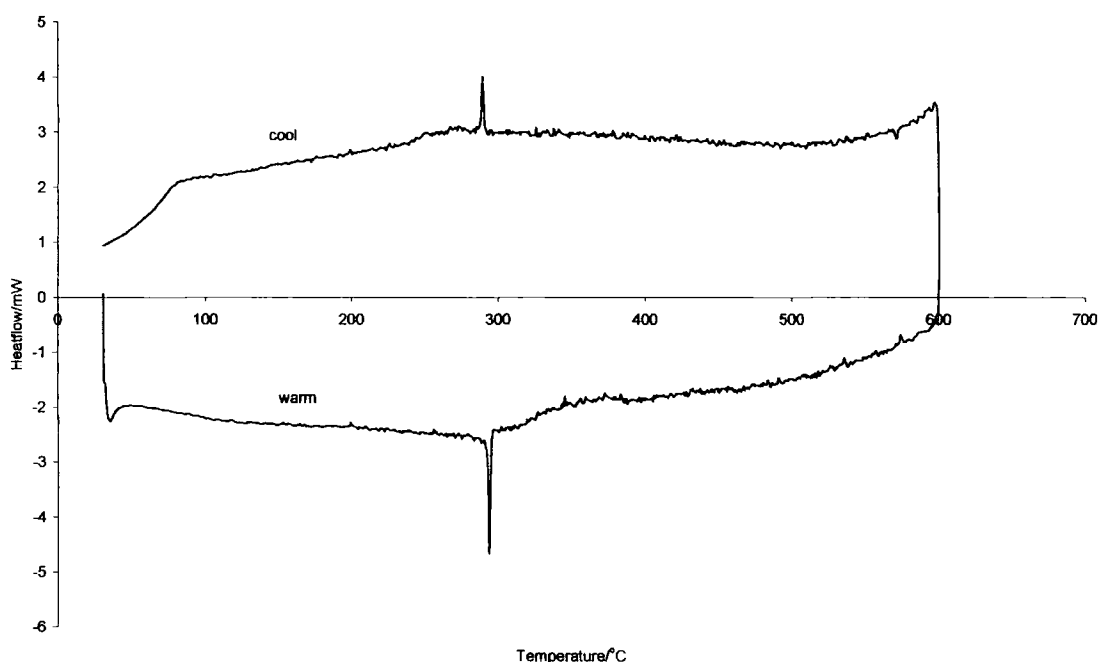
Figure 5.1. A DSC trace of ZrP_2O_7.

The apparent lack of this middle incommensurate phase was of interest, as if these structures were truly isostructural at both room temperature and high temperature, it could be expected that the same phase transitions may occur to get from the low temperature form to the high temperature form. With this in mind variable temperature powder X-ray and electron diffraction studies were undertaken (the later being carried out as part of this study by Prof. Ray L. Withers and his group in Canberra, Australia).

5.1.2 Powder X-ray Diffraction

Variable temperature (VT) X-ray diffraction experiments were carried out, with data collected between 10° and 60° 2θ, with two hour scans taken in 10K steps between 30 and 220°C and 5K steps between 225 and 280°C. The second region was done in 5K steps as it spans the phase transition. To help obtain accurate data sets, a one-hour scan was run directly before starting the VT experiment to ensure the monochromator was at operational temperature. A typical X-ray diffraction pattern obtained is shown in fig. 5.2. The data collected were analysed with the Topas program.[10] This program uses the space group (here assumed to be $Pa\bar{3}$) and approximate a-cell parameter (for cubic systems such as ZrP_2O_7) to calculate the positions of the reflections. This was done first for the subcell reflections only (starting with a cell parameter of 7.911Å). This was repeated for the superstructure starting with an a-cell edge of 23.733Å (i.e. three times that of the subcell). The fit was carried out using a Pawley approach, which involves fitting of intensities, within the constraint of the expected peak positions. In general the 2θ value observed for a reflection is dependent on not only the cell, but also the sample height in relation to the X-ray beam (this varies with temperature) and the 2θ zero point.

So,

$$2\theta_{obs} = \text{f (cell, zero point, height)} \qquad \text{(Equation 5.1)}$$

By first fitting the subcell (i.e. the strong reflections) it is possible to find accurate values for both the zero point and the height at each temperature. These can then be used as fixed values when fitting the superstructure, reducing the possibility of them correlating with other variables during the Pawley fit of the complex superstructure.
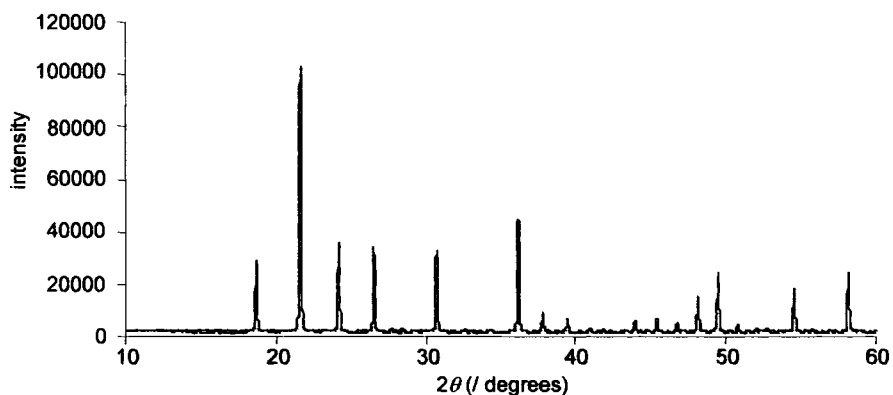
Figure 5.2. A room temperature X-ray diffraction powder pattern of ZrP₂O₇. The reflections due to the 3 x 3 x 3 superstructure are very small compared to those of the subcell, and only a few are visible here.

As can be seen from fig. 5.2, the subcell reflections are much stronger than those of the supercell. Only a few supercell reflections are visible, most not being seen on the scale shown, with most of the small reflections seen actually being due to the subcell. An expanded section is shown in fig. 5.3, showing that the supercell reflections are clearly visible but much weaker than the subcell reflections and only just above the noise.
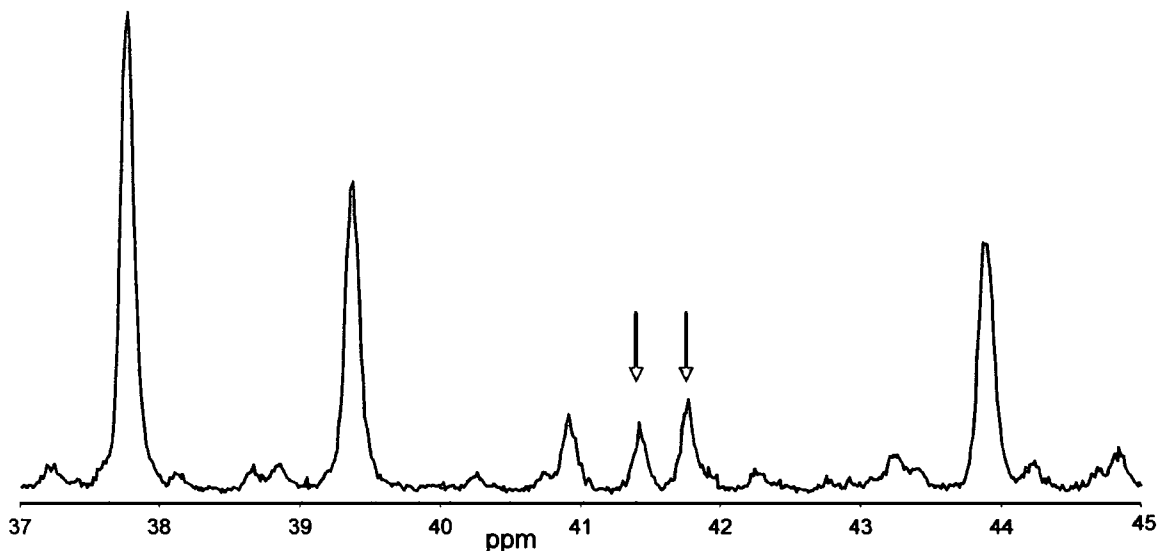
Figure 5.3. An expanded range of figure 5.2, highlighting the relatively low intensities of the supercell reflections. Two relatively strong supercell reflections are highlighted here by arrows (the reflection of similar intensity to the left of these is a weak subcell reflection).

The fitting of the superstructure was done over small sections of the XRD data sets, in which no subcell reflections exist, specifically [10.00-18.03, 26.88-30.12 and 32.69-34.00° 2θ], and a cubic cell was used. Nine parameters were refined, including six background terms, two peak shape terms and one cell parameter. If the supercell of ZrP₂O₇ does go incommensurate at any stage one would expect the 2θ values of the superstructure reflections to behave in a different

way to the subcell reflections. To investigate this possibility, the cell parameter of ZrP_2O_7 was

derived in two ways: from subcell only and supercell only reflection positions. The cell edges of

the subcell and the supercell were compared by simply multiplying the cell edge of the subcell

by three. A plot of cell edge, a, against temperature is shown in fig. 5.4. From this figure it does

not look as though ZrP_2O_7 undergoes the two phase transitions seen for ZrV_2O_7, but rather just

one phase transition, at 294°C. Both the supercell and subcell derived cells show thermal

expansion at the same rate, suggesting a commensurate phase. However, there is one slight

anomaly right at the phase transition, but it is thought this is not real, as the fits obtained for both

the supercell and subcell at this temperature are good (fig. 5.5). Another test for any

incommensurate behaviour was to look at the intensities of the weak supercell reflections as a

function of temperature. It could be expected that for an incommensurate phase the intensities

of the different reflections would show different behaviour with temperature. As can be seen

from fig. 5.6, the normalised plot of intensity with temperature for these reflections shows similar

behaviour for all of the reflections over the temperature range studied.
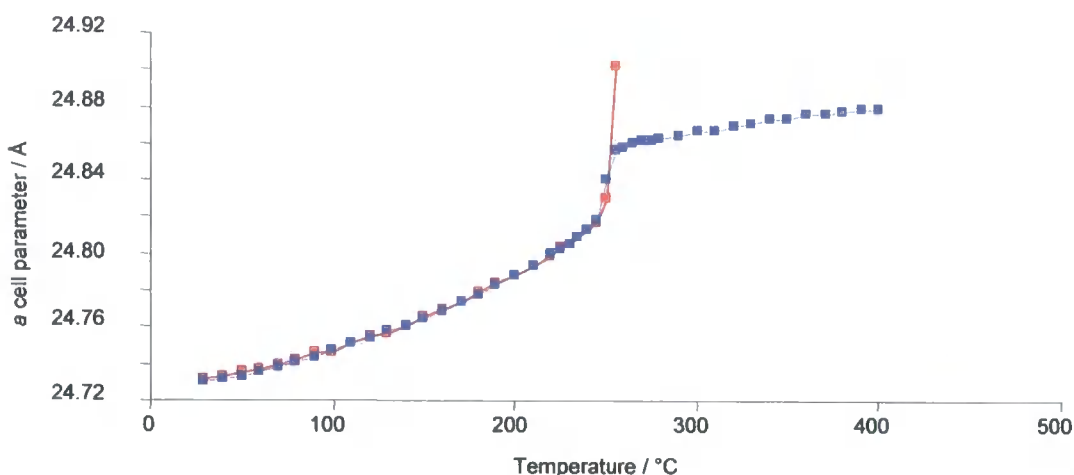
Figure 5.4. A graph of cell edge, a, against temperature. Cells derived from both subcell only and supercell only reflections are shown. Note that the cell edge values for the subcell are multiplied by three to allow comparison. The temperatures on this graph have not been fully calibrated.
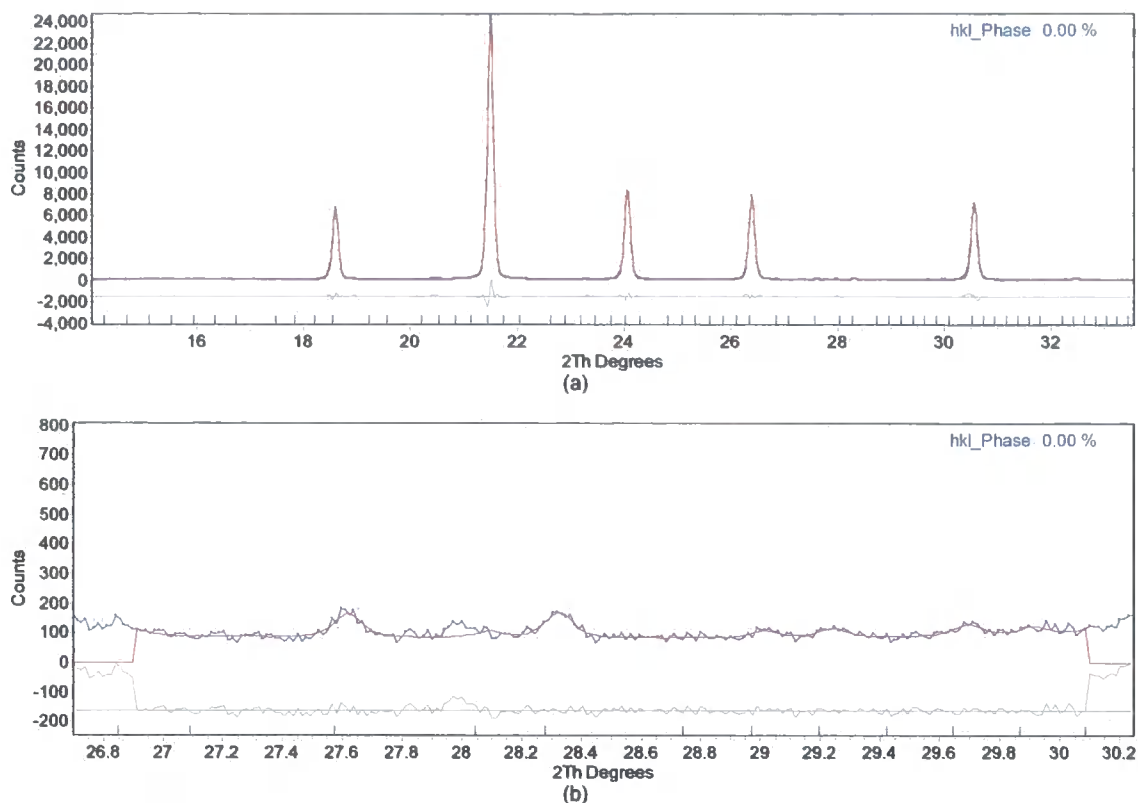
Figure 5.5. Pawley fits of ZrP_2O_7 powder XRD patterns, showing (a) the subcell fit (Rwp = 8.096, goodness of fit (GOF) = 1.760); and (b) a selected region of the supercell fit (Rwp = 12.255, GOF = 1.255).
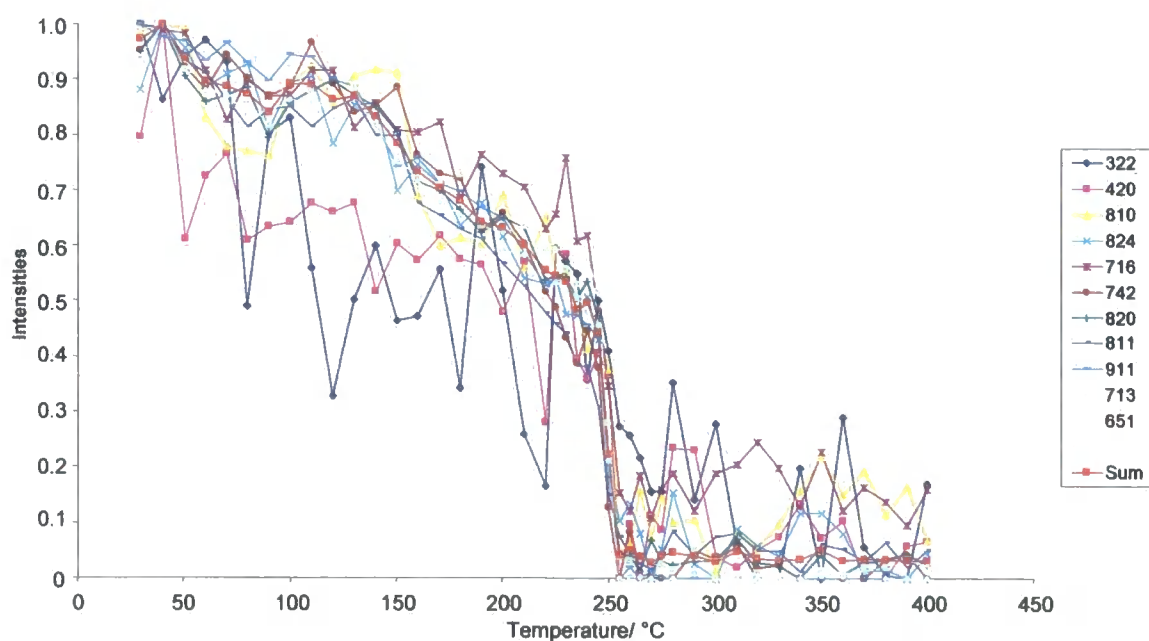
Figure 5.6. A normalised plot of the intensities of the supercell reflections as a function of temperature. NB. The reflection for 322 and 420 show a large scatter as they are very weak reflections, so uncertainties in their measurement are the cause of this scattering.

The conclusion from the X-ray diffraction data must be that there is no clear evidence of any incommensurate behaviour on warming ZrP_2O_7, and that only one phase transition is seen to occur.

5.1.3 Electron Diffraction

In an attempt to support this conclusion electron diffraction studies were undertaken. As has been shown earlier for ZrV_2O_7 (4.2.2), electron diffraction can be used to show the presence of superstructure, and of incommensurate phases. Fig. 5.7 shows three electron diffraction patterns obtained for ZrP_2O_7 at different temperatures. Unfortunately, as variable temperature electron diffraction experiments are performed on samples mounted on heated copper grids it can be experimentally very difficult to know the true sample temperature – the temperature of an individual grain will depend strongly on its proximity to a grid wire.

(a)

(b)

(c)
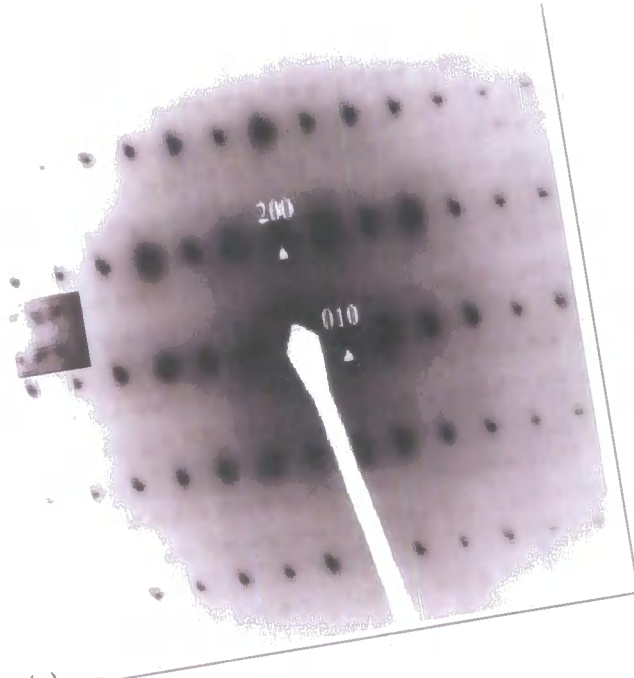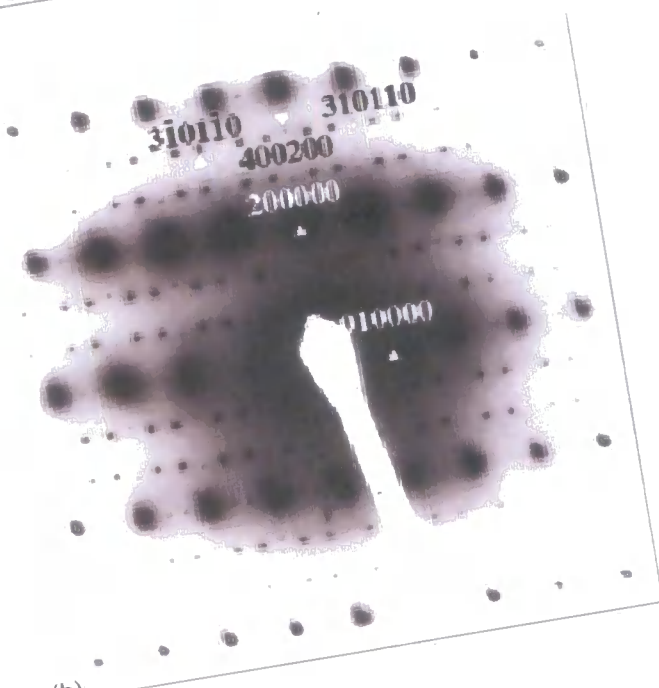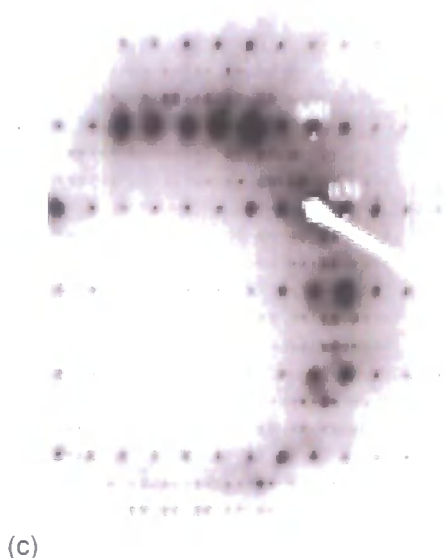
Figure 5.7.   Electron diffraction patterns of ZrP_2O_7 at different temperatures showing; (a) the unmodulated high temperature, parent, structure; (b) the incommensurate intermediate phase; and (c) the room temperature 3 x 3 x3 superstructure.

It can clearly be seen from fig. 5.7 that three different phases of ZrP_2O_7 do exist, rather than the two seen from the X-ray data, with the third phase being an incommensurate intermediate phase, i.e. like ZrV_2O_7 it appears that ZrP_2O_7 goes through an incommensurate phase on going from the room temperature 3 x 3 x 3 superstructure to the 'ideal' high temperature form. In the high temperature phase all superstructure reflections are absent. The electron diffraction of the room temperature phase shows the presence of Pa portion of $Pa\bar{3}$, although from fig. 5.8, this does not rule out the possibility of the $Pbca$ space group.

5.1.4 Solid-State NMR and Diffraction Studies of the 3 x 3 x 3 Superstructure

From the data presented above, there is clear evidence that ZrP_2O_7 exists at room temperature with a 3 x 3 x 3 superstructure, and that an a-glide plane is present within its structure. As already stated, this glide plane can only arise from two of the 12 possible superstructure space groups (fig. 5.8). Again, as already stated, due to the reflections from the supercell being weak it is possible to 'fit' a number of the 'allowed' space groups to the powder XRD pattern to obtain a satisfactory answer, and in this case, this is possible for both $Pa\bar{3}$ and $Pbca$, the two space groups that would give rise to an a-glide plane (although is should be noted that the $Pa\bar{3}$ space group gives a structure that requires two chemically implausible P–O bond-lengths [one long

and one short]). Because of this, it was necessary to employ another technique to gain more

information in an attempt to conclusively assign the correct space group, and hence be able to

use this information to solve the structure.
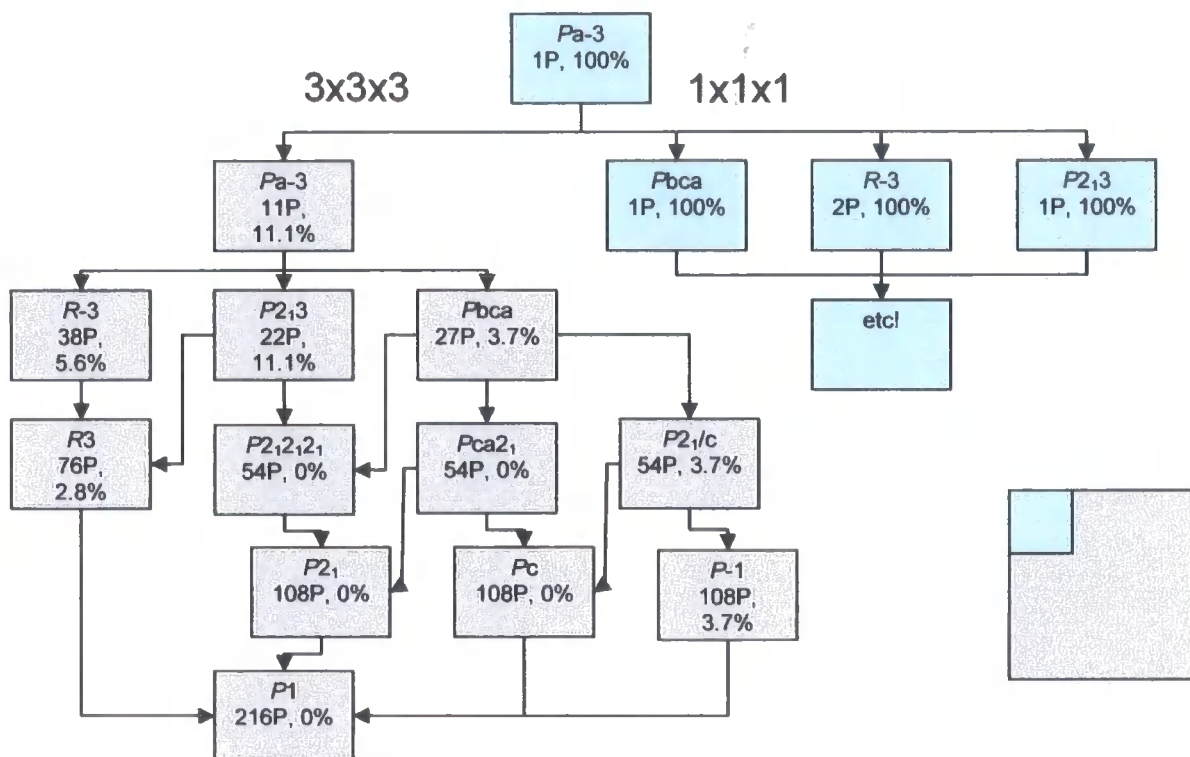
Figure 5.8. Table of allowed space groups for both the 1 x 1 x 1 subcell and the 3 x 3 x 3 supercell (as shown earlier in fig 4.5), showing the number of unique phosphorus sites in the asymmetric unit, and the percentage of these that lie on a site of special symmetry (i.e. in a $P_2O_7^{4-}$ unit with a 180° P–O–P bond angle).

All the information to date, both literature and the diffraction studies undertaken here, was

pointing towards the $Pa\bar{3}$ space group, although there was no conclusive evidence.

5.1.5 Why NMR?

One very powerful method to use is ^{31}P MAS NMR; four members of this family have previously

been studied via ^{31}P MAS NMR: SiP_2O_7 (11 ^{31}P sites), TiP_2O_7 (11 ^{31}P sites), GeP_2O_7 (more than

35 ^{31}P sites) and ZrP_2O_7 (11 ^{31}P sites).[9,11-14] ^{31}P NMR allows one to find the number of ^{31}P sites

in the asymmetric unit. As can be seen in fig. 5.8, different space groups give rise to different

numbers of ^{31}P sites within the asymmetric unit, and for the space groups $Pa\bar{3}$ and $Pbca$, 13

and 27 ^{31}P sites would be present respectively. For $Pa\bar{3}$, of the 11 phosphorus environments

present three ^{31}P sites would be seen with a relative intensity of one, with the other eight sites having a relative ratio of three, while for *Pbca*, all the sites would have the same intensity. For the four materials studied previously with this technique, two, GeP$_2$O$_7$ and ZrP$_2$O$_7$,[9,14] have been looked at with simple 1D MAS NMR, while work on the other two, SiP$_2$O$_7$ and TiP$_2$O$_7$,[11-13] utilised some elegant 2D MAS NMR experiments. These 2D MAS NMR experiments have included 2D exchange experiments,[11] 2D TOBSY experiments,[12,13] 2D zero-quantum transfer (ZQT) RIL experiments and single-quantum–double-quantum (SQ–DQ) correlation experiments (using the C7 pulse sequence for DQ excitation and reconversion). The first experiment utilises dipole-dipole interactions to probe through-space interactions. At short mixing times only short range interactions are seen, so that only ^{31}P–^{31}P interactions from the phosphorus atoms in the same P$_2$O$_7{}^{4-}$ group will be probed. The TOBSY experiment utilises through-bond J–J interactions, while suppressing dipolar interactions. These are short range interactions, so only ^{31}P–^{31}P interactions from the phosphorus atoms in the same P$_2$O$_7{}^{4-}$ group are seen. One other characteristic of this experiment is that no cross peaks will be seen for a P$_2$O$_7{}^{4-}$ group containing two crystallographically identical phosphorus atoms, i.e. such groups will give rise to a single resonance lying along the diagonal of a 2D spectrum (as is shown for TiP$_2$O$_7$ in fig. 4.10, section 4.2.1). The last two experiments, ZQT RIL and SQ–DQ correlation, both use dipolar interactions, and can be used to help assign peaks to specific phosphorus atoms. The ZQT RIL experiment can be repeated a number of times using a range of mixing times to see how cross peak intensities change with mixing time. This can be simulated for a number of different possible structural arrangements, and compared to experimental results to find a solution. The SQ–DQ correlations with short mixing times will give rise to cross peaks due to through-space intra-P$_2$O$_7{}^{4-}$ dipolar interactions, but with slightly longer mixing times, some slightly longer range dipolar interactions will be observed. In the case of TiP$_2$O$_7$ this was used to assign peaks to specific phosphorus atoms (first assuming it to be isostructural with the known structure of SiP$_2$O$_7$) by the simple method of looking at next nearest neighbours. The 11 phosphorus sites seen in this structure make this experiment difficult, pushing it to its limits, as the chemical shift range in these systems is small, because all the phosphorus atoms are in similar environments.

5.1.6 1D MAS NMR

As a starting point for this study, the ZrP_2O_7 MAS NMR work by Korthuis *et al.* is of obvious interest.[9] In this study a 1D MAS NMR spectrum was presented, recorded with a MAS speed of 18 kHz using a Chemagnetics CMX360. It looked very much like the spectrum recorded with a MAS frequency of 5 kHz as shown in fig. 5.9. The study concluded that 11 ^{31}P sites were present, and the peak at ~ -45 ppm was due to an impurity, although no real explanation appeared to support this. With chemical shielding anisotropy usually having a large affect on ^{31}P MAS NMR spectra it would seem to make sense for spectra to be recorded at high spinning speeds. However, this can involve losing information as some interactions are averaged out. In addition for both SiP_2O_7 and TiP_2O_7 some peaks have been seen to move with different spinning rates, with one peak having been seen to split in the case of TiP_2O_7.[13] These effects were both explained as being due to dipolar interaction effects at different spinning speeds, and will be discussed further below.[13] Armed with all of this knowledge, 1D ^{31}P MAS NMR spectra were recorded at three different spinning rates, 3, 5 and 14 kHz, with a Bruker DSX 300 using a standard probe, and are shown in fig. 5.9.
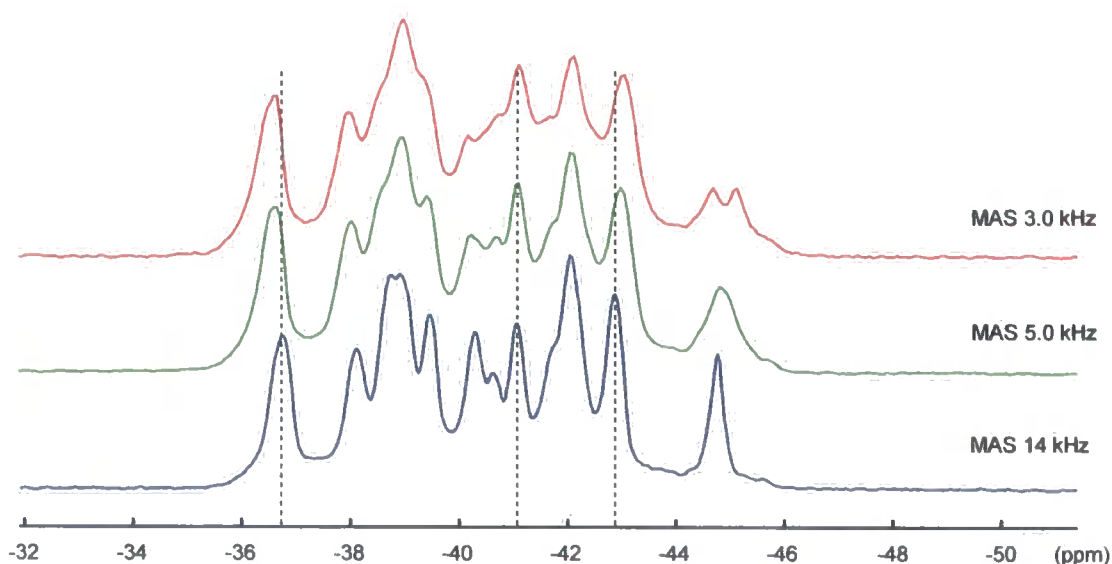
Figure 5.9. 1D ^{31}P MAS NMR spectra of ZrP_2O_7 at different spinning rates. Vertical lines have been added to highlight the different behaviour of different peaks at different spinning speeds.

The spectra obtained at 5 and 14 kHz are very similar to that presented by Korthuis *et al.*[9] The first important conclusion is that the peak they assigned as an impurity is also present in the

spectra obtained here. This would mean that either the sample studied here contained the same impurity with the same relative intensity, or that this peak is not due to an impurity, but is intrinsic to ZrP_2O_7. Upon lowering the spinning speed it is seen that some peaks move in the spectrum, and the peak at ~ -45 ppm is seen to split into two. As mentioned earlier, these effects have been seen for TiP_2O_7, and occur as MAS does not readily average out homonuclear dipolar coupling interactions fully in extended homonuclear dipolar coupled spin systems, such as exists for the AM_2O_7 materials.[13, 15,16]

It is clear 'movement' of peaks is seen for the resonances previously assigned to the pure phase and the resonance previously assigned as an impurity. It is likely that all these peaks actually arise from the same phase (although the effect is larger for the latter resonance). If this is true then it is apparent that these spectra imply more than the 11 phosphorus sites expected for space group $Pa\bar{3}$ (at least 13 resolved peaks are visible). However, these 1D spectra were not enough to be able to draw a reliable conclusion. Therefore a 2D RFDR[17] experiment was undertaken.

5.1.7 2D RFDR Experiments

An RFDR experiment allows the probing of dipolar coupling (through space interactions), but only from atoms within the same phase, so any impurity will show no cross-peaks with the pure phase in the 2D spectra. As for other 2D exchange experiments, short mixing times give spectra showing only short range interactions, while long mixing times show longer range interactions, so a number of experiments are often carried out with varying mixing times. Here two experiments were carried out, one with a mixing time of 12 ms and a second with a mixing time of 40 ms. The spectra are shown in fig. 5.10. The diagonal of these 2D RFDR spectra (like the diagonal in other 2D spectra) is the 1D MAS spectrum, while the off-diagonal peaks arise when dipolar interactions occur between different sites, in this case different ^{31}P sites. The ^{31}P sites within the 1D MAS spectrum between which these interactions occur can be seen simply by drawing a horizontal and vertical line to the diagonal, and as such you therefore always see symmetry within the spectra (although usually not exact symmetry due to experimental effects). Fig. 5.10(a) shows short range interactions within the ZrP_2O_7 structure,

but gives very little, if any, useful information. However, fig. 5.10(b) is a spectrum showing longer range interactions. It is quite clear in the spectrum that interactions occur between all the individual resonances, including the peak at approximately -45ppm, showing that only one [phosphorus containing] phase is present. One thing worth highlighting is that the use of different mixing times clearly shows how different information may be obtained.

Using the information from the 2D RFDR experiment in conjunction with the 1D MAS spectra (fig. 5.9) we can conclusively show that the structure of ZrP$_2$O$_7$ contains more than 11 ^{31}P sites. However, it is not possible with the information so far presented to be able to say any more than this. This shows that the ZrP$_2$O$_7$ is not isostructural with the published structure of ZrV$_2$O$_7$.[18]
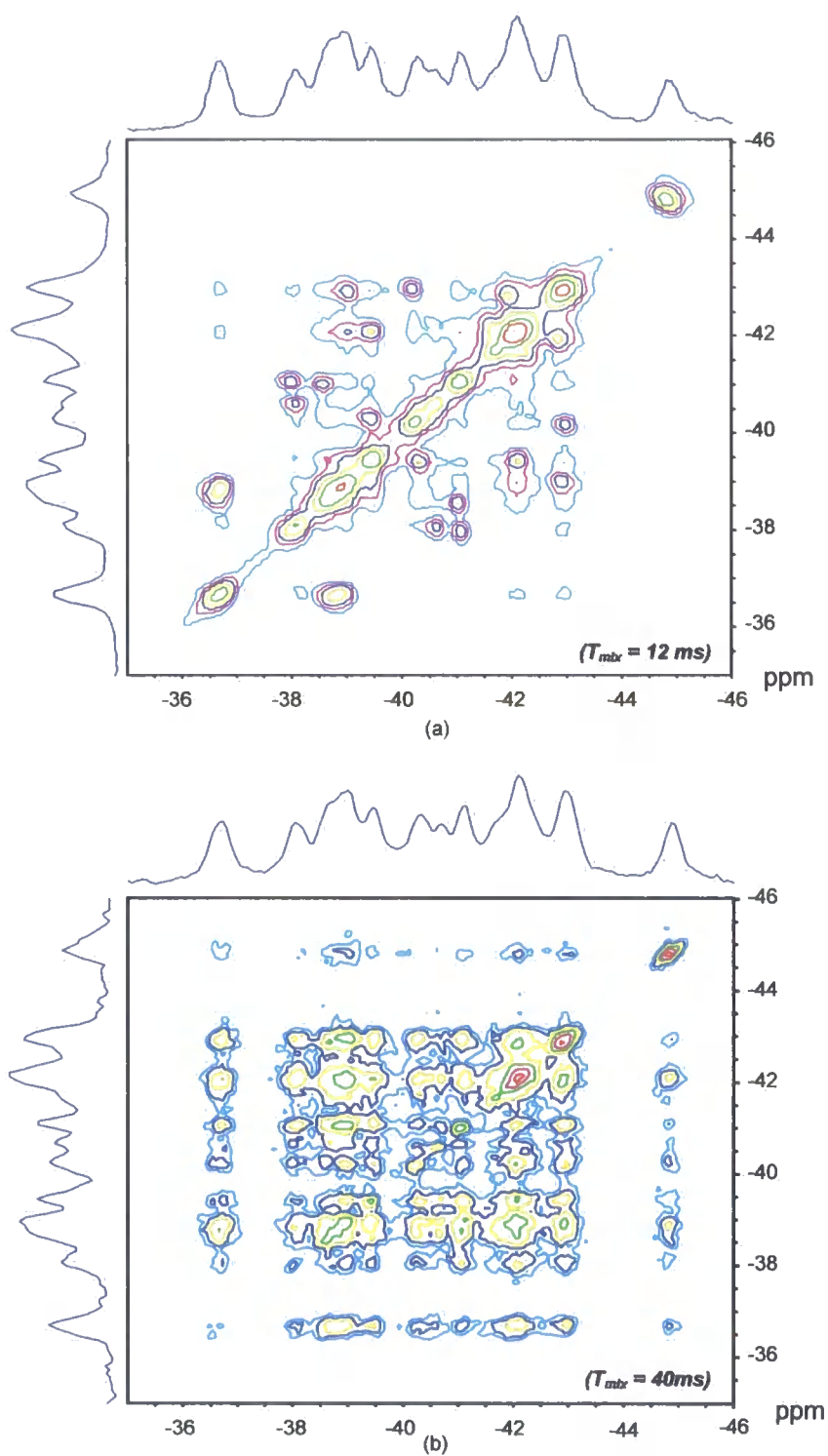
Figure 5.10. 2D RFDR spectra of ZrP_2O_7 recorded using a MAS frequency of 10 kHz at (a) short mixing time, showing short range interactions and (b) longer mixing time, showing longer range interactions. As can be seen in (b) cross-peaks appear between all the individual resonances in the spectrum showing that all the ^{31}P resonances are from a single crystalline phase.

5.1.8 2D MAS Double-Quantum Through-Space Experiments

2D double-quantum (DQ) NMR experiments, like RFDR experiments, 'look' at through-space dipole-dipole interactions between different nuclei within a structure. However, two important differences are present between these two experiments: (a) only relatively short range interactions are seen in 2D DQ experiments; (b) the 1D MAS spectrum is not seen along the diagonal on a 2D DQ spectrum, allowing much better resolution. This latter point is due to the fact that 2D DQ experiments use double quantum coherence (here achieved through use of the POST-C7 sequence[19]) which requires pairs of spins. In practice this means that the spectra presented here are a correlation of the 1D MAS spectrum for individual spins (e.g. PO_4 tetrahedra), i.e. the 'normal' MAS, with the 1D MAS for pairs of spins (e.g. $P_2O_7^{4-}$ groups). This then gives information on the number of $P_2O_7^{4-}$ units in the structure, and hence the number of unique phosphorus sites. Here it is important to note that peaks can still appear along the diagonal of the spectra, but only when they arise from autocorrelations.

Experiments were done under a MAS speed of 10 kHz using a Bruker DSX 300. A spectrum is shown in fig. 5.11 below. It is quickly clear from this spectrum that at least 10 pairs of phosphorus atoms are present plus either one or two autocorrelations. However, on closer inspection it can be seen that only one true autocorrelation peak exists, and the peak in the top right of the spectrum is due to the two resonances that are seen to split at lower spinning speed in the 1D MAS (fig. 5.9). This gives us at least 23 phosphorus sites. Further information was gained by obtaining a fit of this spectrum using the dmfit2001 program,[20] and the fit is shown in fig. 5.12. The fit indicates that the two peaks in the bottom left of the spectrum were of triple intensity, i.e. they represented 3 phosphorus pairs rather than one, while all of the others were shown to be of single intensity (with respect to one another). Therefore, in total, this spectrum shows the presence of 13 $P_2O_7^{4-}$ groups with two inequivalent phosphorus atoms, and one $P_2O_7^{4-}$ group with two equivalent phosphorus atoms. The oxygen in this last group lies on a centre of inversion so that the two phosphorus atoms are in different asymmetric units. So, 27 phosphorus atoms are present within the asymmetric unit, all in a 1:1 ratio, showing (by referring back to fig. 5.8) that the true space group is $Pbca$, and not $Pa\bar{3}$.
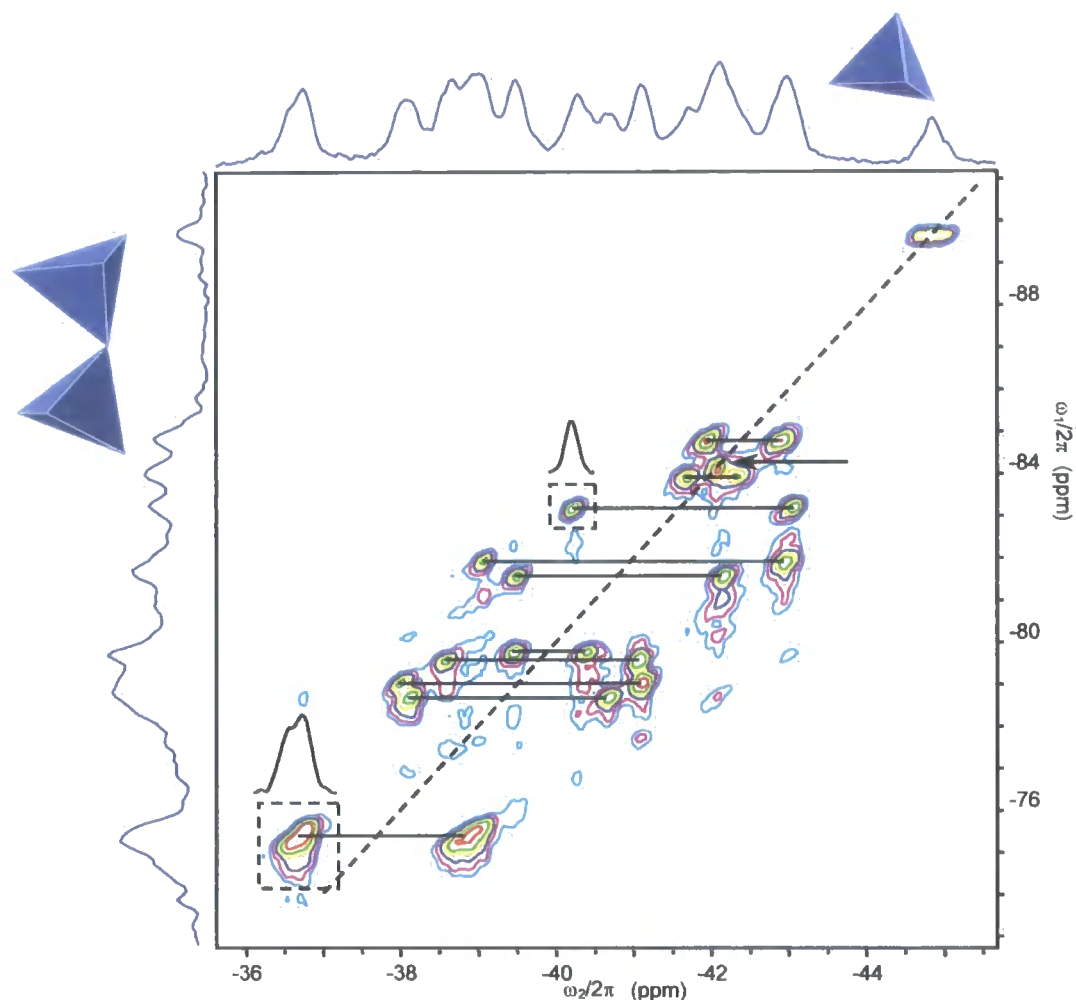
Figure 5.11. 2D ^{31}P double quantum dipolar MAS spectrum of ZrP_2O_7, using the POST-C7 sequence for double quantum excitation and reconversion, obtained with a MAS speed of 10 kHz. Horizontal lines highlight phosphorus pairs, and the arrow indicates an autocorrelation. More information is given in the text.

The information from this experiment was then used to fit the 1D MAS spectrum at 10 kHz (i.e. the same spinning speed as for the 2D DQ experiment). The peak positions were fixed, but line-widths were allowed to refine, and as can be seen in fig. 5.13, the peak positions allowed a good fit to the experimental 1D MAS spectrum.

This is only the second of these materials that have conclusively been shown not to exist in space group $Pa\bar{3}$, the other being GeP_2O_7.[14]
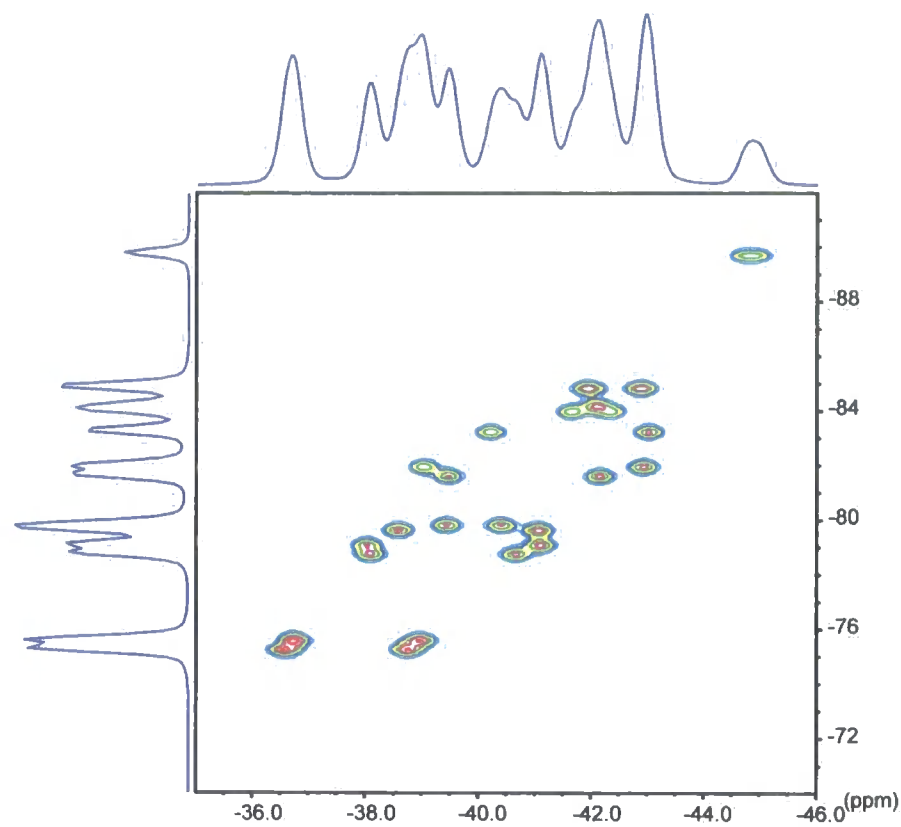
Figure 5.12. A fit of the 2D double quantum spectrum shown in fig. 5.11, done using the dmfit2001 program.[20]
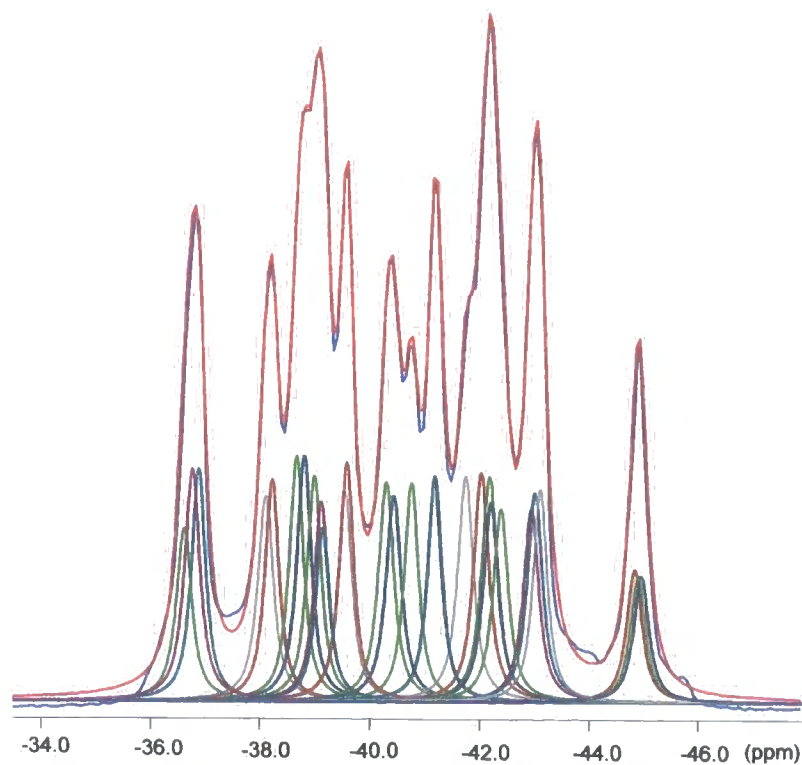
Figure 5.13. 1D ^{31}P MAS NMR spectrum of ZrP_2O_7 at 10 kHz fitted with 27 peaks, whose peak positions were taken from the fit of the 2D POST-C7 spectrum shown in figure 5.11.

5.1.9 2D MAS Double-Quantum Through-Bond Experiments

However, although this has shown that 27 unique phosphorus sites are present in the asymmetric unit, the information was still obtained by using through-space interactions, and to be totally conclusive it must be shown that the same number of phosphorus pairs are seen using through-bond interactions. This can be done by utilising *J*-couplings. An experiment was therefore carried out using the POST-C9 pulse sequence,[21,22] with a MAS speed of 8 kHz. The spectrum is shown below in fig. 5.14, and it is clear that the same off-diagonal peaks are present here that are present in the 2D DQ experiment, supporting the statement above that 13 $P_2O_7{}^{4-}$ groups exist which contain two inequivalent phosphorus sites. In this spectrum the 1D MAS appears along the diagonal, so that the cross-peak is obscured.
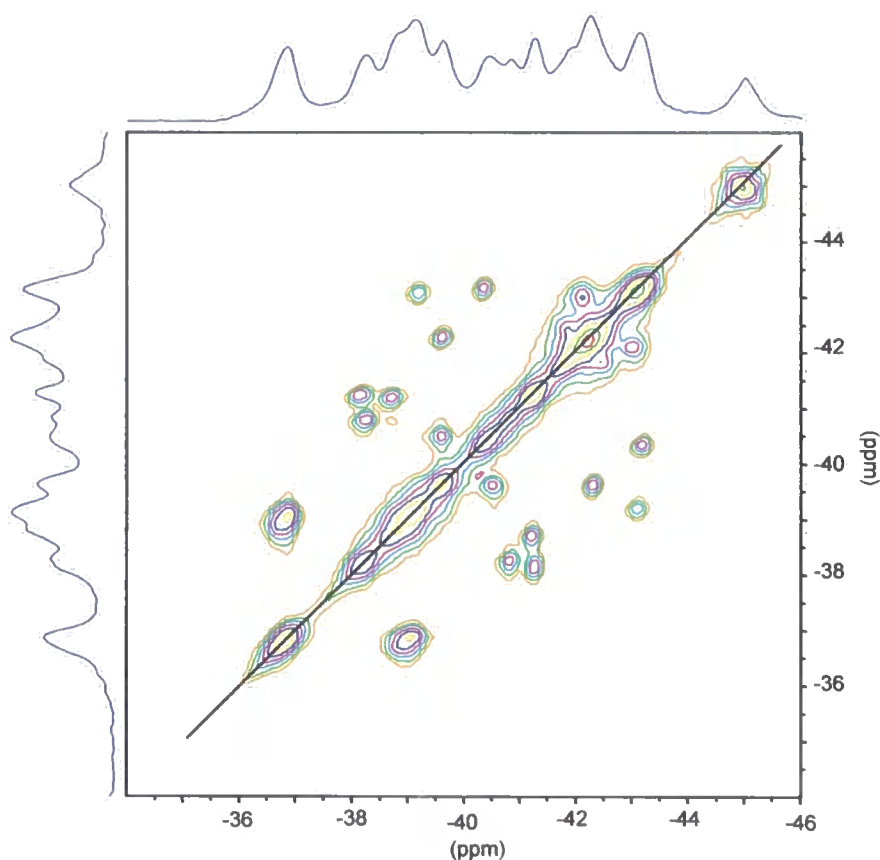
Figure 5.14. The 2D POST-C9 spectrum of ZrP_2O_7 with a mixing time of 15 ms. The spectrum shows through-bond interactions in the structure.

Armed with all the information from the three 2D experiments it is possible to state that the correct space group for ZrP_2O_7 is *Pbca*. Using this information it is then possible to return to the diffraction data to attempt a structure solution of this material.

5.1.10 Structure Solution of ZrP_2O_7 from Powder XRD

A structure solution of ZrP_2O_7 was carried out from powder XRD and neutron data by Dr. John Evans, as part of this study. For this structure solution two distinct methods were undertaken and both of these used combined treatment of synchrotron X-ray and high resolution powder neutron diffraction data. The two methods used gave equivalent answers, with an average atomic shift of only 0.02 Å between the two models.

The first method was a combination of distance least-squares modelling and Rietveld refinement. With this method, all atoms are initially set to ideal high-temperature coordinates and random atomic displacements are then applied. All the atomic coordinates are then refined so that the Zr–O distances, P–O distances, O–Zr–O bond angles and O–P–O bond angles converge to values that are reasonable when compared to other known structures. In this case the process was repeated several hundred thousand times and the best 277 structures created were selected. The term 'best' was based on the closeness of the bond distances to the criteria set. Combined X-ray/neutron refinement was then performed on these 277 structures with bond lengths and angles restrained to chemically sensible values. The best of these solutions was selected and more extensive Rietveld refinement was undertaken.

The second method defined the 13 P_2O_7 groups, which were not constrained to containing a 180° P–O–P bond angle, as semi-rigid bodies allowed to bend around the P–O–P bond and with an O–P–O–P–O torsion angle allowed to deviate from its ideal value of 60°. A simulated annealing program was then used which initially had the 13 P_2O_7 groups at ideal coordinates, and a full Rietveld refinement of partial neutron and X-ray data sets performed. At convergence, the groups and their internal degrees of freedom were moved by a random amount and the model re-refined. This was repeated many thousands of times and the model which gave the best fit to the experimental data was selected.

Both of these solutions were then subjected to identical Rietveld refinement protocols and X-ray data were refined from 2° to 57.7° 2θ, with the neutron data being refined from 40 to 113000 msecs. The final agreement factor achieved was, wRp = 6.16 %, with X-ray data giving values of wRp = 8.01 % and R_{Bragg} = 1.57 %, and neutron data giving values of wRp = 3.42 % and R_{Bragg} = 1.28 %. An example of the fit obtained is given in fig. 5.15, which shows the fit of neutron data, with the difference between the model and the experimental data shown.
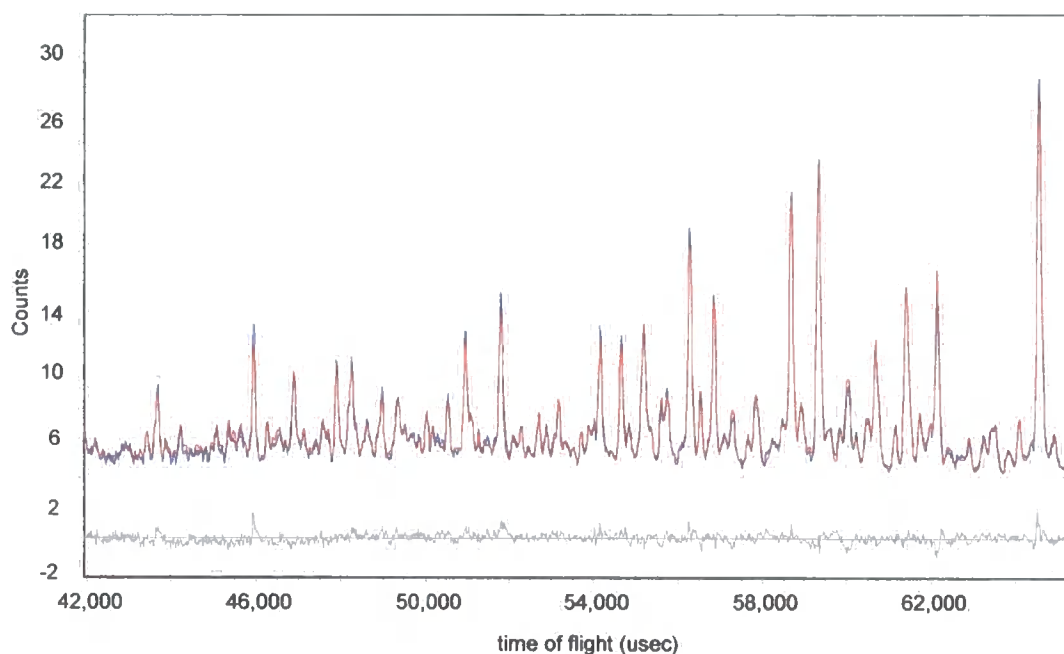
Figure 5.15. Neutron data of ZrP$_2$O$_7$ (blue) fitted with the structural model (red) described in the text, with the difference between these shown (grey).

This model gives the room temperature ZrP$_2$O$_7$ superstructure shown below (fig. 5.16). The full input file used to refine this structure, along with all the atomic coordinates and relevant information, is given in Appendix 4.
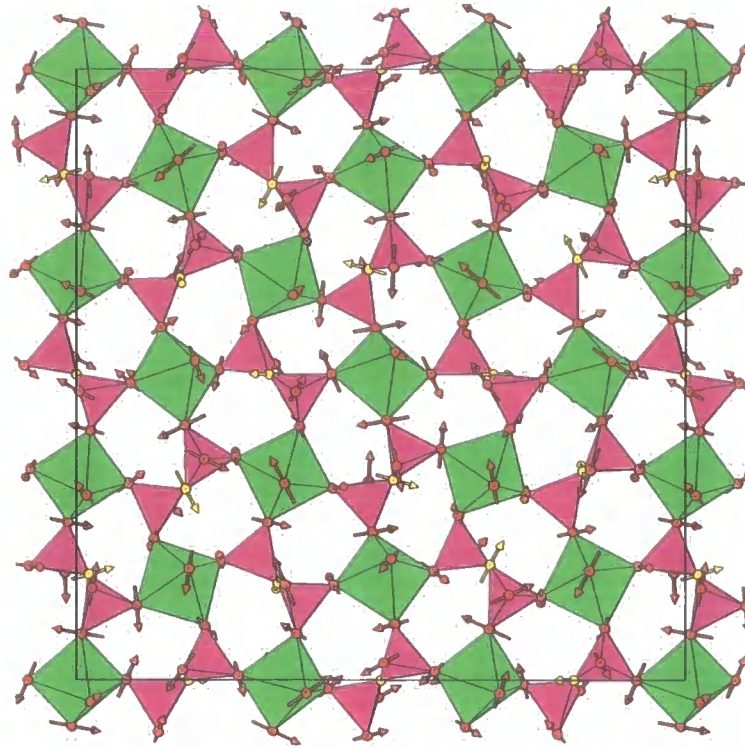
Figure 5.16. Picture of the refined superstructure of ZrP_2O_7, containing PO_4 corner-sharing tetrahedra, and ZrO_6 octahedra. The arrows on each oxygen show the magnitude and direction in which each has tilted from its ideal high symmetry position (the length of the arrow is proportional to twice the shift in Å).

5.2 HfP₂O₇

5.2.1 1D MAS NMR

1D MAS NMR spectra were recorded for HfP$_2$O$_7$ at 3 kHz and 6 kHz as shown in fig. 5.17. The spectra for HfP$_2$O$_7$ do not appear to be as resolved as those of ZrP$_2$O$_7$ (fig. 5.9), with only seven or eight (including shoulders on peaks) unique phosphorus sites being resolved in these spectra. However, as is clear from chapter 4, and can be seen in fig. 5.8, a number of space groups are possible for these materials, and so fewer peaks may be apparently resolved (compared to ZrP$_2$O$_7$) as there may be fewer phosphorus sites in this structure. So, with the information available in these spectra it is not possible to discount any of those space groups, i.e. no real information about the structure can be taken from these spectra. However, it is perhaps of interest to note that the general shapes of these 1D MAS spectra are similar to those obtained for ZrP$_2$O$_7$, as well as the chemical shifts being over a range of ~ 9 ppm, although the ^{31}P shifts of HfP$_2$O$_7$ are at lower ppm values, suggesting a similar structure with some subtle differences in the phosphorus environments.
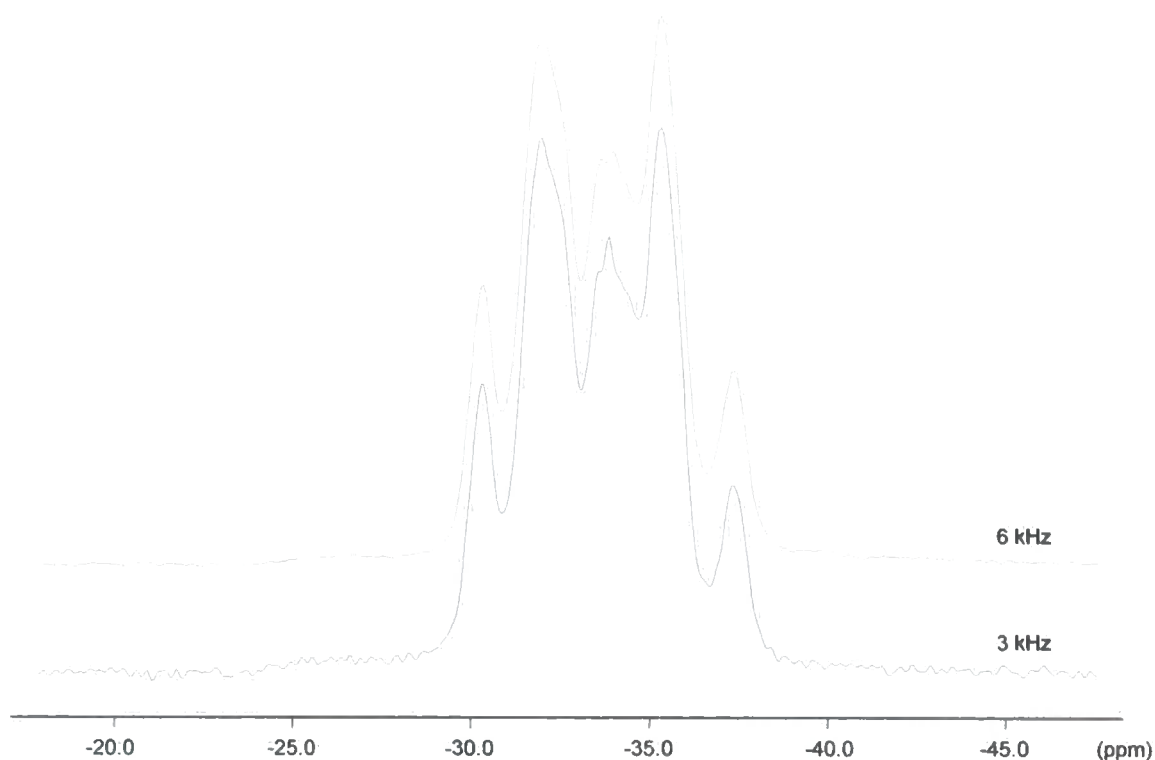
Figure 5.17. 1D ^{31}P MAS NMR spectra of HfP$_2$O$_7$ at 3 kHz and 6 kHz.

112

In an attempt to gain more information 2D NMR experiments were carried out.

5.2.2 2D MAS Double-Quantum Through-Space Experiments

A 2D MAS POST-C7 ^{31}P NMR spectrum of HfP_2O_7 was recorded at 10 kHz on a Bruker 300 DSX spectrometer, and is shown in fig. 5.18.
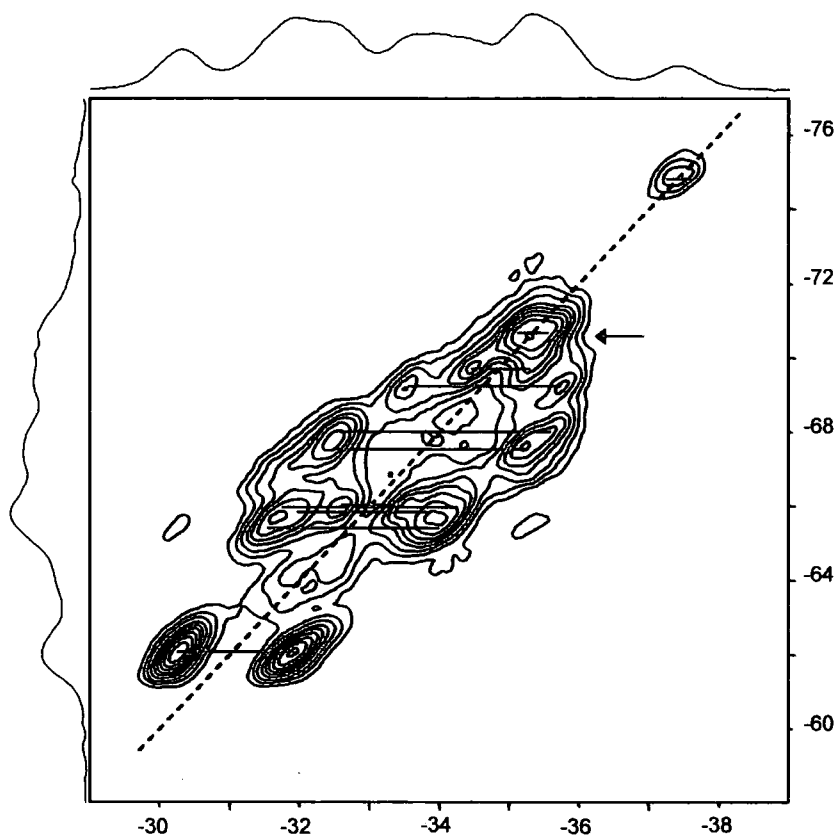
Figure 5.18. 2D ^{31}P POST-C7 spectrum of HfP_2O_7, under MAS conditions (10 kHz). The pairs of correlated peaks are shown by horizontal blue lines., with the pair in the bottom left corner being of triple intensity. The arrow shows the position of the autocorrelation peak.

As in the case of ZrP_2O_7 (section 5.1.8) this spectrum shows the presence of 27 unique phosphorus environments, with 13 correlated pairs, and one autocorrelation, implying that this material also has a space group *Pbca*. This supports the general observations regarding the 1D spectrum, and it is likely that the change in chemical shift with respect to ZrP_2O_7 is due to the change in the metal present in the structure.

5.2.3 2D MAS Double-Quantum Through-Bond Experiments

A 2D refocused-INADEQUATE experiment was also carried out to support the findings of the through-space POST-C7 experiment. The spectrum obtained is shown in fig. 5.19 below.
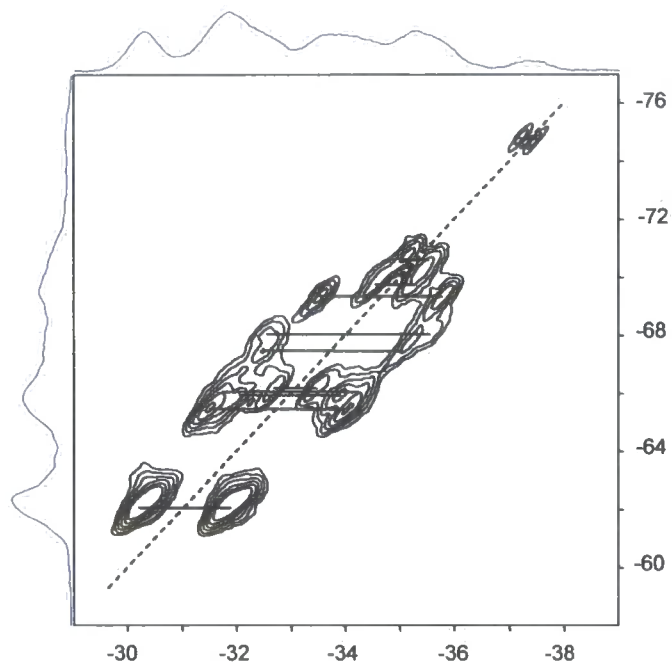
Figure 5.19. 2D ^{31}P refocused-INADEQUATE experiment, under MAS conditions, with spinning frequency 10 kHz. As in the POST-C7 spectrum (fig. 5.18) 27 unique phosphorus sites are seen.

HfP_2O_7 has therefore been shown, via ^{31}P NMR, to exist with the space group $Pbca$, as in the case of ZrP_2O_7, and so is another material in the AM_2O_7 family not to have a space group $Pa\overline{3}$. Assuming pure, highly crystalline HfP_2O_7 can be synthesized, it should be possible to solve the room temperature structure of this material, as has been the case for ZrP_2O_7.

5.3 SnP₂O₇

5.3.1 Powder X-ray, Neutron and Electron Diffraction

The powder X-ray, neutron and electron diffraction studies carried out as part of these studies were undertaken by Dr R. K. B. Gover et al.[3] As noted earlier (4.1.3), SnP_2O_7 is seen to exist with an apparently pseudo-cubic 3 x 3 x 3 superstructure at room temperature and to undergo two phase transitions upon heating, firstly to an incommensurate (by electron diffraction) superstructure phase and secondly to a superstructure which gives subcell reflections displaying rhombohedral distortions. It should be noted that electron diffraction also showed the presence of a 2_1 symmetry axis in the room temperature superstructure. This work was the starting point to the NMR work presented here, with the same sample being used, which was kindly prepared by Dr. R. K. B. Gover.

5.3.2 1D MAS NMR

As in the cases of ZrP_2O_7 and HfP_2O_7 1D ^{31}P MAS spectra of SnP_2O_7 were recorded at a variety of different MAS frequencies, and are shown below in fig. 5.20.

MAS 3.0 kHz

MAS 5.0 kHz

MAS 14 kHz

-26   -28   -30   -32   -34   -36   -38   -40   -42   -44   -46   -48   -50   (ppm)
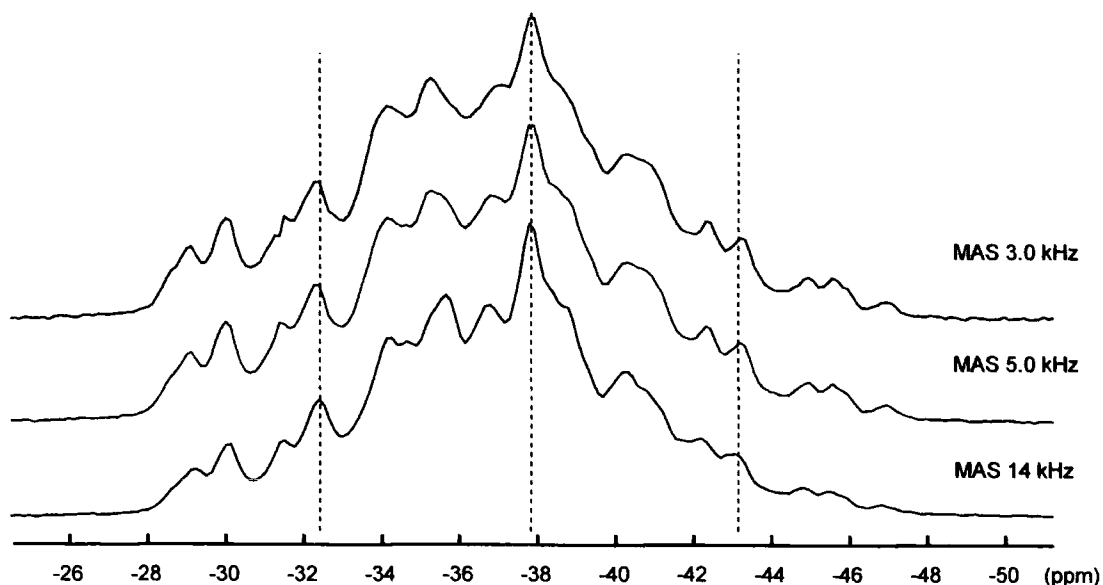
Figure 5.20. 1D ^{31}P MAS spectra of SnP_2O_7 at different MAS frequencies, as shown. The vertical dashed lines highlight the lack of 'movement' of the positions of any of the peaks when the spinning speed is changed.

It is instantly clear that the structure of SnP$_2$O$_7$ would appear to be much more complicated than that of ZrP$_2$O$_7$, with more than 16 unique phosphorus peaks in the 1D MAS at 3 kHz. Unlike the cases of ZrP$_2$O$_7$ and TiP$_2$O$_7$[13] there is no apparent movement of any of the resonances with MAS rate. It is thought no literature exists with regard to NMR experiments involving SnP$_2$O$_7$, so it is not possible to compare this to any other data set. As in the case of ZrP$_2$O$_7$ the next step was to proceed to 2D NMR experiments to attempt to gain more information and get a better understanding of the structure.

5.3.3 2D RFDR Experiment

Again, as in the case of ZrP$_2$O$_7$, an RFDR experiment was performed to check the sample was all of the same phase. The 2D RFDR spectrum is shown in fig. 5.21.
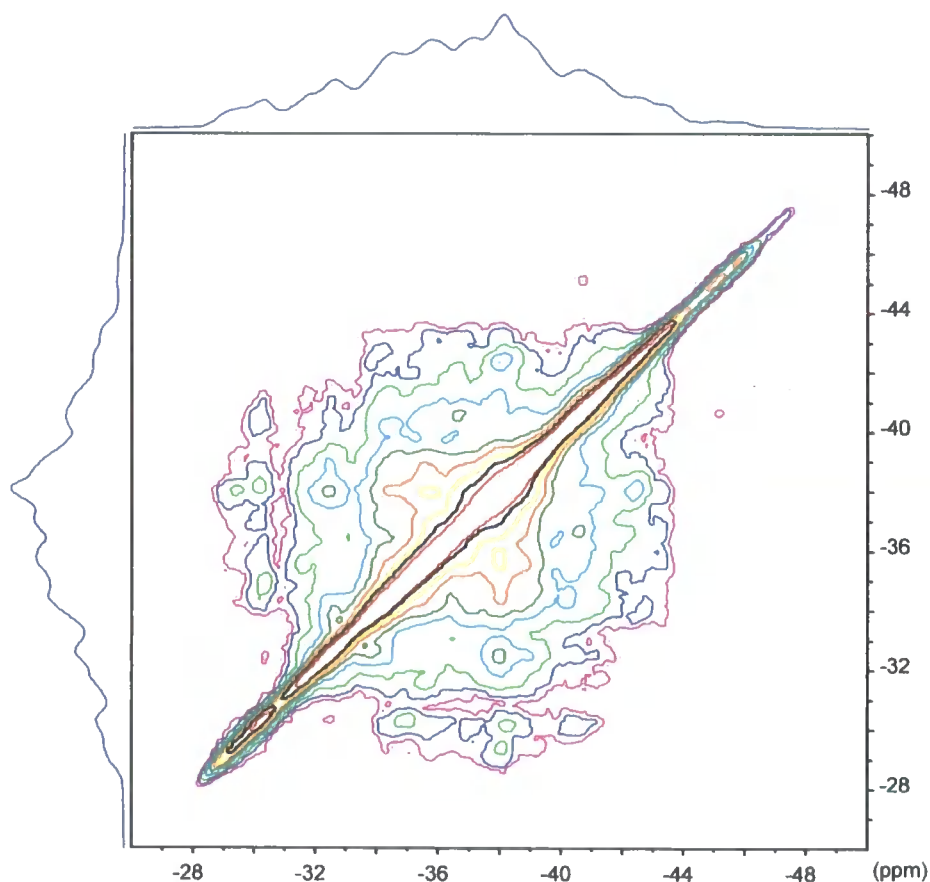
Figure 5.21. 2D RFDR spectrum of SnP$_2$O$_7$ recorded with a mixing time of 7.5 ms. No cross peaks are seen in relation to the top right of the spectrum. It is thought this is due to offset problems in the experiment.

As can be seen from fig. 5.21, no cross peaks are seen between the outer parts of the 1D MAS spectrum and the central 'area'. It is thought this is due to offset problems that arise in the pulse sequence, so that it is believed that this sample is all of the same phase, as proposed by Gover et al.[3] This experiment does reinforce the observation from the 1D MAS that it would appear that the structure of SnP_2O_7 is more complex than that of ZrP_2O_7.

5.3.4 2D MAS Double Quantum Through-Space Experiments

In the case of ZrP_2O_7 double quantum experiments allowed the number of unique phosphorus sites to be known and hence it was possible to assign the correct space group. The 1D MAS and the RFDR experiments shown above had already suggested a more complex structure for SnP_2O_7, which would mean more than 27 phosphorus sites. The POST-C7 experiment shown below (fig. 5.22) illustrates a considerable lack of resolution compared to that seen in the ZrP_2O_7 case.
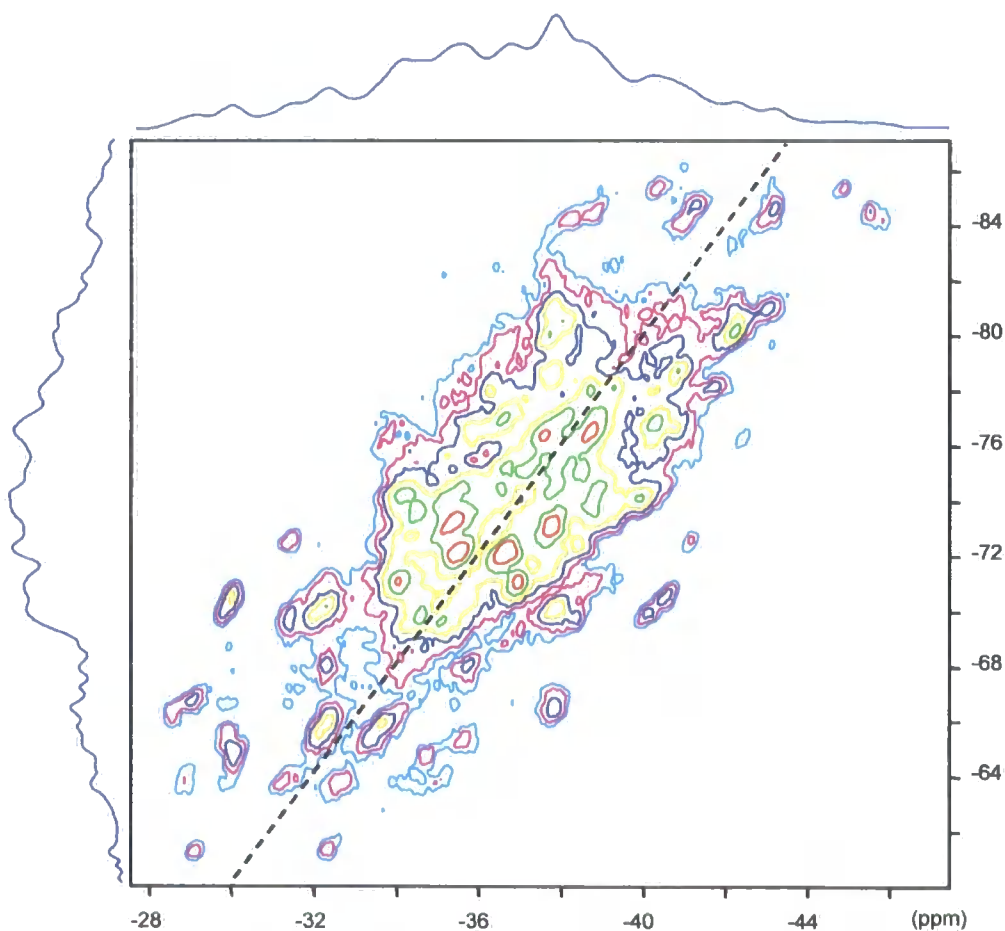
Figure 5.22. 2D POST-C7 spectrum of SnP_2O_7 showing through-space interactions.

This 'lack of resolution' is due to the complex nature of the structure, and in this case this experiment does not allow us to assign the correct space group to the structure of SnP_2O_7. However some information is available: no peaks are seen along the diagonal, removing the possibility of a number of space groups, including $Pa\bar{3}$, $R\bar{3}$, $P2_13$, $Pbca$, R3, $P2_1/c$ and $P\bar{1}$ just from this relatively simple bit of information; at least 27 pairs of phosphorus atoms are present, so a minimum of 54 phosphorus sites. These two bits of information leave only five possible space groups, $P2_12_12_1$ (54 ^{31}P sites), $Pca2_1$ (54 ^{31}P sites), $P2_1$ (108 ^{31}P sites), Pc (108 ^{31}P sites) and $P1$ (216 ^{31}P sites). It is likely, however, that more than 54 ^{31}P sites are present, which would discount the first two of the five remaining possible space groups. In an attempt to gain more information through-bond experiments were attempted.

5.3.5 2D MAS Double Quantum Through-Bond Experiments

The first experiment to be done was the POST-C9 experiment, as was done in the case of ZrP_2O_7.
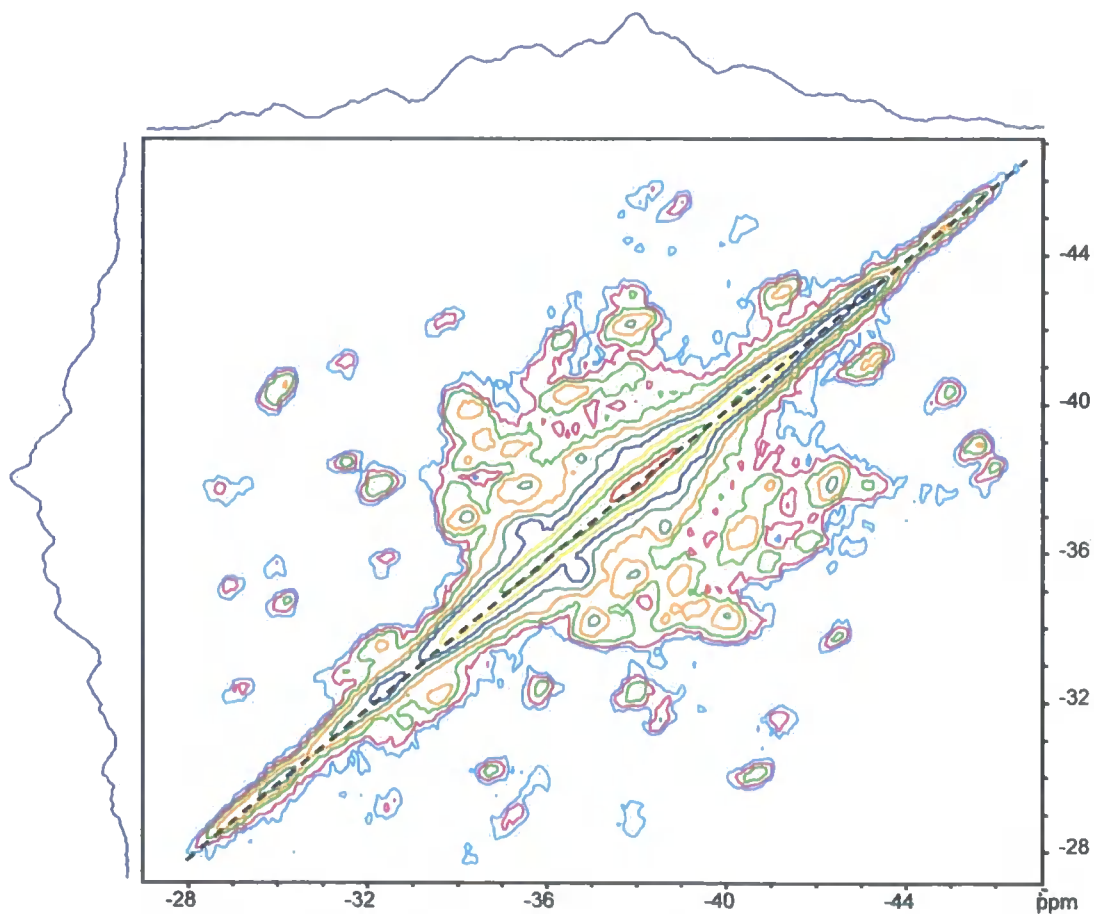
Figure 5.23. 2D POST-C9 spectrum of SnP_2O_7 showing through bond interactions.

This is shown in fig. 5.23. Again, the resolution, due to overlapping of peaks, is not good enough to allow space group assignment. This spectrum does give better resolution than the 2D POST-C7 experiment, and due to this it is possible to pick out at least 28 phosphorus pairs, giving a minimum of 56 phosphorus sites, discounting the two space groups, $P2_12_12_1$ and $Pca2_1$, both of which would contain 54 phosphorus sites. A recent study by Fayon *et al.*[23] showed the advantages of the refocused INADEQUATE experiment[24] as a probe of through-bond P–P connectivities. Like the POST-C7 experiment this experiment also uses double-quantum excitation and reconversion so that the 1D spectrum does not appear along the diagonal. This experiment was repeated for this system, and the spectrum is shown in fig. 5.24.
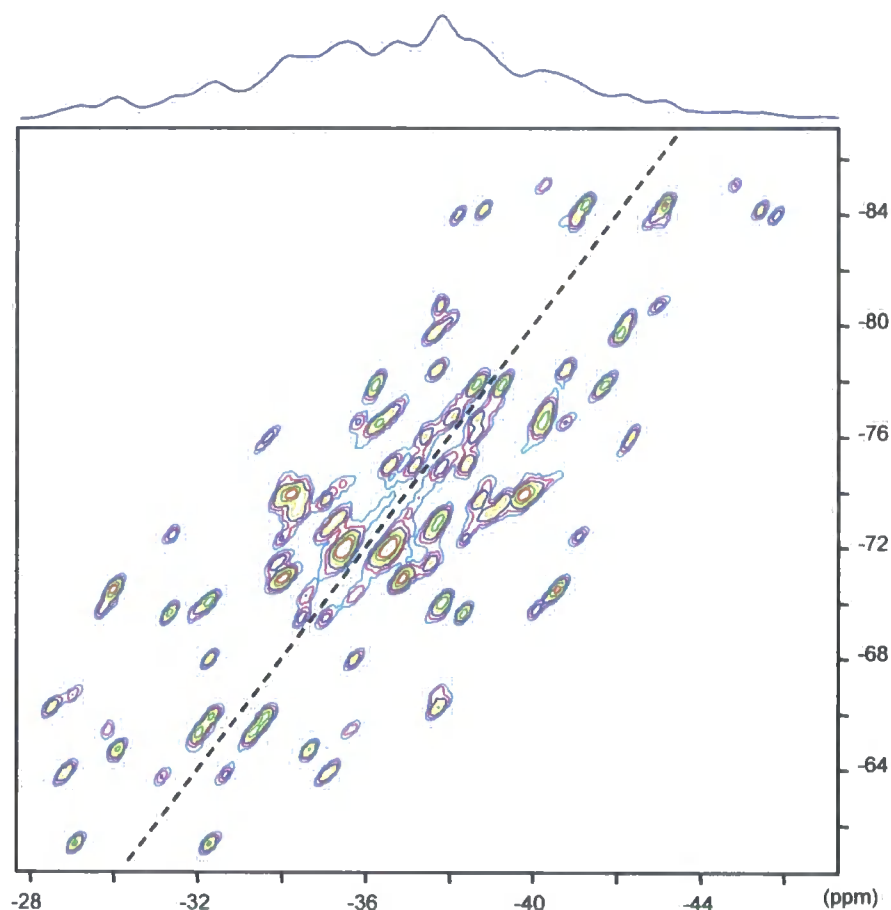
Figure 5.24. 2D refocused INADEQUATE experiment of SnP_2O_7.

This experiment clearly gives much greater resolution when compared to the experiments presented earlier. It can easily be seen from this spectrum that at least 39 P–P pairs exist, meaning a minimum of 78 unique phosphorus sites. This spectrum also confirms the lack of

autocorrelation(s) along the diagonal. One problem that has been seen with this experiment arises from off-set effects, meaning that fitting is difficult, if not impossible, as the off-set problem gives rise to incorrect relative intensities in the spectrum. A fit has been attempted using the dmfit program.[20] The fit was done on a sheared spectrum (fig. 5.25) as this halves the number of parameters that have to be fitted, and has no effect on the result. The best fit (fig. 5.26) obtained corresponds to 216 individual phosphorus sites, so the space group *P*1.
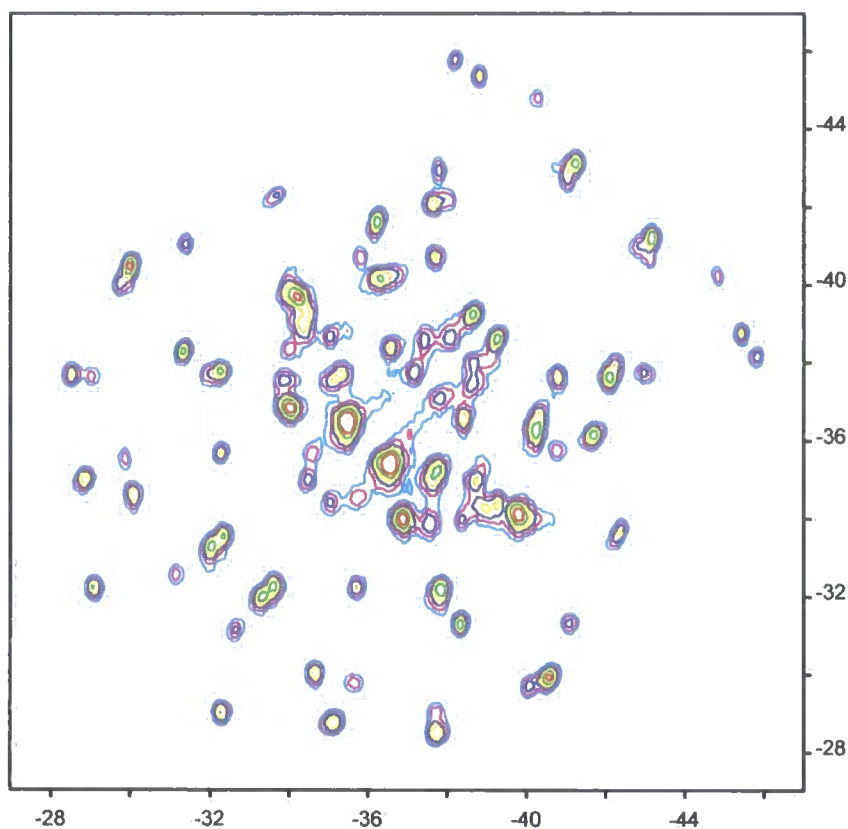
Figure 5.25. 2D refocused INADEQUATE spectrum of SnP$_2$O$_7$ after shearing.

However, as already stated, off-set effects give problems with relative intensities, so this fit cannot be taken as being definitive, but is shown here to illustrate that fitting of a spectrum this complicated is possible. Therefore it may be that 108 phosphorus sites exist, rather than 216, as it is possible to obtain a fit for 108 sites, although using 216 sites a better fit is obtained. A *P*2$_1$ space group, containing 108 unique phosphorus sites, would be consistent with the 2$_1$ symmetry axis noted by Gover *et al.*[3]

5.3.6 Conclusions on SnP₂O₇

SnP_2O_7 is the fourth material in the AM_2O_7 family that along with GeP_2O_7[14], ZrP_2O_7[16] and

HfP_2O_7 has been shown not to exist at room temperature with a $Pa\bar{3}$ space group. Indeed, the

work presented here, and the study by Gover *et al.* shows that this material has the most

complicated structure of this family, in studies to date.
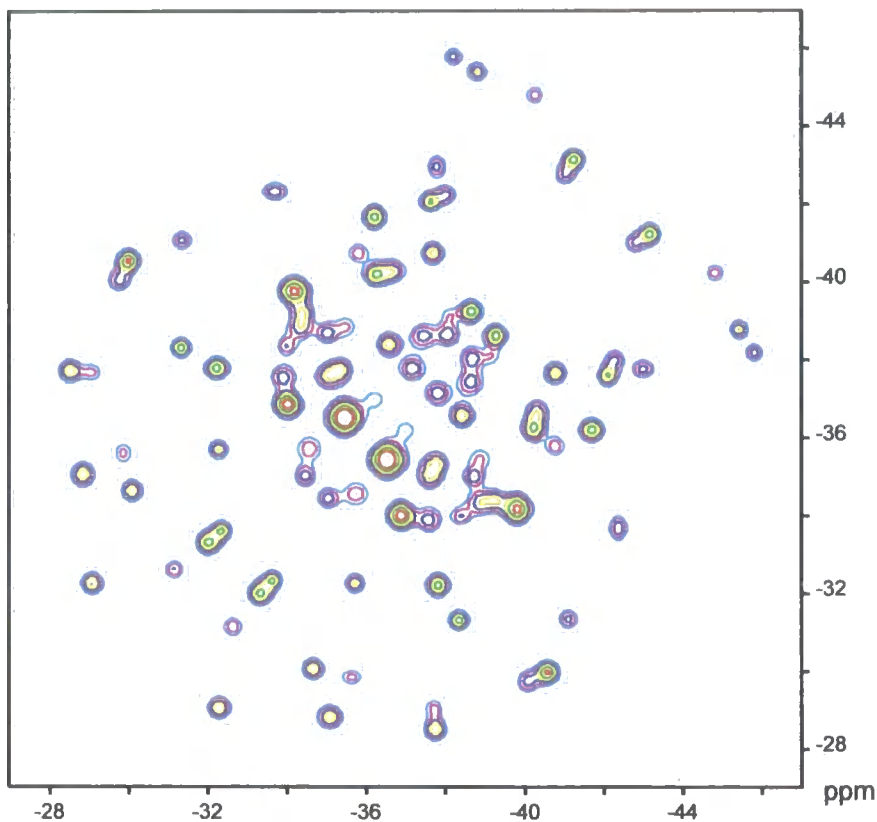
Figure 5.26. A fit of the sheared 2D refocused INADEQUATE experiment using 216 phosphorus sites all with a 1:1 intensity ratio.

The NMR experiments have made it possible to rule out nine of the 12 possible space groups,

and it is hoped that this information will be able to be used in attempted fitting of the X-ray and

neutron data. Indeed when used in conjunction with the latest methods of structure

determination from X-ray powder diffraction it may well be possible to solve this structure.[25]

Clearly further work is required, and it is likely this will come from the diffraction side rather than

the NMR side.

5.4 PbP₂O₇

Although little studied, PbP_2O_7 has been shown by electron diffraction[26] to have an incommensurate superstructure at room temperature. As part of this study both 1D and 2D MAS NMR experiments were carried out, shown in fig. 5.27 and fig. 5.28 respectively.

| 0.0 | -8.0 | -16.0 | -24.0 | -32.0 | -40.0 (ppm) |
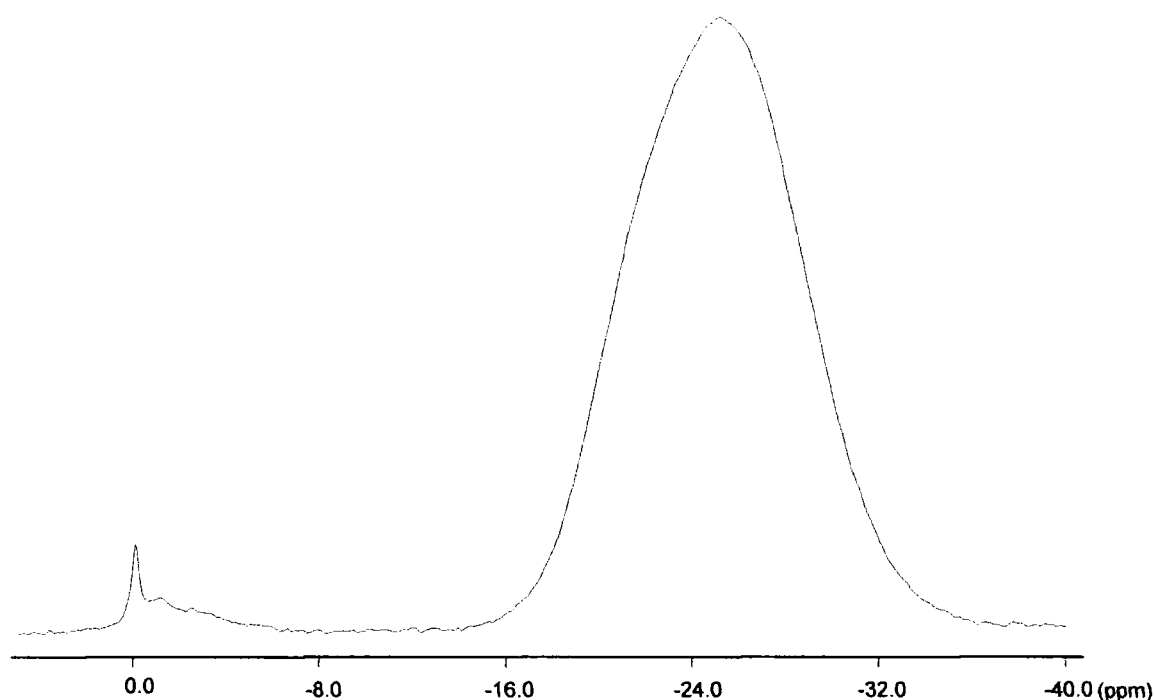
Figure 5.27. 1D MAS NMR ³¹P spectrum of PbP₂O₇. The broad band between ~-16 and ~-33 ppm is believed to be from PbP₂O₇, while the band at ~0 ppm is thought to be an impurity, probably phosphoric acid.

As can be seen from the 1D spectrum a peak appears at around 0 ppm, possible due to a phosphoric acid impurity from the synthesis. The main 'band' is due to PbP_2O_7, and has no clearly defined regions in contrast to both ZrP_2O_7 and SnP_2O_7. This could be due to either a lack of sample crystallinity due to the method of preparation or due to the presence of an incommensurate phase, which would give rise to a large number of phosphorus sites that, although unique, would be in very similar environments. With this knowledge a 2D 2Q POST C7 experiment was carried out in an attempt to gain better resolution. As has been shown this experiment does not give any intensity along the diagonal apart from autocorrelations. It would be expected that if the broad shape of the 1D MAS NMR experiment was due to lack of crystallinity, then a 2D 2Q POST C7 spectrum would contain some cross peaks, although there may be some lack of resolution. However from fig. 5.28 no defined regions appear to exist, with

all the intensity along the diagonal.   It is thought that this is due to the sample being an incommensurate phase.
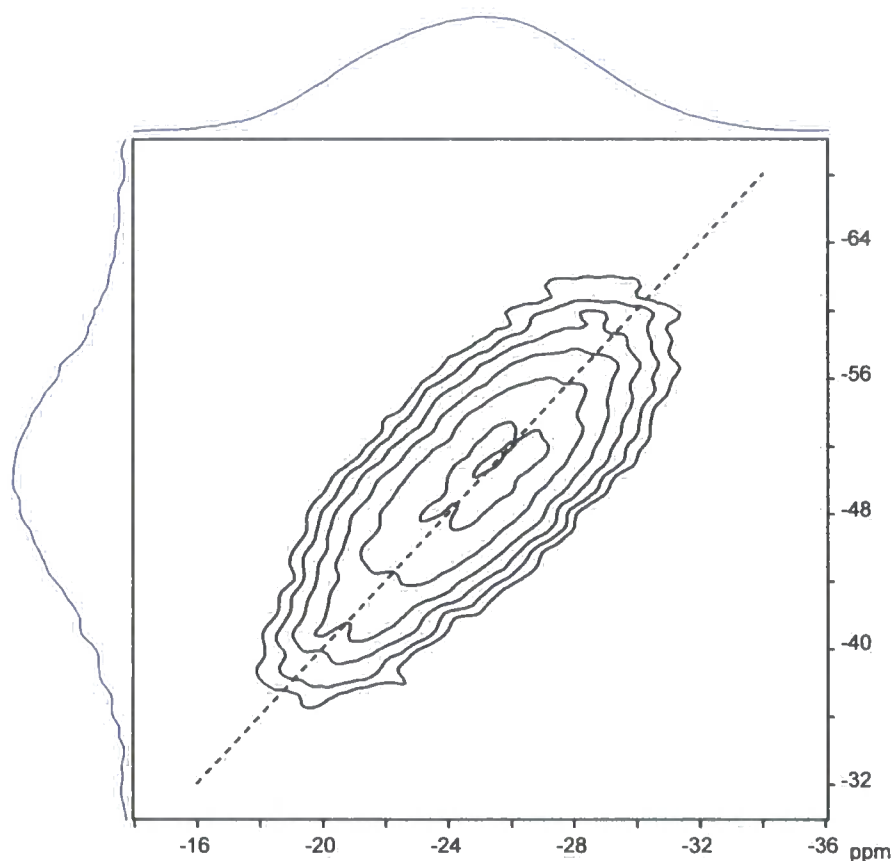
Figure 5.28. 2D POST-C7 spectrum of PbP_2O_7.

If this is an incommensurate phase, then a lack of resolution would be expected, as a large number of phosphorus environments would exist that are only subtly different, so essentially a continuum of chemical shifts (when compared to similar structures) would then be expected, as is seen experimentally.

5.5 CeP$_2$O$_7$

CeP$_2$O$_7$ has been previously shown to exist with a cubic subcell, a = 8.5648 Å, although no supercell was confirmed.[27] A simple 1D ^{31}P MAS NMR spectrum of CeP$_2$O$_7$ was recorded as part of this study, as shown in fig. 5.29. As in the case of PbP$_2$O$_7$, this 1D MAS spectrum does not give much information by itself, and is consistent with either relatively low crystallinity or an incommensurate superstructure.
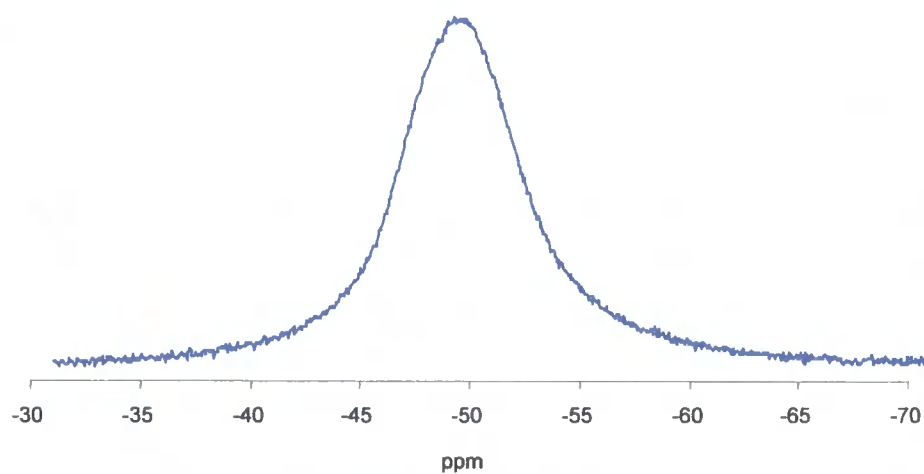
Figure 5.29. The 1D ^{31}P MAS NMR spectra of CeP$_2$O$_7$ recorded on a Varian Unity Plus 300, with a MAS frequency of 10 kHz.

It is perhaps worth noting that the broad peak seen in fig. 5.29 has a width of ~ 10 ppm, similar to the spectra of ZrP$_2$O$_7$ and HfP$_2$O$_7$. No further studies were undertaken on this material.

5.6 ZrV₂O₇

ZrV$_2$O$_7$ is perhaps the best understood member of the AM$_2$O$_7$ family, as its room temperature structure has been solved by single-crystal diffraction,[18] and its phase transitions have been well studied.[1] However, only one ^{51}V solid-state NMR study appears to have been undertaken, by Korthuis et al.[9] In this study a room temperature 1D MAS spectrum was obtained that was similar to that of ZrP$_2$O$_7$, while high temperature spectra obtained above the phase transition temperature showed the presence of two peaks, although these were assigned as being due to a single site split by quadrupolar coupling. Here a 1D ^{51}V MAS NMR spectrum was obtained and is shown in fig. 5.30.
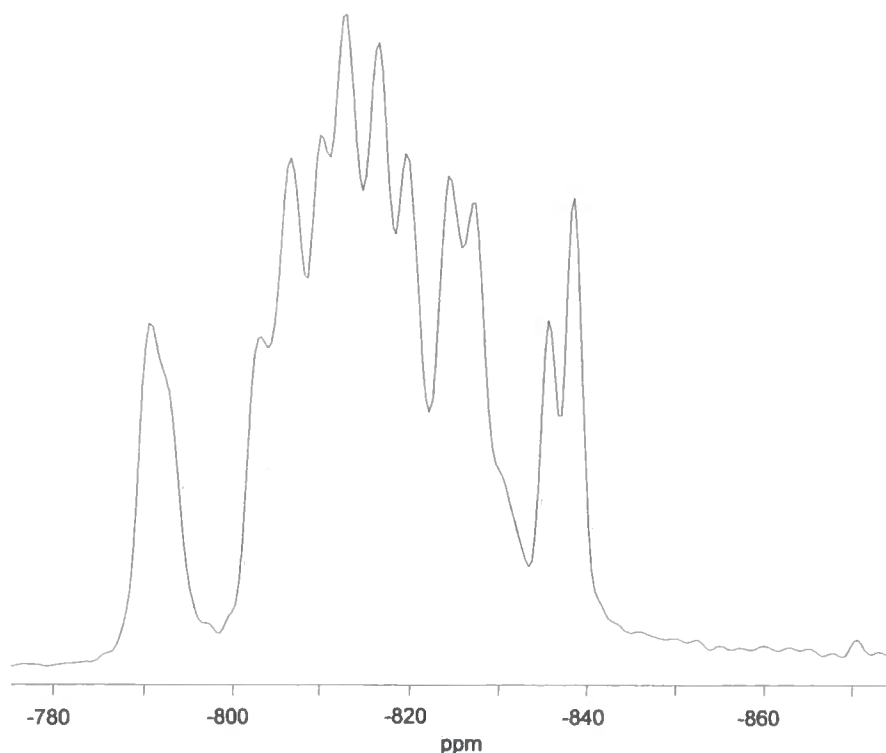
Figure 5.30. 1D ^{51}V MAS NMR spectrum of ZrV$_2$O$_7$. 11 individual resonances (probably 12) are clearly defined, with shoulders present on some of these.

This spectrum appears to show at least 12 unique vanadium sites present in the structure, which in not compatible with the structure as presented from single-crystal XRD by Evans et al.[18] for which 11 unique sites are present. The presence of 12 vanadium sites does not fit any

of the possible space groups (fig 5.8, replacing vanadium for phosphorus). It is possible that there are many overlapping resonances, as was shown in the case of ZrP_2O_7, however such a high degree of overlap (only 1 extra peak being visible, as a shoulder, over the number expected) seems unlikely. An alternative explanation is that the shoulder present on the peak at highest frequency is not due to a unique vanadium site, but rather it is due to quadrupolar coupling. To distinguish between these possibilities further NMR studies, including MQMAS studies and work at different applied fields, must be undertaken. This work, along with high-temperature NMR is currently being done by Hodgkinson & co-workers (University of Durham). Initial high temperature work by this group of workers, at temperatures above the phase transition, has also shown two peaks, but the sample used appears to be of higher crystallinity than that used by Korthuis et al.,[9] and the two peaks are more defined. At this stage this group has been unable to rule out the presence of two peaks due to quadrupolar coupling, as opposed to two unique vanadium sites, but if the latter of these two possibilities is true then this will mean an extended study will need to be undertaken on all of the materials in this family, above their phase transition temperatures. If one of these materials is shown to exist above its phase transition with a space group that is not $Pa\bar{3}$ then it may be that this is the actual case for others in the family.

Although the spectrum presented here cannot give any conclusive information, further work utilising variable temperature NMR on ZrV_2O_7 may prove of great interest to workers in this field.

5.7 Conclusions

The AM_2O_7 family of materials has proved to be extremely interesting, with many subtle differences in room-temperature structure, even though it is thought that at high enough temperatures they would all exist with a cubic $Pa\overline{3}$ space group. Before this study only two materials, GeP_2O_7[14] and SnP_2O_7,[3] had been shown to exist with a room-temperature superstructure that was not in space group $Pa\overline{3}$, and an assumption appeared to exist within the literature that all the other members of the AM_2O_7 family existed with this $Pa\overline{3}$ space group at room temperature. This study has clearly shown that in two cases, ZrP_2O_7 and HfP_2O_7, this is not true, and has supported the XRD study of SnP_2O_7 by Gover et al.[3] The observation that these apparently simple materials have (in this work) up to 540 crystallographically unique atoms in their asymmetric unit is remarkable. The reasons for these differences in structure are, presumably, subtle differences in the structure because the metal is changed, which causes the lowest energy conformation to change.

One case that is of special importance for future work is the case of ZrV_2O_7, which raised a number of questions, although answers to these will only be known after further ^{51}V solid-state NMR studies.

This work has shown the power of using a combination of techniques to determine structures. In the case of ZrP_2O_7, powder XRD studies gave 12 possible space groups and the use of solid-state NMR allowed the determination of just one of these space groups, while electron diffraction showed the presence of an incommensurate phase. So, powder XRD allowed both a speedy check of sample purity and crystallinity (with respect to solid-state NMR), and, when the information on the space group obtained from NMR was taken into account, allowed the room-temperature structure of ZrP_2O_7 to be found. With 136 crystallographically unique atoms, this is one of the most complex structures solved to date using powder methods.

5.8 Future Work

A number of systems studied here, including ZrV_2O_7, CeP_2O_7, PbP_2O_7 and SnP_2O_7, clearly warrant further study, using a combination of techniques. There are also a number of other related materials, as discussed in Chapter 4, that have not been investigated; a large number of these would also be of interest to study, as understanding all of the structures will hopefully allow the 'bigger picture' to be seen, and enable the subtle factors that cause some of these materials to exhibit isotropic NTE to be determined. One problem with some of these materials, in respect to a multi-technique approach, arises for systems such as NbP_2O_7 and WP_2O_7, which are paramagnetic in nature, causing problems for the application of NMR. However, it is clear a large amount of work is required in studying these structures, but this study has laid the foundations for future work.

5.9 References

(1)   Withers, R. L.; Evans, J. S. O.; Hanson, J.; Sleight, A. W. *J. Solid State Chem.* 1998, **137**, 161-167.

(2)   Withers, R. L.; Tabira, Y.; Evans, J. S. O.; King, I. J.; Sleight, A. W. *J. Solid State Chem.* 2001, **157**, 186-192.

(3)   Gover, R. K. B.; Withers, N. D.; Allen, S.; Withers, R. L.; Evans, J. S. O. *J. Solid State Chem.* 2002, **166**, 42-48.

(4)   Levi, L. R.; Peyronel, G. *Z. Krist* 1935, **92**, 190 - 209.

(5)   Vollenke, H.; Wittmann, A.; Novotny, H. *Monatsh. Chemie* 1963, **94**, 956-963.

(6)   Hagman, L.; Kierkegaard, P. *Acta Chem. Scand.* 1969, **23**, 327-328.

(7)   Chaunac, M. *Bull. Soc. Chim. Fr.* **1971**, 424-429.

(8)   Pascard, R.; Chaunac, M.; Grison, E. *Bull. Soc. Chim. Fr.* **1971**, 429-435.

(9)   Korthuis, V.; Khosrovani, N.; Sleight, A. W.; Roberts, N.; Dupree, R.; Warren, W. W. *Chem. Mater* 1995, **7**, 412-417.

(10)   Coehlo, A.; Bruker: Karlsruhe, Germany, 2000.

(11)   Hartmann, P.; Jana, C.; Vogel, J.; Jäger, C. *Chem. Phys. Lett.* 1996, **258**, 107-112.

(12)   Iuliucci, R. J.; Meier, B. H. *J. Am. Chem. Soc.* 1998, **120**, 9059-9062.

(13)   Helluy, X.; Marichal, C.; Sebald, A. *J. Phys. Chem. B* 2000, **104**, 2836 - 2845.

(14)   Losilla, E. R.; Cabeza, A.; Bruque, M. A.; Aranda, M. A. G.; Sanz, J.; Iglesias, J. E.; Alonso, J. A. *J. Solid State Chem.* 2001, **156**, 213-219.

(15)   Maricq, M. M.; Waugh, J. S. *J. Chem. Phys.* 1979, **70**, 3300-3316.

(16)   King, I. J.; Fayon, F.; Massiot, D.; Harris, R. K.; Evans, J. S. O. *Chem. Comm.* **2001**, 1766-1767.

(17)   Bennett, A. E.; Ok, J. H.; Griffin, R. G.; Vega, S. *J. Chem. Phys.* 1992, **96**, 8624-8627.

(18)   Evans, J. S. O.; Hanson, J. C.; Sleight, A. W. *Acta Cryst. B* 1998, **54**, 705-713.

(19)   Hohwy, M.; Jakobsen, H. J.; Edén, M.; Levitt, M. H.; Nielsen, N. C. *J. Chem. Phys.* 1998, **108**, 2686-2694.

(20)   Massiot, D.; Fayon, F.; Capron, M.; King, I.; Le Calvé, S.; Alonso, B.; Durand, J.-O.; Bujoli, B.; Gan, Z.; Hoatson, G. *Magn. Reson. Chem.* 2002, **40**, 70-76.

(21)   Heindrichs, A. S. D.; Geen, H.; Giordani, C.; Titman, J. J. *Chem. Phys. Lett.* 2001, *335*,

          89-96.

(22)   Hardy, E. H.; Verel, R.; Meier, B. H. *J. Magn. Res.* 2001, *148*, 459-464.

(23)   Fayon, F.; Le Saout, G.; Emsley, L.; Massiot, D. *Chem. Comm.* **2002**, 1702-1703.

(24)   Lesage, A.; Bardet, M.; Emsley, L. *J. Am. Chem. Soc.* 1999, *121*, 10987-10993.

(25)   Evans, I. R. In *IuCr XIX*: Geneva, 2002.

(26)   Brindley, J.; 4ᵗʰ year thesis, Department of Chemistry, University of Durham, 2001.

(27)   Tait, M. M.; 4ᵗʰ year thesis, Department of Chemistry, Durham University, 2002.

Chapter 6

ZrW_2O_8 – ^{17}O Variable Temperature MAS NMR

6.0 ZrW_2O_8 - Background

ZrW_2O_8 is a material of considerable academic and technological interest as it has been shown to exhibit isotropic negative thermal expansion (NTE) over a wide temperature range.[1,2] As can be seen in fig. 6.1 NTE is seen from close to absolute zero up to 1500 K, with a thermal expansion coefficient of $\alpha_1 = -9 \times 10^{-6} K^{-1}$ (0-350 K).
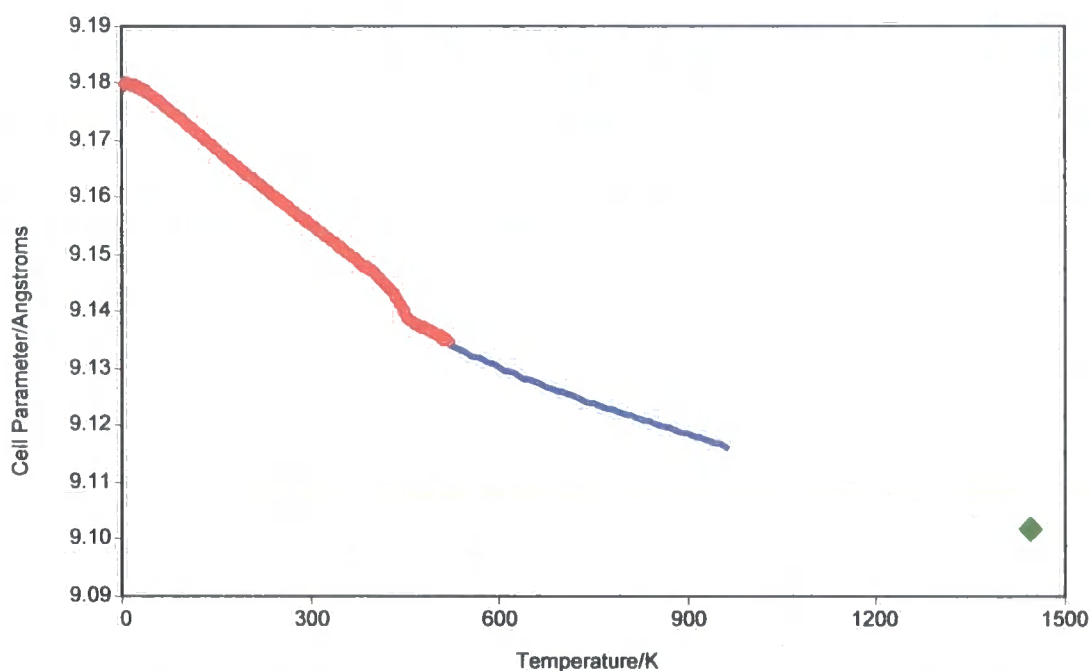
Figure 6.1. The cell parameter of ZrW_2O_8 shown as a function of temperature. The plot shows information derived from neutron data (red and green points), and from dilatometer data (blue). This plot has been copied from ref. 5, with the kind permission of the author.

The structure of ZrW_2O_8 and its related family ($Zr_{1-y}Hf_yW_{2-x}Mo_xO_8$) is similar to that of the AM_2O_7 materials, with an extra oxygen atom inserted, so that M_2O_8 groups are contained within the structure rather than M_2O_7 groups. The structure of ZrW_2O_8 is shown in fig. 6.2.
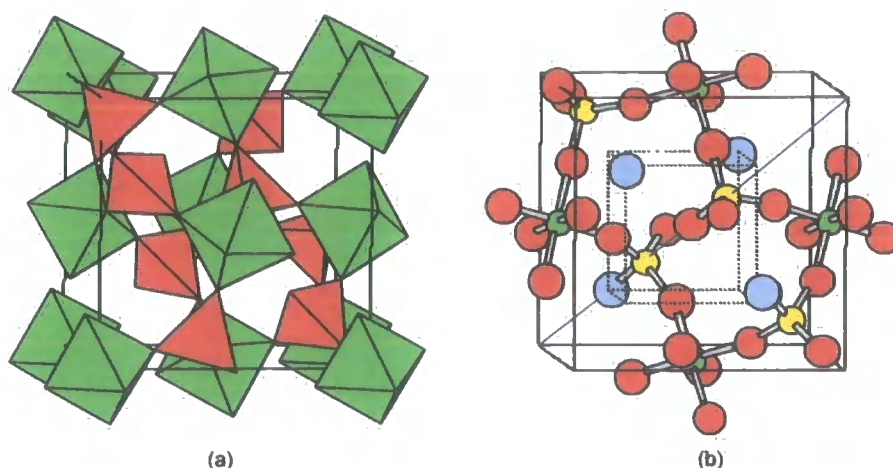
Figure 6.2. The structure of cubic ZrW_2O_8 shown in (a) a polyhedral representation with (green) ZrO_6 octahedra that share corners with (red) WO_4 tetrahedra; (b) a ball and stick representation, with: Zr (green), W (yellow), and two-coordinate oxygen atoms (red). The WO_4 tetrahedra lie along the main diagonal on the cubic unit cell and contain one strictly one-coordinate oxygen (blue).

ZrW_2O_8 has been described by Evans *et al.*[3] as having a framework structure containing corner sharing ZrO_6 octahedra and WO_4 tetrahedra. Each octahedron shares all 6 of its corner oxygen atoms with a tetrahedron; each tetrahedron, however, shares only 3 of its 4 corners with an octahedron. This then means that each WO_4 tetrahedron contains one oxygen atom that is formally one coordinate, an unusual arrangement for the solid-state. The structure also contains a W–O–W bridge that contains one short W–O bond, 1.7 Å, and one long W–O bond, 2.4 Å, with this latter distance being just within in the limits of being able to be considered a bonding interaction. Pryde *et al.*[4] have shown that ZrW_2O_8 contains a family of RUM's and qRUM's (see section 4.0.2), which give rise to an unusually high phonon density of states at low energy. It is these low energy modes which give rise to NTE. As a material, ZrW_2O_8 is metastable, being synthesised from ZrO_2 and WO_3 at around 1450 K, where it is kinetically stable, and then quickly quenched to room temperature. The material is also only thermodynamically stable with respect to ZrO_2 and WO_3 above ~1400 K, which is thought to be partly due to the unusual entropic stability due to both vibrational modes and oxygen disorder (see below) present at this temperature. The synthesis of ZrW_2O_8 will be discussed further in the section 6.2.3 in respect to the incorporation of ¹⁷O into the structure.

Although ZrW_2O_8 shows continuous NTE from over a wide temperature range a phase transition is seen at around 448 K,[3] as is apparent from the cell discontinuity in fig. 6.1. This phase

transition sees the material going from an acentric $P2_1$3 structure (α-form) to a disordered

centric $Pa\bar{3}$ structure (β-form). This is shown schematically below in fig. 6.3.
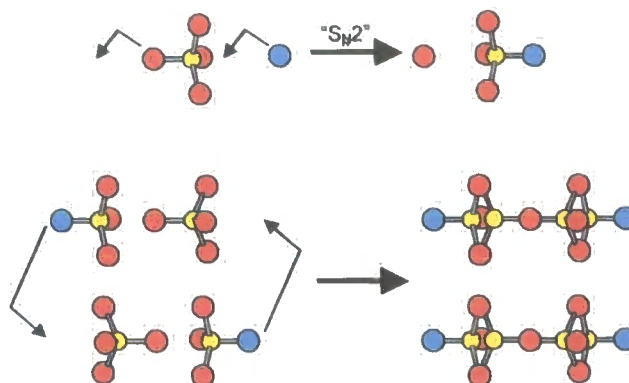
Figure 6.3. The "S$_N$2" type mechanism that is thought to occur at the temperature driven phase transition, which is an order-disorder transition.[5] The top picture is a section of the bottom picture, with this latter diagram showing a time average 'picture' on the right

As can be seen from fig. 6.3 the phase transition brings about the 'hopping' of two of the oxygen atoms, in an S$_N$2 manner. This process can be looked on as creating a mobile oxide ion that migrates from one WO$_4$ tetrahedron to another, reversing the direction in which the WO$_4$ tetrahedra face, leading to a disordered average structure.[3] The fact that oxygen migration occurs at these very low temperatures is remarkable. Another phase transition exists for this material, the α to γ–ZrW$_2$O$_8$ transition, this being pressure induced.[6,7] This phase transition occurs at a pressure of around 2 kbar, with cubic α–ZrW$_2$O$_8$ going to orthorhombic γ–ZrW$_2$O$_8$. This phase transition is more complicated than the α to β phase transition, but again concerted oxygen migration is thought to occur that reverses the direction of one in three of the WO$_4$ tetrahedra. This phase transition is well described in a review by Evans.[5] Other members of this family include ZrWMoO$_8$ and ZrMo$_2$O$_8$, which exhibit similar α to β phase transitions, but at lower temperatures, although these phases are more difficult to prepare than ZrW$_2$O$_8$.[8]

The α to β phase transition is of interest in this study, as the mechanism involved has only been studied via diffraction techniques, and supporting evidence from NMR would be of great benefit in understanding it. Three mechanisms are possible for this transition:

I) The S$_N$2 type mechanism shown in fig. 6.3, and discussed above. This process is invoked in the literature as the most likely mechanism,[3] as it is chemically plausible, and although oxygen

'hopping' is seen, this can be rationalised by taking account of vibrations in the structure thought to be key to the NTE behaviour. In fig 6.3 it can be seen that the tungsten atom oscillates between two points, and it is this oscillation that allows the oxygen to 'hop'. This mechanism is shown in a different manner in fig. 6.4.
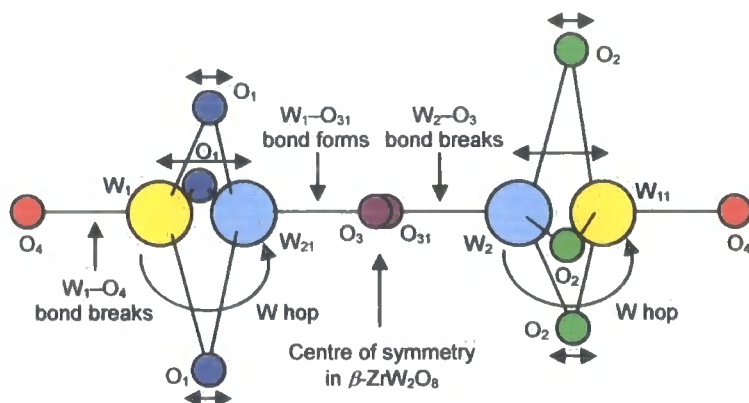
Figure 6.4. The hopping mechanism shown in figure 6.3 is shown again. In this representation of the α–β order-disorder transition α–ZrW$_2$O$_8$ sites W$_1$, W$_2$, O$_1$, O$_2$, O$_3$ and O$_4$ are occupied, with sites W$_{11}$, W$_{21}$, O$_{31}$ and O$_{41}$ becoming 50% occupied in β–ZrW$_2$O$_8$. As can be seen from fig. 6.3, O$_4$ hops to another WO$_4$ tetrahedron to become O$_{41}$, i.e. O$_4$ and O$_{41}$ in this figure are not the same oxygen atom.

This model shows that in the β-form O$_1$ and O$_2$ become equivalent, while the 'hopping' of O$_4$ means that when this oxygen 'hops' it becomes O$_{41}$, in the same process O$_3$ becomes O$_{31}$ and W$_1$ becomes W$_{21}$, while W$_2$ becomes W$_{22}$. To model the α-to-β phase transitions Evans et al. assumed two independent WO$_4$ tetrahedra in α–ZrW$_2$O$_8$ can invert independently, but the terminal oxygen migration, O$_4$, occurs at the same rate as the tungsten site hopping, so that each tungsten retains tetrahedral coordination throughout the process.[3] This view of the temperature driven phase transition of ZrW$_2$O$_8$, as already stated, appears chemically sensible and does not require any strong bridging Zr–O–W bonds to be broken at relatively low temperatures. In NMR terms very little difference would be expected between the ^{17}O MAS NMR spectra for the two forms of ZrW$_2$O$_8$ apart from, possibly, the peaks for O$_1$ and O$_2$ coalescing.

II) A possible alternative to the mechanism described above would the formation of discreet W$_2$O$_7$ and W$_2$O$_9$ groups in the structure, which would be bought about by oxygen hopping, similar to mechanism I, except in this case the process would not be a concerted one.[9]

III) A third possible process is one in which all of the oxygen atoms migrate at the phase transition. However, this would necessitate the need for the breaking of Zr–O bonds, as well as W–O bonds, and this mechanism was thought unlikely in the literature. In fig. 6.4 this could be seen as O_4 moving to an O_1 site, and O_1 moving to an O_3 site, and so on.

6.1 ^{17}O Solid-State NMR - Background

^{17}O is a quadrupolar nucleus ($I = {}^{5}/_{2}$) and has a very low natural abundance of only 0.037 %, making solid-state NMR quite difficult. Unfortunately this is the only oxygen isotope that is accessible via NMR, so enrichment is required. Due to the cost of ^{17}O and the effort involved in enriching samples, early development of ^{17}O solid-state NMR was limited. ^{17}O has been characterised by Mackenzie & Smith[10] as a nucleus with a small quadrupolar moment and a large chemical shift range. However, the quadrupolar interaction is a strong function of the covalency of the M–O bond, so that oxygen atoms in highly covalent environments will have large quadrupolar broadening associated with them.

An increasing number of systems are being studied via ^{17}O NMR, using a range of NMR methodologies including MAS, DAS (Dynamic Angle Spinning) and MQMAS (Multi-Quantum MAS). All three of these experiments have been compared in a study by Xu and Stebbins.[11] As discussed below ZrW_2O_8 is synthesised from ZrO_2 and WO_3. It would appear from the literature that no ^{17}O NMR studies have been undertaken on the latter material, although there are a number of studies on the former.[12,13] These studies have shown that ^{17}O NMR can readily distinguish the three polymorphic (monoclinic, tetragonal and cubic) forms of ZrO_2, even without enrichment. The monoclinic form has been shown to exhibit two very sharp resonances (linewidths of ~ 2 ppm) separated by 77 ppm and the tetragonal form gives rise to just one peak at ~ 374 ppm. The cubic phase needs to be stabilised at room temperature by doping with an oxide such as MgO, and this gives a solid-solution with a range of next nearest neighbours, shifting the signal from the tetragonal resonance position and with a much increased linewidth of ~ 84 ppm.[13] It is also worth noting that it would appear that, from literature searches, no previous ^{17}O NMR studies of ZrW_2O_8 have been undertaken.

6.2 Results and Discussion

6.2.1 ZrO_2 – XRD and ${}^{17}O$ MAS NMR

ZrO_2 is one of the two starting materials used, along with WO_3, in the synthesis of ZrW_2O_8. To obtain an enriched sample of ZrW_2O_8 enriched starting materials were first synthesised. $Zr^{17}O_2$ was synthesised using $ZrCl_4$ and ${}^{17}O$ enriched H_2O under an inert atmosphere. Sample purity and crystallinity were of obvious importance for not only the final product, but also the starting materials, as highly pure and highly crystalline starting materials have been shown to give the best samples of ZrW_2O_8. Fig. 6.5 shows powder XRD patterns for high purity monoclinic ZrO_2 and ${}^{17}O$ enriched monoclinic ZrO_2. It is instantly appears that the enriched material is less crystalline that the bench sample, which then gives problems in determining the purity of the enriched sample, as the lower crystallinity leads to broadening in the reflections present although this broadening is in fact due to small crystallites and not lack of crystallinity. A small amount of t-ZrO_2 impurity is seen to be present in this material. It can perhaps be presumed that any oxide impurities present in the enriched ZrO_2 sample would contain ${}^{17}O$ within their structures, so that NMR could give a good guide to purity levels. The MAS NMR spectrum of the enriched ZrO_2 sample is shown in fig. 6.6. This spectrum shows two sharp resonances at 400.8 ppm and 322.8 ppm, so the two peaks are separated by 78 ppm, in keeping with the work of Bastow & Stuart.[13] Also, it can be seen, that a third, small resonance is present at 374.4 ppm, which is due to the t-ZrO_2 impurity.
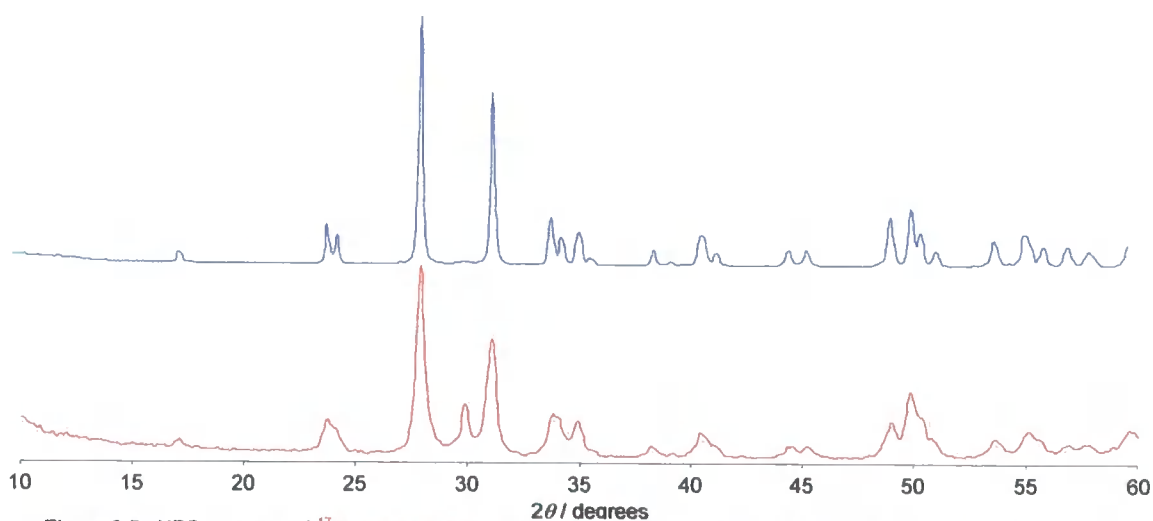
Figure 6.5. XRD patterns of ${}^{17}O$ enriched ZrO_2 (data collected on Bruker D8 over 30 mins) and bench ZrO_2 (data collected on Siemens D5000 over 50 mins).
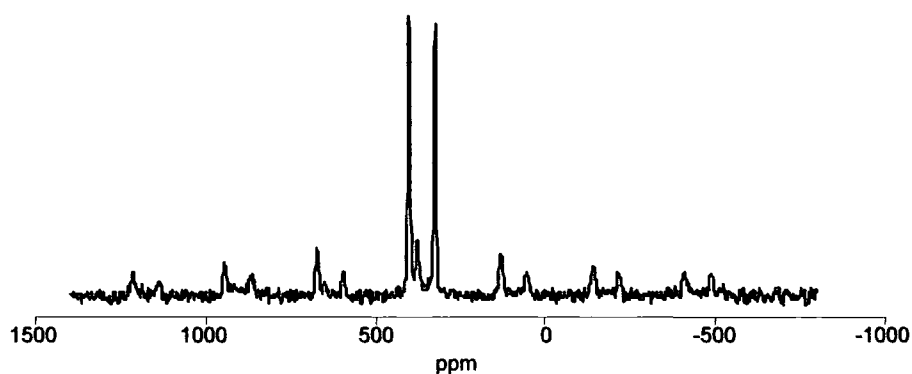
Figure 6.6. ¹⁷O MAS NMR spectrum of Zr¹⁷O₂, recorded on a Varian Unity Plus 300 spectrometer. Two ¹⁷O resonances are seen due to ZrO₂ 322.8 and 400.8 ppm. A smaller resonance is also seen at 374.4 ppm, thought to be due to an impurity.

6.2.2 WO₃ – XRD and ¹⁷O MAS NMR

Again, as in the case of ZrO₂, sample purity and crystallinity are of importance. In the case of WO₃ a number of polymorphic forms exist, but it is the monoclinic form that is stable at room temperature.[14] When preparing this material in the enriched form it was necessary to heat it in air for a short amount of time as the material initially formed was oxygen deficient (WO₃₋ₓ), and this may have led to some loss of ¹⁷O. The powder XRD pattern for the enriched material, as well as for bench WO₃ is shown in fig. 6.7. From this it can be seen that the enriched material is the correct phase, and reasonably crystalline.
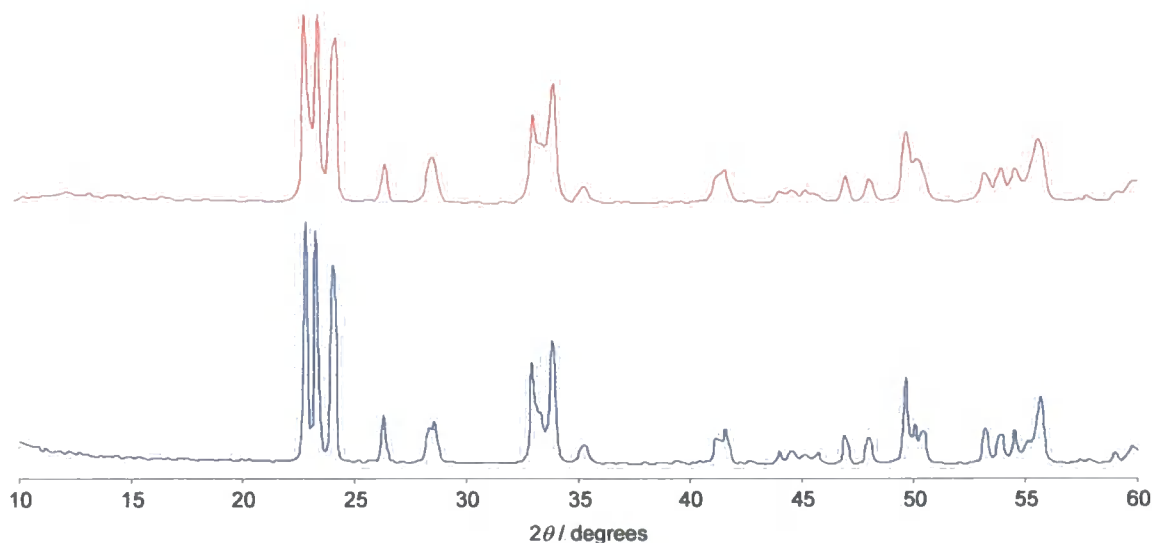
Figure 6.7. XRD patterns of ¹⁷O enriched WO_3 and bench WO_3.

The ¹⁷O NMR spectrum (fig. 6.8) shows the presence of at least three different oxygen sites. XRD studies have shown that the monoclinic form of WO_3 contains six oxygen sites, each being two coordinate with respect to tungsten. The six oxygen atoms in the asymmetric unit are essentially in pairs, two in symmetrical environments (d[W–O] = 1.864 Å / 1.917 Å & 1.856 Å / 1.936 Å), two in less symmetrical environments (d[W–O] = 1.813 Å / 2.051 Å & 1.737 Å / 2.116 Å) and two in rather unsymmetrical environments (d[W–O] = 1.707 Å / 2.194 Å & 1.719 Å / 2.200 Å).[15] The lowering of symmetry seen is caused by a well known sequence of phase transitions that WO_3 undergoes on cooling from high temperature.[14-16]

The three oxygen types can be seen in the 1D spectrum, where the peak at 576 ppm is a highly symmetric site, the peak at 527 ppm arises from a site of lower symmetry than that at 576 ppm, and the peak at ~ 435 ppm is clearly of lower symmetry again. This is consistent with the 'pairs' of oxygen atoms discussed above.

Again, no obvious impurities are seen in the ¹⁷O MAS NMR spectrum, although in this case there are no literature spectra to compare.
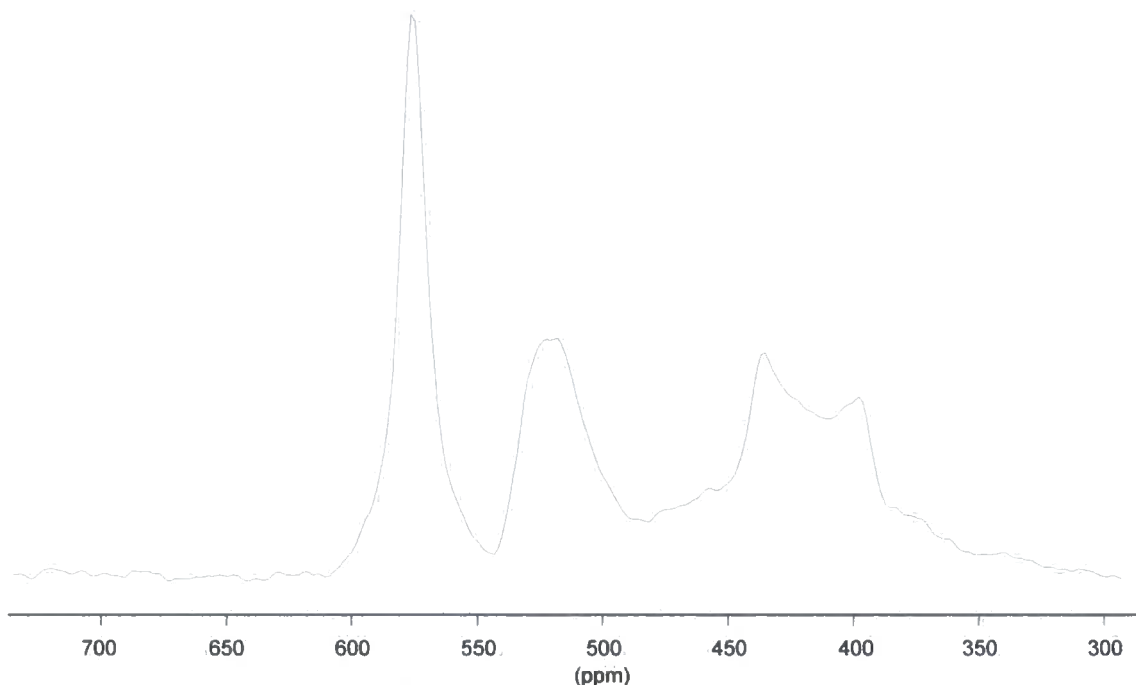
Figure 6.8. 1D ^{17}O MAS NMR spectrum of ^{17}O enriched WO$_3$ recorded on a Bruker DSX300.

6.2.3 ZrW$_2$O$_8$ – XRD and ^{17}O MAS Variable Temperature NMR

^{17}O enriched ZrW$_2$O$_8$ was synthesised from the enriched samples of ZrO$_2$ and WO$_3$ whose respective powder XRD patterns and MAS NMR spectra are presented above. These starting materials have been shown to be of high purity, although ZrO$_2$ was not highly crystalline. These oxides were ground, pressed into pellets, heated in a sealed quartz tube to 1450 K then quenched to room temperature. Despite repeated attempts, the best samples achievable by these routes contained only ~ 78% ZrW$_2$O$_8$, by mass. The XRD patterns for this sample and for a high purity 'normal' sample are shown below in fig. 6.9. The XRD pattern for the enriched sample shows the presence of ZrO$_2$ and WO$_3$ impurities, and therefore it would be expected that these same impurities would be seen in the ZrW$_2$O$_8$ NMR spectrum.
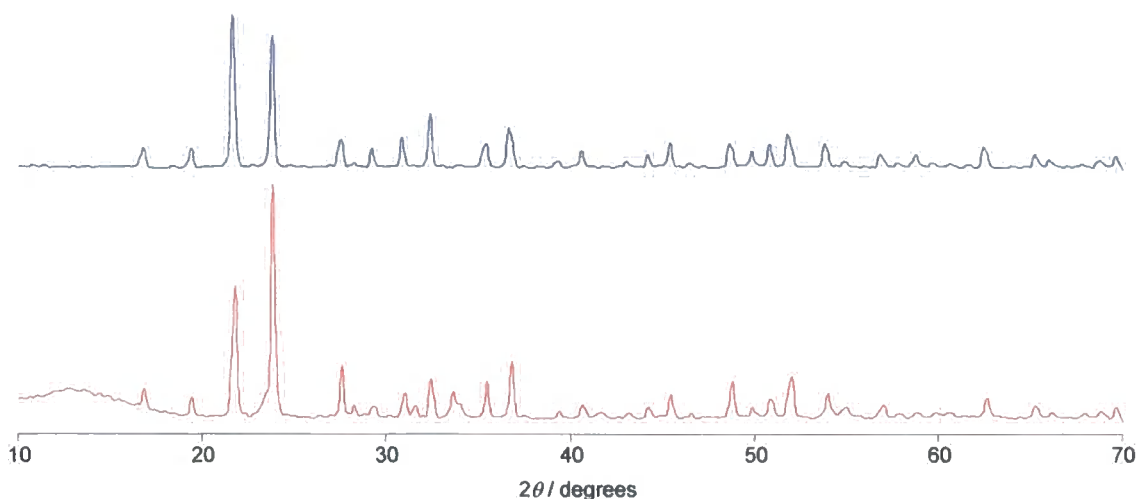
Figure 6.9 XRD patterns of ¹⁷O enriched ZrW₂O₈ (78% purity) and bench ZrW₂O₈.

It can be seen from looking at figures 6.10, 6.11 and 6.12 that this is, in fact, not the case. The ZrO_2 impurity is seen in all of the spectra of the ZrW_2O_8 sample, but the WO_3 impurity is not. In fig. 6.10, at around 460 – 520 ppm two apparent peaks are seen, but it is thought these are not due to WO_3, as fig. 6.11 shows that (comparing spectra recorded at 9 and 12 kHz) there are apparently no isotropic peaks in this region. This gives rise to the question as to what has happened to the enriched WO_3 impurity? This is an intriguing question, for which an adequate answer is difficult. One explanation could be differential rates of oxygen exchange between the two starting materials and, for example, the SiO_2 quartz tube, such that WO_3 has a higher rate of exchange than ZrO_2 and 'loses' its ^{17}O more rapidly than ZrO_2. It is worth noting that the loss of ^{17}O is not simply due to the air heating of WO_{3-x} to obtain WO_3, as the WO_3 sample is clearly seen to contain ^{17}O, from its NMR spectrum, shown in section 6.2.2. The impurities are probably more likely to have been formed during the sample quench, rather than due to lack of reaction going to completion. This could then mean that when WO_3 and ZrO_2 were being 'reformed' from ZrW_2O_8, ^{17}O was not entering the WO_3 structure. Whilst we suggest this as a possibility, we can give no adequate rationalisation.
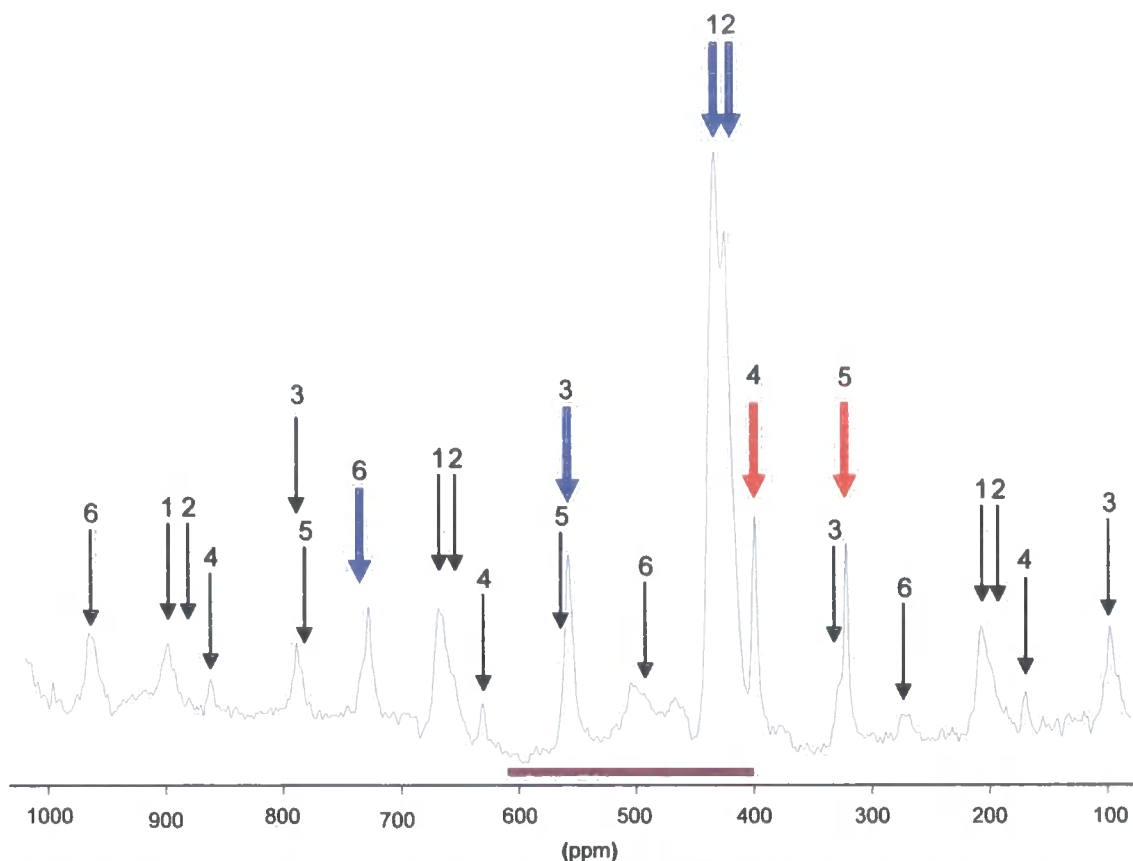
Figure 6.10. 1D ^{17}O MAS NMR spectrum of a ^{17}O enriched sample of ZrW_2O_8, shown to be 78 % pure by powder XRD. The two resonances due to ZrO_2 are highlighted by red arrows, while the peaks due to the main phase, ZrW_2O_8, are shown by the blue arrows, with spinning sidebands shown by black arrows. These have been determined by comparing spectra obtained at different spinning rates. The area in which resonances due to WO_3 would be expected to appear is highlighted by a purple line. The only apparent resonances are not thought to be due to WO_3, as discussed in the text.

To study the phase transition of ZrW_2O_8 via ^{17}O solid-state NMR, it was necessary to use variable temperature techniques, as described in section 2.1.6. The aim of this was to study the oxygen environments below and above the phase transition, to see if NMR would support any of the mechanisms in section 6.0. Below the phase transition, there are four oxygen environments present in the structure, in a 3:3:1:1 ratio. The oxygen sites of triple intensity are oxygen atoms O_1 and O_2, which are bonded to both a tungsten atom and a zirconium atom. The other two oxygen environments, O_3 and O_4, are the oxygen atom bonded to two tungsten atoms, and the one-coordinate oxygen, respectively. In the "favoured" mechanism shown in fig. 6.2, O_1 and O_2 are essentially uninvolved, but become equivalent due to the motion of O_3 and O_4. It is these latter two oxygen atoms that were presumed to undergo the most major changes at the phase transition.[3] As can be seen from fig. 6.10, the spectrum seen at room temperature is consistent with the structure, described in the literature.[3] Two large peaks are seen very close together at

426 and 434 ppm, which can be assigned to O_1 and O_2, and two lower intensity resonances are seen at ~ 560 and ~ 730 ppm, which are assigned as O_3 and O_4, respectively, as O_4, which is strictly one-coordinate, is less shielded than O_3, so can be expected to be at higher frequency. Spectra were recorded at different MAS frequencies to distinguish between spinning side bands and the centre bands, from which three isotropic groups could be identified (fig. 6.11). With the room temperature spectrum recorded and assigned, variable temperature (VT) ^{17}O MAS NMR experiments were untaken, with the spectra recorded shown in fig. 6.12. One problem when undertaking such VT work is the difference in temperature between the temperature measured by the thermocouple and the actual sample temperature within the rotor. This can be corrected by running calibration VT experiments using lead nitrate, and measuring the chemical shift of the lead within this material, as a good correlation has been shown to exist between temperature and chemical shift.[17-20] The temperatures shown in fig. 6.12 have been corrected using this so-called '^{207}Pb thermometer' technique (a calibration curve can be found in Appendix 1).

As can be seen from fig. 6.12, as the temperature of the sample is increased the two weaker resonances (those for O_3 and O_4), broaden and appear to disappear, while the peaks from O_1 and O_2 slowly broaden. This is followed by a shift to higher frequency for these latter resonances, and a continued broadening, up to 205°C. After this temperature, the position of the broad peak does not change, showing a chemical shift value of ~ 485 ppm, and an apparent decrease in linewidth. If we take the original chemical shift values of the four oxygen sites, and average these, taking into account the relative intensities, it is seen that the average, δ_{AV} = 483.7 ppm, is extremely close to the value of the single peak seen at the highest temperature. A fit of the broad peak in the spectra in fig. 6.12, shows that it becomes broader up to 205°C, before starting to decrease in width (fig. 6.13). The fit was carried out with a function that is a Gaussian-Lorentzian mix. At the higher temperatures just one broad peak was fitted, while at the lower temperatures two peaks were need for the fitting process.
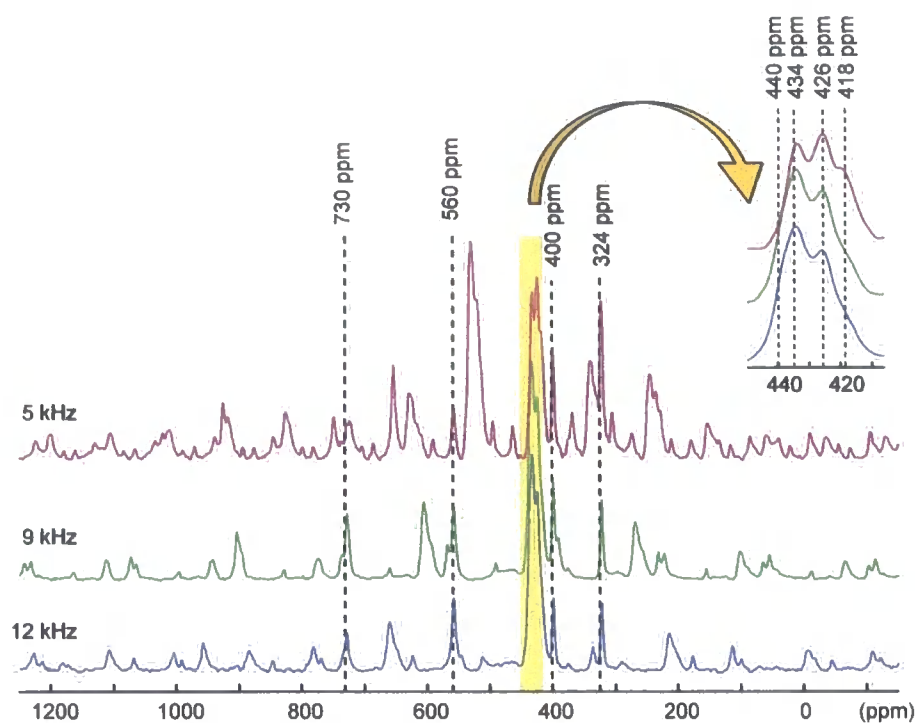
Figure 6.11. ¹⁷O MAS NMR spectra of ZrW_2O_8 recorded at different MAS frequencies. A zoomed region, between ~ 410 and 450 ppm, is shown and it can be seen four sites may be present here, although It is thought that this is actually due to quadrupolar coupling, and only two isotropic sites are present . The peaks at 324 and 400 ppm are due to ZrO_2.

The observed disappearance of the weaker peaks, followed by the shifting and broadening of the stronger peaks with the eventual decrease in width of this peak at a position that is approximately an average of the positions of all the peaks at lower temperature (taking into account the relative intensities) is consistent with complete exchange between all the oxygen sites within the structure. This is surprising, and it clearly does not support the literature speculation regarding the phase transition. One other interesting phenomenon in the spectra is the spectrum recorded at 136°C, which has a sudden loss of signal to noise, for which no explanation is clear. The spectrum was recorded in the same manner as the others, and this loss of signal to noise was seen on both heating and cooling at this temperature. Further investigation would be required to explain what is happening at this temperature.
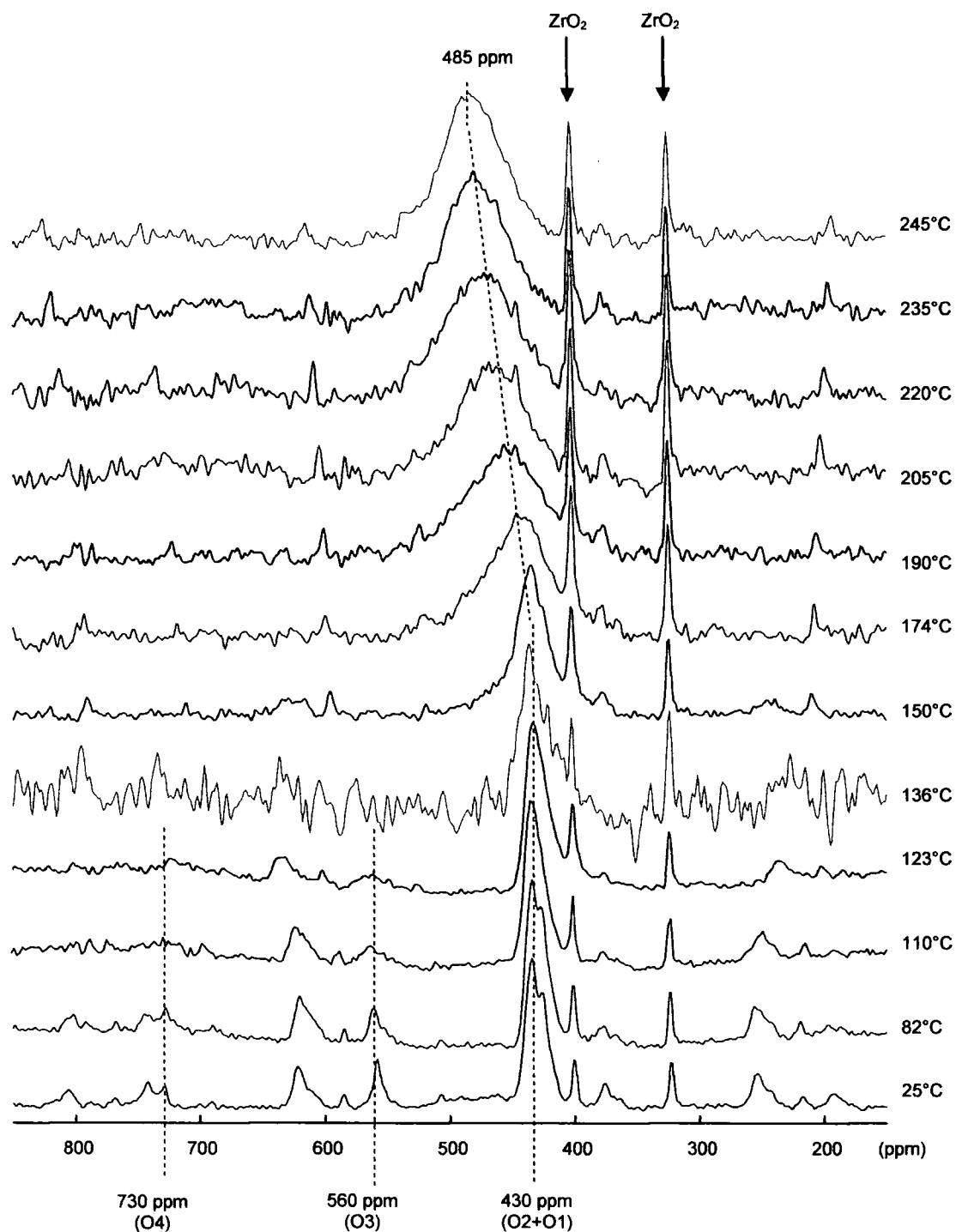
Figure. 6.12. ¹⁷O MAS NMR spectra of ZrW_2O_8 as a function of temperature, recorded with a MAS frequency of approximately 10 kHz. See text for a full disussion. Note the position of the two peaks due to ZrO_2 (highlighted with arrows) do not change with temperature. In this figure the spectra are scaled to the height of the tallest peak.
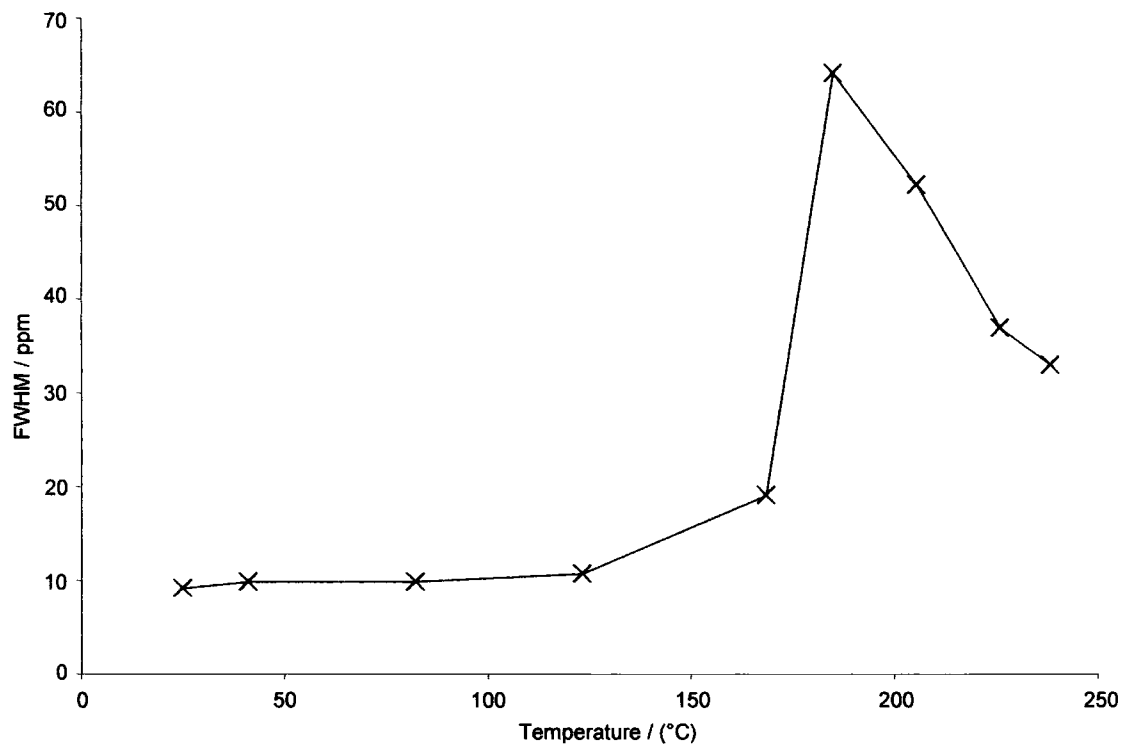
Figure 6.13. A plot of FWHM against temperature for the broad peak in figure 6.10.

6.3 Conclusions

Although the NMR evidence does not appear to support the literature regarding the temperature driven phase transition of ZrW_2O_8 a full picture can not be achieved until higher temperatures can be reached using MAS NMR. In this case the maximum achievable temperature for the VT probe used was, in theory, 299°C. Unfortunately, the difference between the thermocouple reading and 'true temperature' as calculated using the ^{207}Pb thermometer was 54°C. If higher temperatures could be applied, a continued decrease in width of the observed broad ZrW_2O_8 resonance would be expected if a complete oxygen exchange is occurring. Complete oxygen exchange at such low temperatures is somewhat surprising and further experiments will be necessary to completely understand this material. Such studies have not, unfortunately, been possible with the time/equipment constraints of this work, but could include:

(i)   development of samples with higher enrichment levels;

(ii)   NMR study of 100% pure $ZrW_2{}^{17}O_8$;

(iii)   longer VT NMR experiments to gain improved signal:noise;

(iv)   NMR studies over a wider temperature range;

(v)   NMR studies on other members of the family;

(vi) ^{183}W NMR studies.

6.4 Acknowledgement

I would like to acknowledge the work of Simon Allen in the synthesis and X-ray analysis of the samples studied and presented in this chapter. Many hours of work were required in the synthesis of the ^{17}O enriched samples, for which I owe Simon huge thanks.

6.5 References

(1)   Evans, J. S. O.; Mary, T. A.; Vogt, T.; Subramanian, M. A.; Sleight, A. W. *Chem. Mater.* 1996, *8*, 2809 - 2823.

(2)   Mary, T. A.; Evans, J. S. O.; Vogt, T.; Sleight, A. W. *Science* 1996, *272*, 90-92.

(3)   Evans, J. S. O.; David, W. I. F.; Sleight, A. W. *Acta Cryst.* 1999, *B55*, 333 - 340.

(4)   Pryde, A. K. A.; Hammonds, K. D.; Dove, M. T.; Heine, V.; Gale, J. D.; Warren, M. C. *J. Phys.-Condens Matter.* 1996, *8*, 10973-10982.

(5)   Evans, J. S. O. *J. Chem. Soc.-Dalton Trans.* **1999**, 3317-3326.

(6)   Evans, J. S. O.; Hu, Z.; Jorgensen, J. D.; Argyriou, D. N.; Short, S.; Sleight, A. W. *Science* 1997, *275*, 61.

(7)   Jorgensen, J. D.; Hu, Z.; Teslic, S.; Argyriou, D. N.; Short, S.; Evans, J. S. O.; Sleight, A. W. *Phys. Rev. B* 1999, *59*, 215 - 225.

(8)   Evans, J. S. O.; Hanson, P. A.; Ibberson, R. M.; Duan, N.; Kameswari, U.; Sleight, A. W. *J. Am. Chem. Soc.* 2000, *122*, 8694-8699.

(9)   Evans, J. S. O.; Hu, Z.; Jorgensen, J. D.; Argyriou, D. N.; Short, S.; Sleight, A. W. *Science* 1996, *275*, 61-65.

(10)   Mackenzie, K. J. D.; Smith, M. E. *Multinuclear Solid-State NMR of Inorganic Materials*; Pergamon: Oxford, 2002.

(11)   Xu, Z.; Stebbins, J. F. *Solid State Nucl. Mag. Res.* 1998, *11*, 243-251.

(12)   Bastow, T. J.; Smith, M. E.; Whitfield, H. J. *J. Mater. Chem.* 1992, *2*, 989-990.

(13)   Bastow, T. J.; Stuart, S. N. *Chem. Phys.* 1990, *143*, 459-467.

(14)   Locherer, K. R.; Swainson, I. P.; Salje, E. K. H. *J. Phys.- Condens. Matter* 1999, *11*, 6737-6756.

(15)   Woodward, P. M.; Sleight, A. W.; Vogt, T. *J. Solid State Chem.* 1997, *131*, 9-17.

(16)   Vogt, T.; Woodward, P. M.; Hunter, B. A. *J. Solid State Chem.* 1999, *144*, 209-215.

(17)   Bielecki, A.; Burum, D. P. *J. Magn. Res.* 1995, *A116*, 215-220.

(18)   van Gorkom, L. C. M.; Hook, J. M.; Logan, M. B.; Hanna, J. V.; Wasylishen, R. E. *Magn. Reson. Chem.* 1995, *33*, 791-795.

(19)   Takahashi, T.; Kawashima, H.; Sugisawa, H.; Baba, T. *Solid State Nucl. Mag.* 1999, *15*, 119-123.

(20)   Zhao, P. D.; Prasad, S.; Huang, J.; Fitzgerald, J. J.; Shore, J. S. *J. Phys. Chem. B* 1999, *103*, 10617-10626.

Chapter 7

2-[4-(2-hydroxy-ethylamino)-6-phenylamino-

[1,3,5]triazin-2-ylamino]- ethanol –

A Structure Solution from Powder X-Ray Diffraction

7.0 Overview of the Process of Structure Solution from Powder XRD

Structure solution has traditionally been thought of as lying almost solely in the domain of single-crystal X-ray diffraction (XRD). However, in many cases it is not possible to prepare single crystals of sufficient quality for use in single-crystal diffraction studies. In such cases, where the material is of sufficient crystallinity, it is possible to turn to powder XRD to obtain structural information, and in an increasing number of cases it is possible to determine the full structure of a material via this technique.[1,2] The increase in the numbers of structures being solved from powder XRD has come about due to several recent advances, including more accurate powder patterns from laboratory machines, faster computers (allowing more data to be processed), and new strategies for structure solution, namely direct-space approaches.[2] Also there is increasing use of other techniques in conjunction with diffraction data, as has been shown earlier in section 5.1. Excellent reviews, particularly by K. D. M. Harris et al., regarding recent developments in this field can be found in the literature.[1,2]

The procedure for structure solution using powder XRD follows a number of steps, as outlined below.

7.0.1 Sample Preparation and XRD Measurement

Sample preparation and measurement are the first, and perhaps the most important, steps in the process of structure solution. To be able to solve a structure from powder XRD it is important to have a high-quality sample, i.e. one with high purity and high crystallinity, and a

high quality XRD pattern, i.e. very accurate 2θ values and precise relative intensities. As will be discussed in more detail in the next section, high crystallinity is required to give the sharp peaks in the XRD patterns required for accurate 2θ values, while high purity is beneficial as it makes the next step, indexing, a lot easier. The measurement of powder samples for structure solution has often required synchrotron data to be collected for accurate 2θ values and good signal-to-noise, but recent advances in laboratory instrumentation has meant this is no longer the case, although it is still a very useful tool, and it can often be beneficial to employ both data collected on a laboratory instrument and data collected on a synchrotron.

7.0.2 Unit Cell Determination (Indexing)

This is the most difficult step in powder structure solution, and can often be the most time consuming part of the overall process. The positions of the reflections in a powder XRD pattern may readily be predicted from the unit cell of a known structure, so it would be easy to assume that this means a unit cell could be obtained easily, via the reverse process, from a powder XRD pattern. However this is not typically the case. Six unknown parameters (3 cell edges and 3 angles) need to be found, which requires at least six reflections. In practice, however, more reflections than this are required as it is usual that more than one cell could index any six given reflections. Most indexing programs, of which a number are available, require the positions of around 20 reflections to be input, with less than $0.01°$ error in the 2θ value for each reflection. Three of the most widely used indexing programs are ITO,[3] TREOR[4] and DICVOL91,[5] two of which work in reciprocal space (ITO and TREOR) and one of which performs an exhaustive search in real space (DICVOL91). These programs involve relatively complex operations and protocols which will not be discussed here. The important factor in the use of these programs is the interpretation of the results they give, which are given as the number of lines indexed and a figure of merit which is the discrepancy between the observed and calculated Q values, where Q is the square of the distance from the origin to the point for an arbitrary reciprocal lattice of the same size [as that calculated] and the actual average discrepancy.[6] The figure of merit is a valuable tool in indicating which of a range of possible cells are likely to be correct and, in general, figures of merit above 20 are considered to be possible solutions to the indexing problems.

Each of these programs requires the position of around 20 reflections in an input file, all from the phase being studied. This therefore requires a very high level of purity (the aim of almost any synthesis). Indeed, some indexing programs will not be able to give a possible solution even if just one impurity reflection is present in the input file. Unfortunately, until indexing is complete, it is not always possible to tell if any impurities are present. An alternative method to the problem of sample impurity, that of exhaustively searching subsets of reflections, is possible and is described in section 7.1.3. As mentioned earlier, the 2θ position used in the indexing input files must be extremely accurate (within ~0.01° 2θ), a factor which makes indexing an extremely difficult process (N.B. typical random errors in the determination of peak positions are ~0.02°; typical systematic errors due to diffractometer misalignment/sample positioning errors can be 0.05° or larger). Small, but consistent, alterations can be made to a set of 2θ values in an attempt to get correct 2θ positions, but this is not necessarily recommended, as it may be that this will lead to an incorrect solution. Alternatively a standard, such as Si, for which the 2θ values are known accurately, can be added to the sample so that the positions of the sample reflections can be precisely corrected. Another problem encountered in the indexing program is that as d-spacing increases the number of reciprocal lattice points also increases, but as a cubic function. This leads to overlapping of reflections, making it difficult to determine the positions of individual reflections accurately. Also, even if a given solution from indexing is close to the real solution it may not show up in the figure of merit, as is shown in fig. 7.1. This plot shows Q_D and Q_E (Q_A-Q_F, the powder constants, are the reciprocal space equivalents to the six unit cell parameters in normal space) plotted against the figure of merit, and an extremely "spiky" surface is seen. A high figure of merit is only seen on this plot when the correct Q_E is paired with the correct Q_D, highlighting yet another problem encountered when indexing.

ALPHA CU-PHTHALOCYANINE HKL >VVW W/O OOL THETA<17.5 ** M:
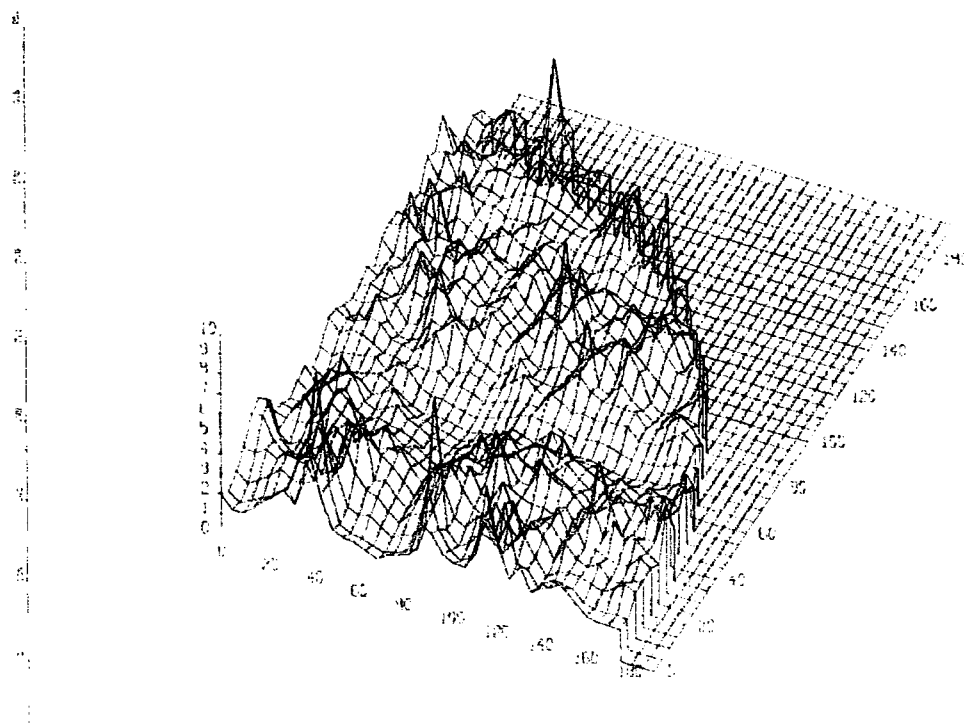
Figure 7.1. A plot of Q_D and Q_E against figure of merit for α-Cu phthalocyanine. This figure has been reproduced from ref. 7.

At the end of the indexing process, programs give an output file of possible solutions, in the form of cell edges and angles, along with figures of merit. The solutions with reasonably high figures of merit can then be used to create a set of reflections, and these can be matched against the experimental data, with this usually being done visually (i.e. overlaying the calculated reflections on the experimental reflections), and from this it can be decided whether to proceed further with a given set of cell parameters.

7.0.3 Space Group Determination

Indexing gives the six cell parameters, but not the space group, which is required to fully define the powder diffraction profile. The space group can be determined by identifying the systematic absences present in the indexed powder pattern. If a space group cannot be uniquely determined it may be necessary to carry out the rest of the structure solution for a number of plausible space groups.

7.0.4 Definition of Powder Diffraction Profile

Once indexing is complete, and the space group determined, the next stage required is frequently the extraction of intensity information from the powder pattern for structure solution. Whilst some approaches model the entire diffraction pattern directly, approaches based on extracted integrated intensities are generally faster. To obtain these, a sophisticated approach is generally adopted, based on the use of a profile-fitting procedure. In this approach the pattern is decomposed using a least squares method. No structural model is used, and the refinement is done using lattice parameters, zero-point error, peak shape parameters, and background terms. The two most commonly used algorithms for this are those of Pawley[8] and Le Bail.[9] The peak shape is dependent on characteristic properties of both the instrument and the sample, with the most commonly used peak shape for laboratory powder XRD being the pseudo-Voigt function,[10] which uses a weighted combination of Gaussian and Lorentzian functions. This process, as in all structure solutions, is an important one, because most methods of structure solution depend of the accurate input of intensity information, which can be difficult for overlapping reflections.[1] This process may also allow the identification of impurities within the powder XRD pattern.

7.0.5 Direct Methods

Direct methods is the classical approach to structure solution, which relies on the extraction of intensity information for individual reflections in the experimental XRD powder pattern. These are then put through one of a number of direct methods programs that use these intensities to 'produce' an electron density map of the unit cell, from which the positions of molecular fragments can be determined. These positions can then be used as the starting point for Rietveld refinements.[11,12] Whilst direct methods remain the technique of choice in the majority of single crystal structure solutions, problems due to the limited information in a powder pattern have led to alternative approaches being researched.

7.0.6 Simulated Annealing

Simulated annealing is a similar process to the Monte Carlo approach to structure solution. In the simulated annealing process a sequence of trial structures is generated, with each structure considered as a potential solution to the diffraction data. Each structure is generated from the previous one by a random displacement of a structural fragment within the unit cell. Once a structure is created, the powder XRD pattern for that structure is calculated and compared to the experimental pattern. The structure is then either accepted or rejected on the basis of the profile R-factor, using an importance sampling algorithm. If we consider each trial structure generated in a sequence of trial structures as N_i for $i = 1, 2, ..., j, j+1, ..., n$, then the trial structure is accepted or rejected by considering $Z = R_{wp}(N_{i,T}) - R_{wp}(N_j)$. If $Z \leq 0$ the trial structure is accepted, whereas if $Z > 0$ the trial structure is accepted with probability $\exp(-Z/S)$ and rejected with probability $[1 - \exp(-Z/S)]$, where S is a scaling factor. For simulated annealing S is decreased systematically according to either an annealing schedule or a temperature reduction procedure, while in the Monte Carlo approach S may be fixed or varied manually. This difference, in the way S is varied, is the fundamental difference between the simulated annealing and Monte Carlo approaches. The outlined procedure is repeated to generate a large number (hundreds of thousands) of structures, until the best solution is found. In order to reduce the possibility of finding a local minimum, the process can be repeated with the initial starting point being altered; and if the structures from several runs match, it is likely that the global minimum has been found.

This process gives a good starting model for the actual structure, but further refinements must be carried out to determine the final structure. Simulated annealing is especially useful in the case of organic compounds, where a relatively large amount of information about the structure is usually already known, such as the atoms present and how they are bonded to each other.

7.0.7 Rietveld Refinement[11,12]

Rietveld refinement is a process in which all points of the experimental and calculated diffraction pattern are compared. Rietveld refinement allows selected parameters to be refined using least squares methods in order to obtain an optimal fit. The goodness of fit is commonly judged via

the weight profile figure of merit, R_{wp}. A number of programs are available for this process, in this work the GSAS[13] package was used.

7.1 Structure Solution of 2-[4-(2-hydroxy-ethylamino)-6-phenylamino-[1,3,5]triazin-2-ylamino]-ethanol (HEB2)

7.1.1 Why Study HEB2?

HEB2 (fig. 7.2) was studied by Birkett[14] as part of an investigation of commercial ink-jet-dyes. Dyes are materials for which a number of properties determine their effectiveness, including lightfastness, wetfastness and brightness. As chemical properties are closely related to physical properties, understanding the chemical factors that affect the physical factors would be of great benefit for the manufacture of dyes.
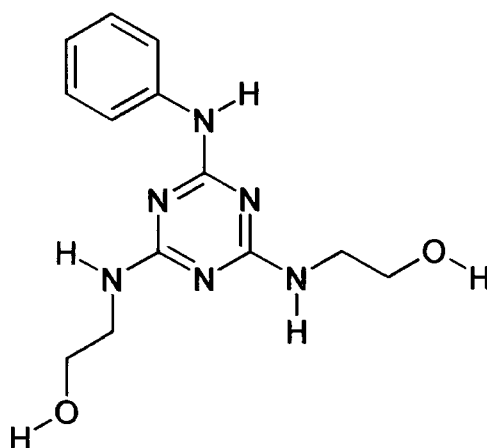
Figure 7.2. The HEB2 molecule.

In this study three model 2,4,6-tris-(amino)-1,3,5-triazine compounds related to a commercial dye, previously reported,[14-16] were synthesised, by Birkett, in a bid to understand the properties of the commercial dye. These were primarily studied via NMR, which is reported elsewhere.[14] The three synthesised compounds were initially examined by powder XRD as a check for crystallinity and their degree of purity (information that is often hard to access by solid-state NMR), via comparison to the patterns of potential impurities, such as the starting materials, using the available databases. From this initial study it became apparent that for one of these three compounds, HEB2, it might be possible to index the powder data, and hence solve its structure. A search of the Cambridge Structural Database (CSD) was undertaken to see if the

structure of this compound had previously been determined. As this proved not to be the case, the study presented here was undertaken.

7.1.2 Powder XRD Measurements

Powder XRD data were initially collected on a Bruker D5000 in reflection mode, as shown in fig. 7.3, and from this it was apparent that it might be possible to index the pattern, as the sample is clearly highly crystalline, and a number of sharp reflections are apparent. Further powder XRD patterns were then collected on a Bruker D8, which is a more modern instrument, and one which, in the case of the instruments used for this study, gives more accurate 2θ values, and has a number of possible arrangements under which to collect powder XRD patterns.
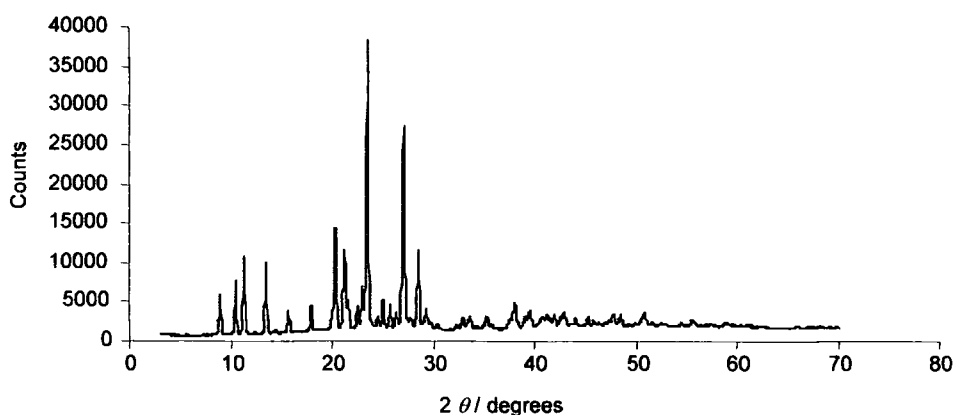
Figure 7.3. Initial powder XRD pattern of HEB2, recorded on a Bruker D5000. Data set collected in reflection mode over 18 hours.

Data were collected on the D8 in both reflection mode (fig. 7.4) and capillary mode (fig. 7.5), the latter being useful as it removes preferred orientation effects that may be present in samples mounted on flat plates (see section 2.2.3).
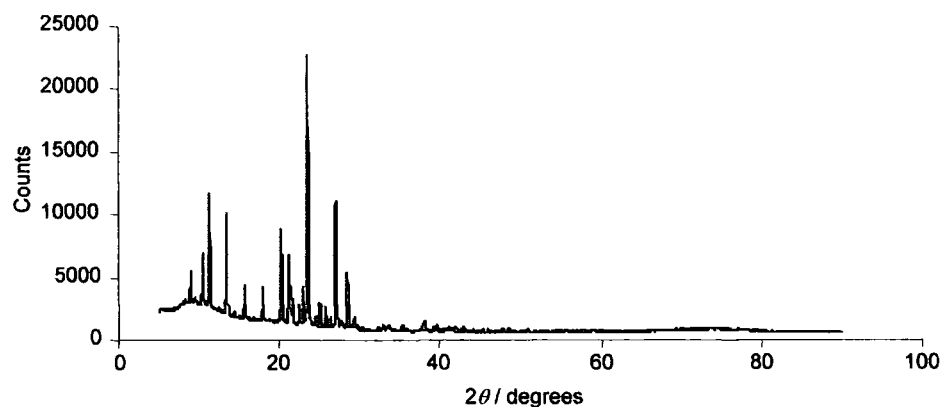
Figure 7.4. Powder XRD pattern of HEB2, recorded on a Bruker D8. Data set collected in reflection mode over 19 hours.

Capillary mode data were collected in seven 12 hour data sets and were summed to give a full data set (which was used for indexing purposes) as this gives a better signal-to-noise ratio. Data were also collected from a synchrotron source (beamline x7a of the National Synchrotron Light Source at Brookhaven National Laboratory (USA), at a wavelength of 0.7452 Å, and from 3° to 40° 2θ), with the sample mounted in a capillary of 0.5 mm diameter (fig. 7.6).
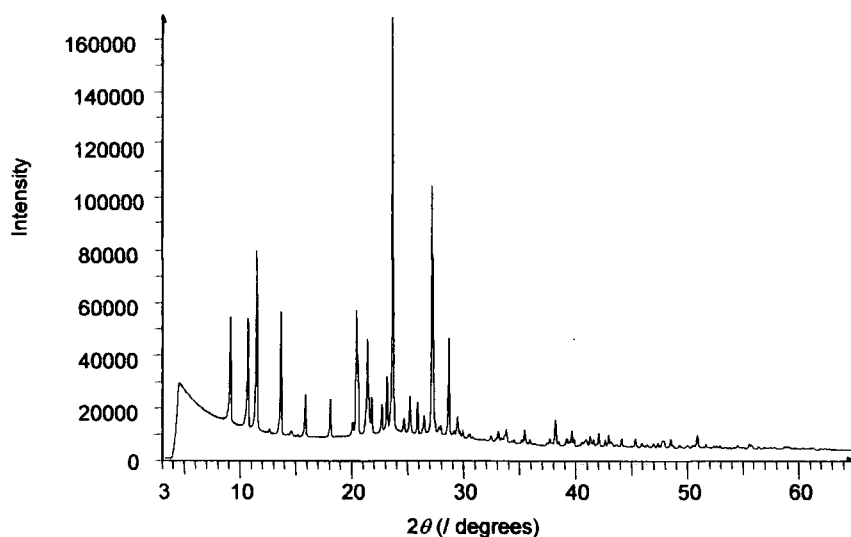
Figure 7.5. Powder XRD pattern of HEB2 collected in capillary mode (data collected in 7 data sets on Bruker D8 over 84 hours with the data sets being added together).
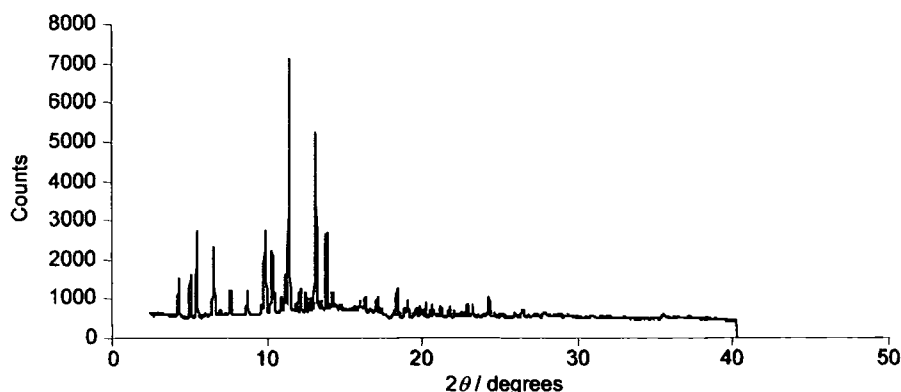
Figure 7.6. Synchrotron data of HEB2, collected on beamline x7a of the National Synchrotron Light Source at Brookhaven National Laboratory at a wavelength of 0.7452 Å.

7.1.3 Indexing

As discussed above, a number of indexing programs are available, and the best choice for a given data set is not always obvious. In this study, the ITO program[3] was used, and a subroutine, named multivisser[17] (Visser being the author of the ITO program), was used to reduce the time of creating input files. This subroutine allows the positions of up to 35 reflections to be input. In the input file these reflections are marked as either being definitely from the phase in question, or as perhaps being from the phase. The subroutine then creates all the possible ITO input files, which include all the reflections marked as definitely belonging to the phase plus a number of the other reflections, so that the input file contains the position of 20 reflections in total. If, as in this case, 31 reflections are in the multivisser input file, with 15 marked as definitely belonging to the phase, being studied and 16 marked as perhaps belonging to this phase, then 4367 ITO input files are created. Each of these files will contain the 15 definite reflections and 5 of the possible reflections, with every possible combination of the 16 possible reflections being trialled. Multivisser then allows all of these to be input into the ITO program and the user gets an output file containing all the cells generated along with the respective figure of merit. This process means only one input automates the otherwise laborious task of file generation, which greatly reduces the time required for indexing. However, even with 4367 combinations of reflections being trialled it is not necessarily true that a correct set of unit cell values will be obtained, and this process may need to be repeated a number of times, and even then it may be that a correct unit cell is not found. In the case of HEB2 a large

number of cells were generated with figures of merit in excess of 80, the highest being 96.2. This had the following cell parameters:

$$a = 9.003 \text{ Å}$$
$$b = 9.893 \text{ Å}$$
$$c = 8.343 \text{ Å}$$
$$\alpha = 91.484°$$
$$\beta = 110.479°$$
$$\gamma = 87.032°$$

which is a triclinic cell, giving the possibility of only two space groups; $P1$ and $P\bar{1}$. From the NMR study of Birkett[14] it was known one molecule was present in the asymmetric unit, and, using density calculation, it was possible to show that $P\bar{1}$ was the actual space group, with two molecules being present in the unit cell. The cell generated by this process accounts for almost all of the reflections seen in the experimental powder pattern, as can be seen from fig. 7.7.

7.1.4 Pawley Fitting

Using the cell parameters above, a Pawley fit[8] was carried out using the Topas program[18] and is shown in fig. 7.7. It can be seen that this cell successfully predicts all the observed reflections. This Pawley fit was carried out using 12 background terms, and a pseudo-Voigt peak shape.
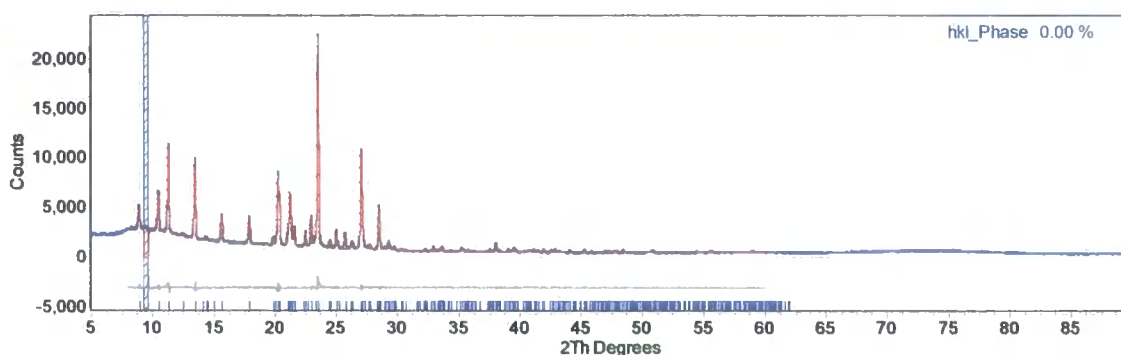
Figure 7.7. Pawley fit of the powder XRD pattern collected on a Bruker D8. The region from 9.25° to 9.65° 2θ is excluded from the Pawley fit. The experimental data are shown in blue, while the Pawley fit is in red, and tic marks occur along the bottom showing the positions of expected reflections. A difference curve is also shown (grey).

7.1.5 Simulated Annealing

Simulated annealing was carried out in this study based on integrated intensity data, extracted and analysed within the DASH program (alpha test version a1).[19] Within the HEB2 structure there are six degrees of freedom, so a large number of solutions are possible. To reduce the computational running time of the simulated annealing process only data from 8° to 40° 2θ were used. The best fit obtained is shown in fig. 7.8.
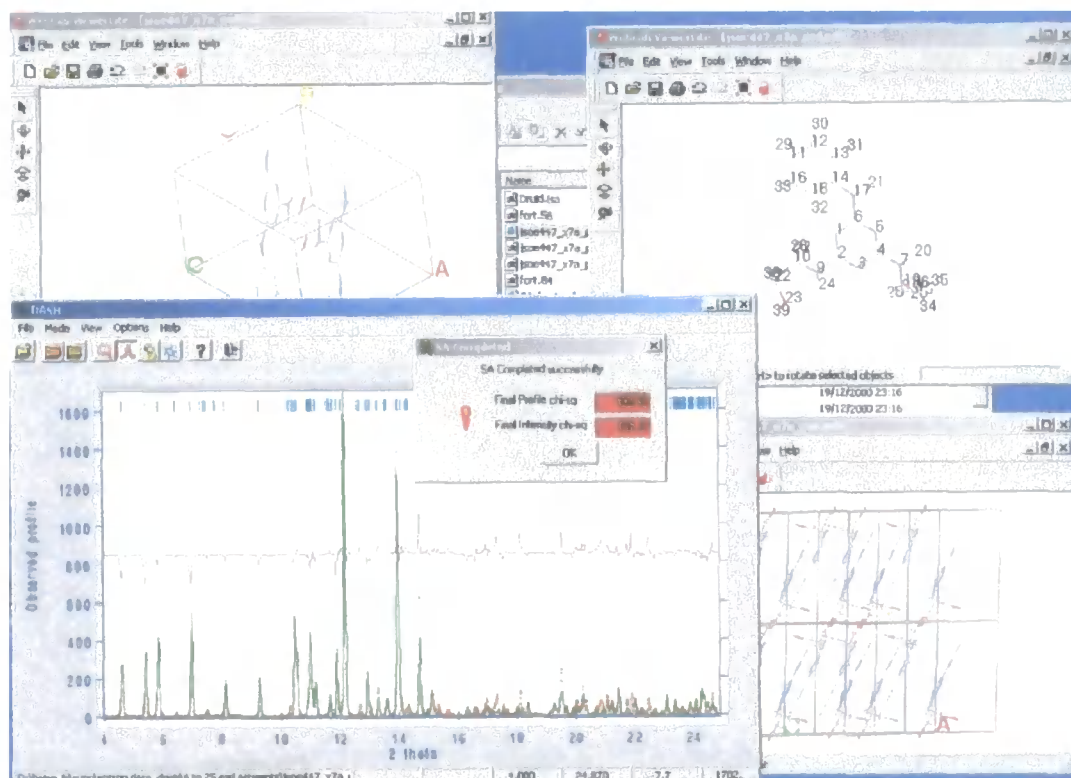
Figure 7.8. DASH fit of the experimental powder XRD pattern of HEB2 after simulated annealing, with the structure which gives this best fit shown. The experimental data are shown by red dots, the powder XRD pattern that would be generated by the best fit structure is shown by the green line, and the difference curve is shown in purple. Other plots of the screen dump give views of the structure.

This structure is best viewed as a 'rough' solution, and further Rietveld refinements were required to find the final solution.

7.1.6 Rietveld Refinement

As can be seen from fig. 7.8, the powder XRD pattern of the best solution from simulated annealing, although giving a reasonable match with the experimental data, still needs further structural refinements. Due to the complexity of the structure, with all atoms being inequivalent

and no symmetry elements being present, searches of the CSD were undertaken to find similar structures so that chemically plausible restraints could be applied during the refinements. Searches were done for bond angles of rings similar to the triazine ring of HEB2 (fig. 7.9), with an example result shown in fig. 7.11 for an N(1)–C(6)–N(5) bond angle.
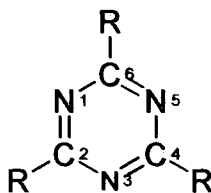
Figure 7.9. Numbering scheme for triazine ring of HEB2.

Only structures with side-chains on the carbon atoms were accepted for this analysis. Those with side-chains on the nitrogen atoms were rejected, and structures were also rejected if a charge was contained close to the ring.

The range of angles for the six bonds in the ring were found to be:

N(1)–C(6)–N(5): 116.2° - 129.7°

C(6)–N(5)–C(4): 110.1° - 121.4°

N(5)–C(4)–N(3): 119.0° - 131.3°

C(4)–N(3)–C(2): 106.8° - 123.3°

N(3)–C(2)–N(1): 113.5° - 132.1°

C(2)–N(1)–C(6): 110.3° - 121.9°

Using this information the ring angles were therefore restrained (a factor which is controlled by a weighting factor in the Rietveld refinement) with a weight that gave angles in the range:

N–C–N bonds: 126° ± 2°

C–N–C bonds: 114° ± 2°
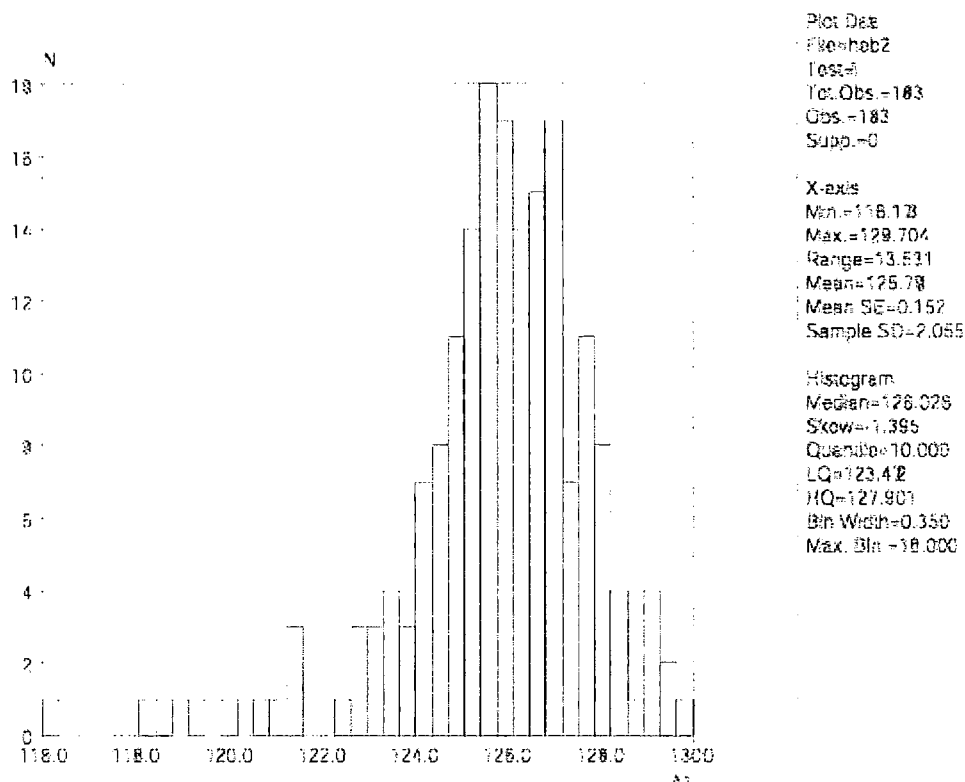
Figure 7.10. Plot of distribution of N(1)–C(6)–N(5) bond angles in C₃N₃ rings in similar environments to the ring in HEB2. The average bond angle for this bond is 125.7°.

Restraints were also applied to the planarity of the phenyl ring so that it was flat, and individual bond distances were also restrained. The higher the weighting, the more rigidly the restraint is applied during Rietveld refinement. Initial Rietveld refinements were undertaken without hydrogen atoms as the diffraction data are relatively insensitive to their positions. Refinements followed a relatively standard protocol in which cell parameters (6), zero point, scale factor, background coefficients (15) and profile coefficients were refined initially (28 "histogram" variables) followed by restrained atomic coordinates (63 variables). Once a reasonable fit to the experimental data had been achieved the hydrogen atoms were introduced. In the majority of cases this could be performed from purely geometrical considerations (ring H's, CH_2's etc.). For H191 and H211, where there is a free torsional angle, the ideal hydrogen coordinates were determined by energy minimization using the Dreiding Force Field and Gasteiger charges, within the Cerius^2 software suite, by Dr Julian Cherryman. For final cycles of refinement, hydrogen coordinates were constrained to refine with the C/N/O atom to which they were attached, and a single overall temperature factor applied, while the weightings of the bond angle and bond length restraints were reduced. Final agreement factors of wR_p = 2.73 and $R(F^2)$ =

9.7% were obtained. Details of the refinement are given in table 7.1, with bond lengths shown in fig. 7.11, final coordinates in table 7.2 and bond angles in table 7.3. The experimental X-ray pattern, the theoretical X-ray pattern from the structure, and difference curve are shown in fig. 7.12. A .cif file for the HEB2 structure is given in Appendix 5.

Parameter	Value	Parameter	Value
λ	0.7452 Å	c	8.34487(28) Å
2θ range	3° to 40°	α	91.5224(21)
zero point	0.006°	β	110.5189(21)
space group	$P\bar{1}$	γ	87.0330(24)
a	9.00468(33) Å	wR_p	2.73%
b	9.8930(4) Å	$R(F^2)$	9.71%
		number of parameter refined	92 (63 xyz parameters; 1 uiso; 28 histogram variables)

Table 7.1. Parameter values for structure solution of HEB2, using synchrotron data.

Figure 7.11. Numbering scheme and bond lengths of HEB2.

165

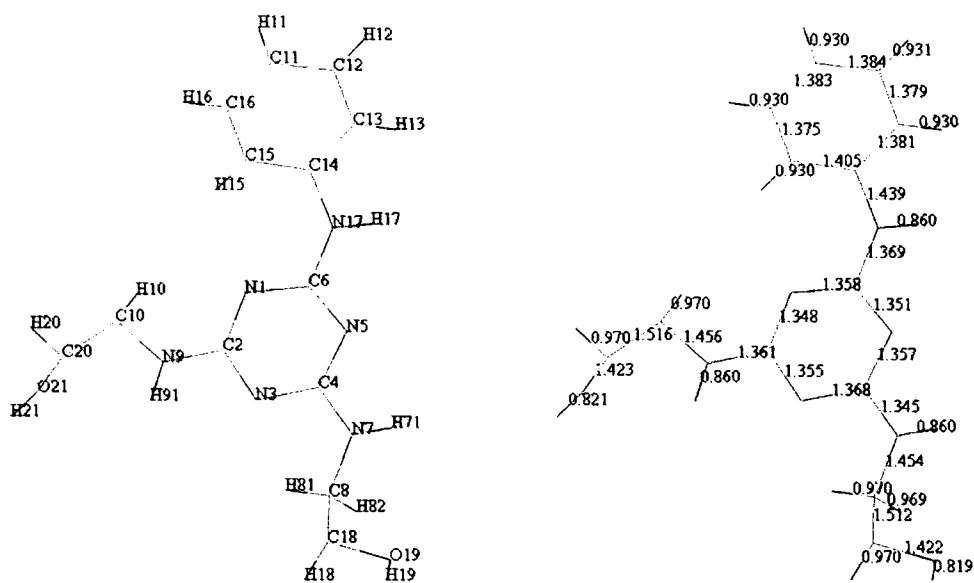| Atom	x-coordinate	y-coordinate	z-coordinate	Uiso
N1	0.4904(6)	0.5866(8)	0.6772(6)	-0.00246
C2	0.4369(9)	0.6964(7)	0.5774(6)	-0.00246
N3	0.2865(9)	0.7245(7)	0.4705(11)	-0.00246
C4	0.1845(8)	0.6246(7)	0.4628(10)	-0.00246
N5	0.2266(8)	0.50982(12)	0.5566(11)	-0.00246
C6	0.3768(8)	0.4990(8)	0.6694(12)	-0.00246
N7	0.0380(9)	0.6439(8)	0.3460(10)	-0.00246
C8	-0.0215(14)	0.7554(9)	0.2271(11)	-0.00246
N9	0.5372(10)	0.8003(8)	0.6126(12)	-0.00246
C10	0.7016(11)	0.8075(10)	0.7263(14)	-0.00246
C11	0.8383(10)	0.2528(9)	1.1661(10)	-0.00246
C12	0.7014(10)	0.1813(8)	1.1207(11)	-0.00246
C13	0.5689(9)	0.2228(8)	0.9849(11)	-0.00246
C14	0.5748(9)	0.3358(9)	0.8941(10)	-0.00246
C15	0.7163(11)	0.4047(8)	0.9368(12)	-0.00246
C16	0.8472(9)	0.3647(8)	1.0744(12)	-0.00246
N17	0.4304(9)	0.3840(8)	0.7639(10)	-0.00246
C18	-0.0788(11)	0.8736(10)	0.3119(14)	-0.00246
O19	-0.2212(9)	0.8439(8)	0.3384(10)	-0.00246
C20	0.7541(13)	0.9517(10)	0.7635(11)	-0.00246
O21	0.7308(9)	0.9984(8)	0.5963(10)	-0.00246
H111	0.9258(10)	0.2252(9)	1.2600(10)	-0.00246
H121	0.6985(10)	0.1044(8)	1.1811(11)	-0.00246
H131	0.4766(9)	0.1750(8)	0.9543(11)	-0.00246
H151	0.7218(11)	0.4776(8)	0.8713(12)	-0.00246
H161	0.9397(9)	0.4124(8)	1.1050(12)	-0.00246
H81	0.0634(14)	0.7832(9)	0.1906(11)	-0.00246
H82	-0.1087(14)	0.7254(9)	0.1284(11)	-0.00246
H101	0.7133(11)	0.7626(10)	0.8322(14)	-0.00246
H102	0.7693(11)	0.7609(10)	0.6721(14)	-0.00246
H181	-0.1003(11)	0.9512(10)	0.2371(14)	-0.00246
H182	0.0033(11)	0.8944(10)	0.4200(14)	-0.00246
H201	0.8654(13)	0.9518(10)	0.8350(11)	-0.00246
H202	0.6915(13)	1.0038(10)	0.8193(11)	-0.00246
H211	0.7437(9)	1.0801(8)	0.6069(10)	-0.00246
H191	-0.2377(9)	0.9050(8)	0.3989(10)	-0.00246
H91	0.4975(10)	0.8727(8)	0.5555(12)	-0.00246
H171	0.3585(9)	0.3252(8)	0.7415(10)	-0.00246
H71	-0.0284(9)	0.5832(8)	0.3415(10)	-0.00246

Table 7.2. Atomic coordinates of HEB2 in the asymmetric unit along with the Uiso value. We note that isotropic temperature factors have refined to slightly negative values. This is presumably caused by a small systematic error such as absorption or the LP correction used for the data. We note that absolute values of temperature factors are hard to obtain from routine powder work, but that the structure give a Uiso of 0.03 (wR_p = 3.53, $R(F^2)$ =5.2 %) when refined against laboratory data.

Group	Atoms	Angle (errors)	Group	Atoms	Angle (errors)
triazine- ring	C2_N1_C6	114.4(5)	other angles (excluding C–H bonds)	C13_C14_N17	117.9(8)
	N1_C2_N3	127.0(6)		C15_C14_N17	122.0(9)
	C2_N3_C4	113.6(6)		C6_N17_C14	136.9(9)
	N3_C4_N5	124.0(6)		C6_N17_H171	112.1(4)
	C4_N5_C6	116.7(6)		C14_N17_H171	111.1(6)
	N1_C6_N5	123.7(6)		N1_C6_N17	115.1(7)
				N5_C6_N17	120.3(4)
				N3_C2_N9	116.2(7)
phenyl group	C12_C11_C16	121.1(7)		N1_C2_N9	115.5(8)
	C11_C12_C13	120.3(7)		N5_C4_N7	121.0(8)
	C12_C13_C14	119.4(7)		N3_C4_N7	114.9(7)
	C13_C14_C15	119.9(6)		C4_N7_C8	127.7(10)
	C14_C15_C16	120.5(7)		N7_C8_C18	110.4(8)
	C11_C16_C15	118.7(7)		C8_C18_O19	110.8(9)
				C2_N9_C10	130.7(9)
				N9_C10_C20	112.7(8)
hydroxyl groups (calculated)	C18_O19_H191	106.2(5)		C10_C20_O21	101.3(8)
	C20_O21_H211	105.5(5)			

Table 7.3. A list of the bond angles in HEB2, excluding X–C–H bond angles (these can be found using the coordinates given in Appendix 5).
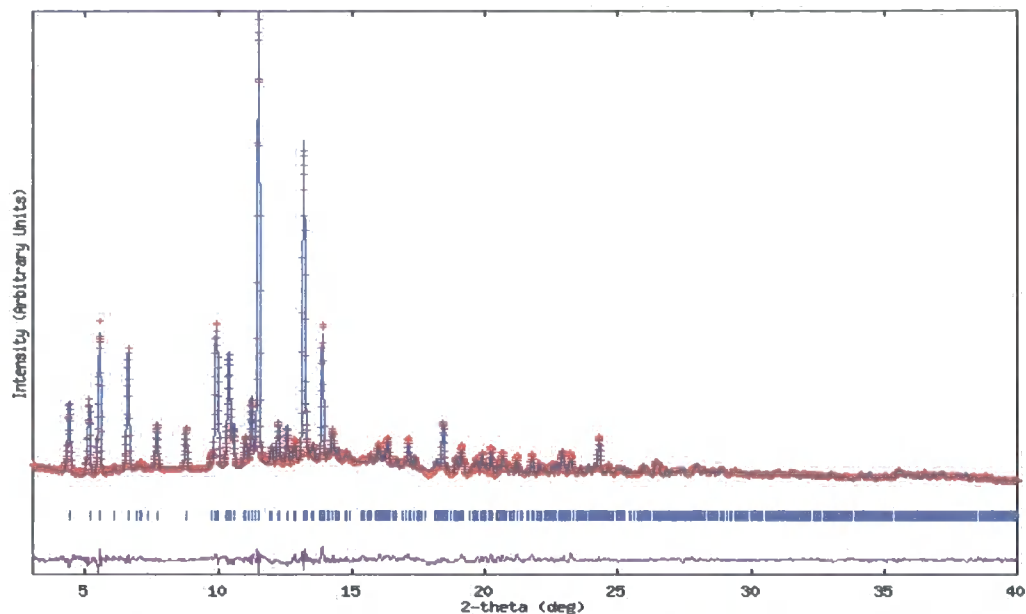
Figure 7.12. Powder XRD pattern from the structure of HEB2 as determined from this study. The experimental X-ray pattern (red) is shown, along with the calculated pattern (blue) and with the difference curve (purple).
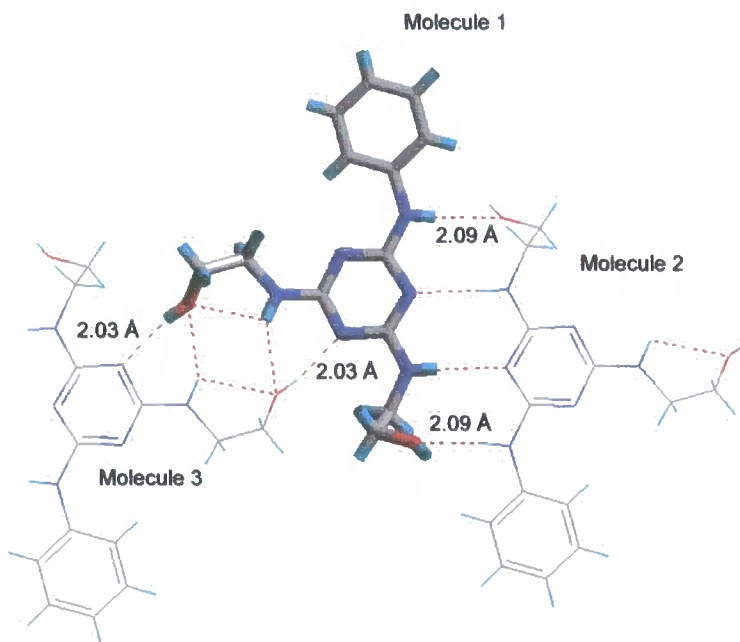
Figure 7.13. Hydrogen bonding network of HEB2, as described in the text, where molecule 1 and molecule 2 form a dimer, and molecule 3 is one half of a second dimer.
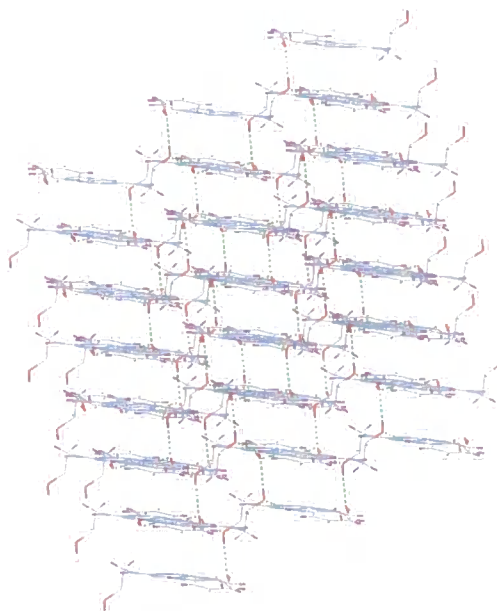
Figure 7.14. Packing of the HEB2 structure with layers being interconnected by a series of O–H hydrogen bonds.

The two rings in the HEB2 structure are essentially coplanar and, as can be seen from fig. 7.13, HEB2 has a rather complex hydrogen-bonding network (table 7.4 gives the hydrogen bond distances), with a prominent dimer motif in which two molecules link through two O···H–N and two N···H–N hydrogen-bonds. These dimers are linked to other dimers through one O···H–N and one N···H–O hydrogen-bond at each end, with the dimers forming 'step-like' planes of molecules. It can also be seen from fig. 7.13 that an internal O···H–N hydrogen bond exists on one of the hydroxy-ethylamino side-chains, with the oxygen and hydrogen atoms involved also forming hydrogen bonds with the same part of a second molecule in the structure, which accounts for the conformation of this side chains. Fig. 7.14 shows that the layers formed by the hydrogen bonded dimers are themselves connected by a series of O···H–O hydrogen bonds to build up a 3-D network.

	Hydrogen bond	D-H···A / Å	D···A / Å	DHA angle / °
Intra-dimer (mol1 and mol2)	$N^{17}H\cdots O^{19}$	2.09	2.93	165.9
	$N^{7}H\cdots N^{5}$	2.46	3.23	150.5
Inter-dimer (mol1 and mol3)	$O^{21}H\cdots N^{3}$	2.03	2.80	155.8
	$N^{9}H\cdots O^{21}$	2.33	3.09	147.4
3D chain	$O^{19}H\cdots O^{21}$	1.97	2.75	160.1
Intramolecular	$N^{9}H\cdots O^{21}$	2.41	2.73	102.1

Table 7.4. Hydrogen bonding in the HEB2 crystal structure, where D is the donor atom and A the acceptor atom of the hydrogen bond.

It is clear that the O–H groups, and hence the hydroxy-ethylamino side-chains, are an integral part of the hydrogen bonding network, and this accounts for the different conformations seen for the side-chains (fig. 7.15).
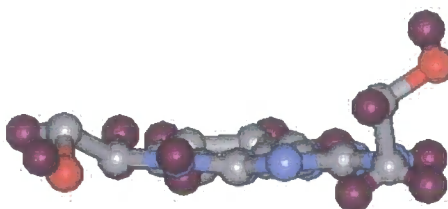
Figure 7.15. Side-view of HEB2 showing the different conformations of the two hydroxy-ethylamino side-chains. In this view O^{19} is sits above the plane.

The dihedral angles of these two side-chains, $C^4N^7C^8C^{18}$ and $C^2N^9C^{10}C^{20}$, are -85.2° and -164.4° respectively.

7.2 $^{n}Bu_2SnF_2$ – an example of a structure that could not be solved

$^{n}Bu_2SnF_2$ was studied as part of a solid-state NMR investigation by Cherryman,[20] into this and related compounds. As in the case of HEB2, a good powder XRD pattern was obtained, however, here it was not possible to solve the structure by powder methods. To assist the indexing process a Si standard was added to aid indexing (fig. 7.16). Data were obtained in transmission mode as in reflection mode significant preferred orientation effects were seen (fig.7.17). The 2θ values for the Si reflections are accurately known, so the presence of Si allows the 2θ values for $^{n}Bu_2SnF_2$ to be obtained free from systematic errors. It is clear from the powder XRD pattern that the sample is highly crystalline and that more than 20 reflections are available for use in the indexing process. Multivisser[17] was again used in this case, and a number of different combinations of reflections were put into input files, so that tens of thousands of sets of 20 reflections were analysed by the ITO[3] indexing program. From this process only a few possible solutions were obtained that gave figures of merit above 20. The Treor and Dicvol91 indexing programs were also used in an attempt to index the $^{n}Bu_2SnF_2$ pattern, but the possible solutions these gave had lower figures of merit (all lower than 20) than those obtained from ITO.
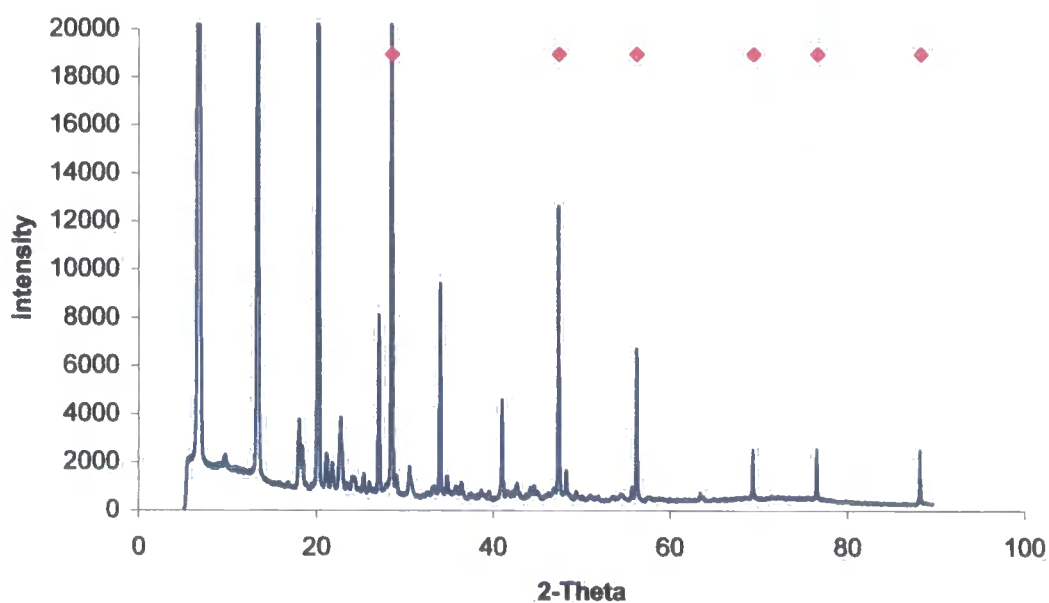
Figure 7.16. The powder XRD pattern of $^{n}Bu_2SnF_2$, using transmission mode, with Si (a = 5.430825Å) added as a standard (peaks shown by the pink markers). This has been expanded vertically so detail can be seen.
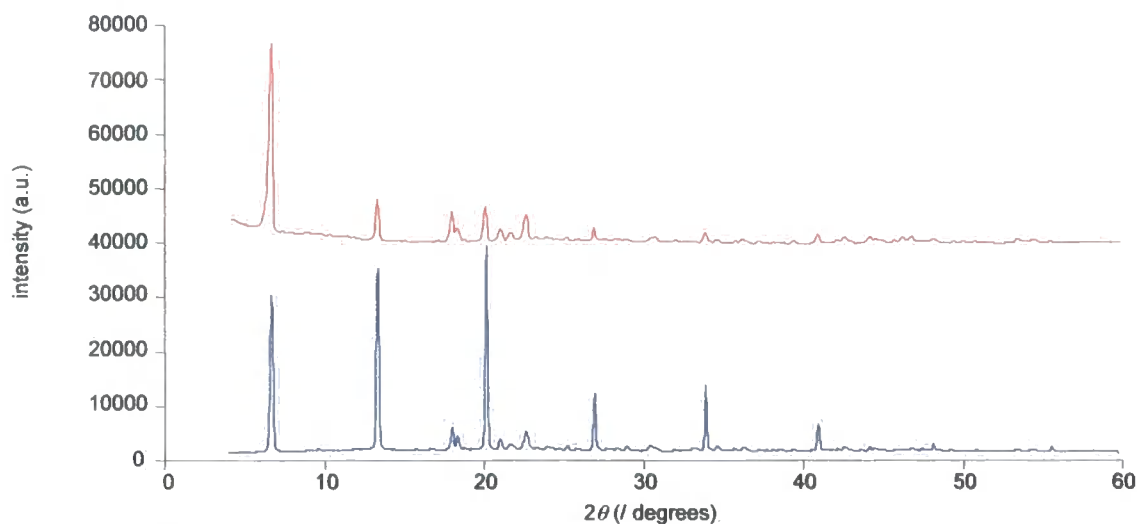
Figure 7.17. Powder XRD patterns of $^nBu_2SnF_2$ in transmission (red) and reflection (blue) modes. It can be seen that severe preferred orientation effects are seen in the reflection mode pattern, with the intensities of one set of reflections significantly exaggerated.

The highest figure of merit obtained from the indexing process was 35.8, but by comparing the calculated reflections from these unit cell parameters with the experimental data, it appeared this was not the correct solution, as can be seen in fig. 7.18. Other possible solutions were also looked at in this manner, but it appeared none was correct. It was believed this may have been due to impurities present in the sample, so a second sample was obtained. Indexing of this new sample generated a highest figure of merit of 48.6, but again this was seen to correspond to an incorrect cell, and none of the possible solutions with reasonable figures of merit described the observed peak positions adequately. This case provides a good example of a material, that, despite being highly crystalline, giving a good powder XRD pattern, and having 2θ values accurately determined using a Si internal standard, still cannot be successfully indexed. This structure can therefore not be determined. This shows the difficulty posed in the process of structure solution from powder XRD, in which many weeks of work on what, initially would appear to be a very good case for structure solution, can turn out to be fruitless.
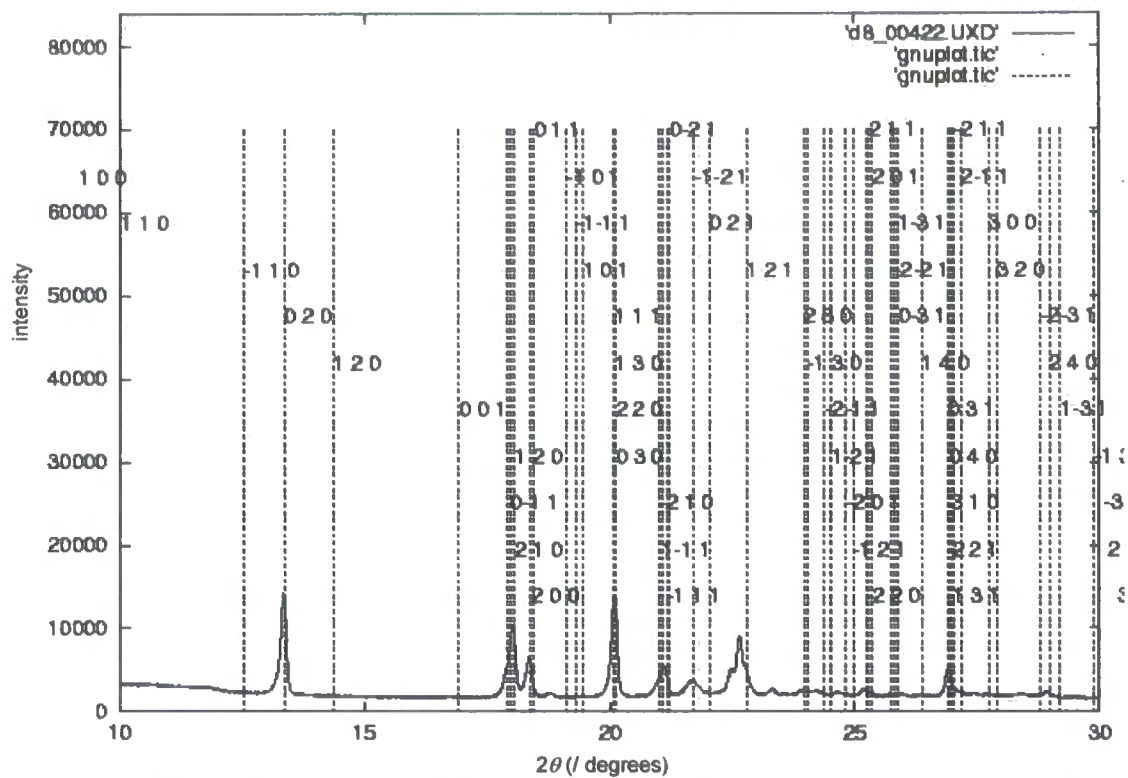
Figure 7.18. Calculated reflections (dashed vertical lines) for the cell which gave the highest figure of merit for $^nBu_2SnF_2$ when indexing with the ITO program with the experimental powder XRD pattern from 10-30° 2θ. It can be seen that some of the observed reflections are not represented by the calculated positions.

7.3 Conclusions

The process of structure solution from powder XRD is a difficult one that often takes a long time, even when it is possible to obtain a solution. Many factors can cause the initial stage of indexing to prove impossible, and even if a cell can be found subsequent steps in the process of the space group assignment/structure solution/refinement may fail. In fact, it may be that for every structure successfully solved by this method, a failed attempt or an incorrect structure exists for another structure. This study has shown both cases, and here the system which, at first appearance, looked to be the more likely to lead to a successful structure solution was actually the system for which this was not possible. At the time the HEB2 work was carried out, this was one of the more complex systems to have been solved using the method outlined, although since that time the procedure has become more commonplace.

7.4 References

(1)   Harris, K. D. M.; Tremayne, M. *Chem. Mater.* 1996, **8**, 2554-2570.

(2)   Harris, K. D. M.; Tremayne, M.; Kariuki, B. M. *Angew. Chem. Int. Ed.* 2001, **40**,1626-1651

(3)   Visser, J. W. *J. Appl. Cryst* 1969, **2**, 89 - 95.

(4)   Werner, P.-E.; Eriksson, L.; Westdahl, M. *J. Appl. Cryst.* 1985, **18**, 367-370.

(5)   Boultif, A.; Louer, D. *J. Appl. Cryst.* 1991, **24**, 987 - 993.

(6)   Wolff, P. M. d. *J. Appl. Cryst.* 1968, **1**, 108 -133.

(7)   Shirley, R., *Seventh European Powder Diffraction Conference (EPDIC-7)*: Barcelona, Spain, 2000.

(8)   Pawley, G. S. *J. Appl. Cryst.* 1981, **14**, 357-361.

(9)   Le Bail, A.; Duroy, H.; Forquet, J. L. *Mater. Res. Bull.* 1988, **23**, 447.

(10)   Young, R. A.; Wiles, D. B. *J. Appl. Cryst.* 1982, **15**, 430.

(11)   Rietveld, H. M. *J. Appl. Cryst.* 1969, **2**, 65-71.

(12)   Young, E. R. A. *The Rietveld Method*; Oxford Science Publications: Oxford, 1996.

(13)   Larson, A. C.; Dreele, R. B. V.; Los Alamos Internal Report LA-UR-86-748, 1994.

(14)   Birkett, H. E., PhD Thesis, *Chemistry Department*; University of Durham: Durham, 2000.

(15)   Birkett, H. E.; Harris, R. K.; Hodgkinson, P.; Carr, K.; Charlton, M. H.; Cherryman, J. C.; Chippendale, A. M.; Glover, R. P. *Magn. Reson. Chem.* 2000, **38**, 504-511.

(16)   Birkett, H. E.; Cherryman, J. C.; Chippendale, A. M.; Hazendonk, P.; Harris, R. K. *J. Mol. Struct.* 2002, **602**, 59-70.

(17)   Evans, J. S. O.: Durham, 1999.

(18)   Bruker AXS; v2.0 ed.: Karlsruhe, Germany, 2000.

(19)   David, W. I. F.; Shankland, K. In; Alpha test version a1; Cambridge Crystallographic Data Centre: Cambridge, 2000.

(20)   Cherryman, J., PhD Thesis, *Department of Chemistry*; University of Durham: Durham, 1998.

Chapter 8

Conclusion

A number of interesting and complex materials have been investigated in this study, and a range of techniques have been utilised. In each of the studies the combined technique approach has been used with great success, and in the case of the AM_2O_7 materials this has given a new approach for studying their structures. The advantages of a multi-technique approach were best seen in the case of this family, where different techniques worked in a complementary fashion to one another. This is perhaps best likened to a jigsaw, with the information obtained from any given method being the individual pieces of the jigsaw, and it only being when these pieces are combined that the whole picture can be seen. In the case of ZrP_2O_7 this has led to one of the biggest structures to date to be solved from powder XRD techniques. For other materials, such as SnP_2O_7 and PbP_2O_7 big advances have been made in the understanding of their room temperature structures, and it has been shown that the general picture presented in most of the literature regarding the structures of AM_2O_7 is considerably over simplified. Each member of the family must be explored individually without any preconceived ideas to understand its true structure.

For ZrW_2O_8, variable-temperature MAS NMR was the main technique employed here, but this work has been done as part of a larger study that has mainly involved extensive variable-temperature diffraction studies that are presented elsewhere. This work has shown that a complete exchange of oxygen atoms may be occurring at this transition which occurs at 450 K. This is in contrast to the proposed model in the literature.

The section on structure solution of HEB2 was separate to the studies of the negative thermal expansion materials, but employed MAS NMR to tell us there was only one molecule in the asymmetric unit and powder XRD. This allowed a complete structure solution for the compound. This was one of the more complex systems to be solved with the methods used at the time of solution. For another material, $^nBu_2SnF_2$, similar methodologies were applied but structure solution proved not to be possible.

So, to conclude, a number of areas of study have been covered in this thesis, and the strengths of a multi-technique approach have been illustrated.

Appendix 1

Temperature calibration curve for variable temperature NMR experiments on the Bruker DSX 400, calculated using the ^{207}Pb thermometer.
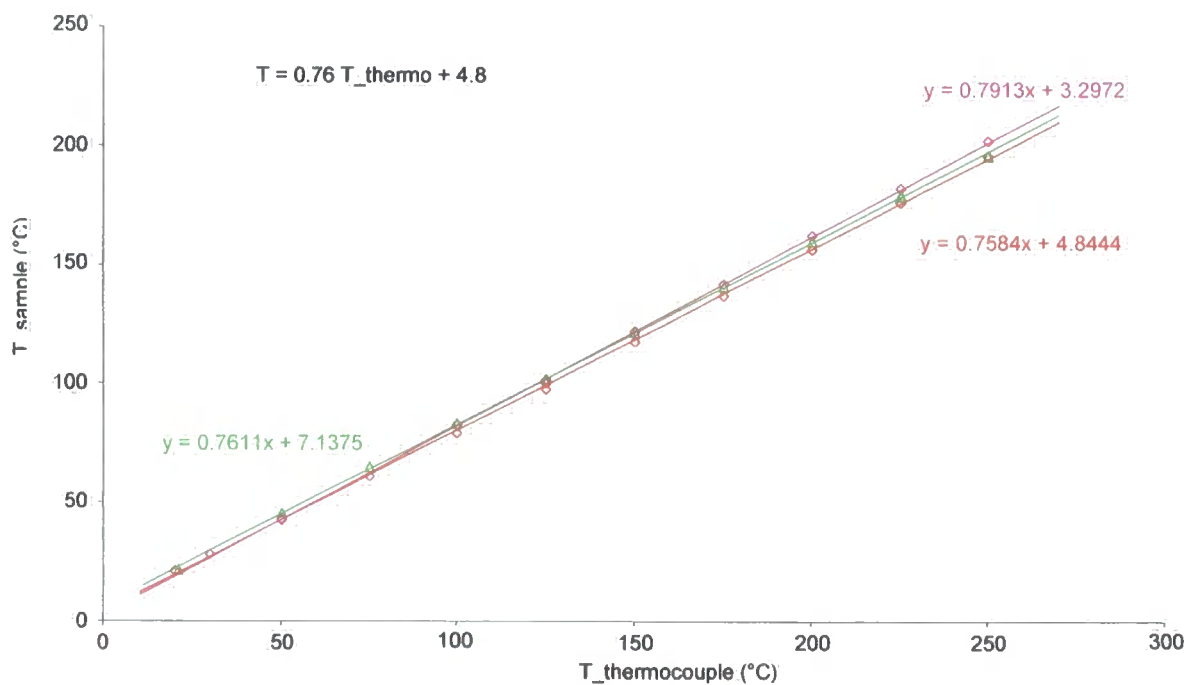
Appendix 2

Temperature calibration curve for variable temperature XRD experiments on the Bruker D5,

calculated using Al_2O_3.
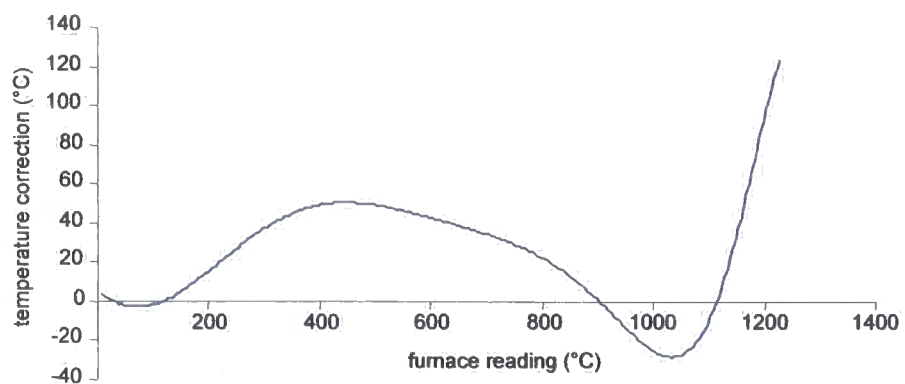
Appendix 3

2D MAS NMR pulse sequence files to use on a Bruker spectrometer.

RFDR

```
; 2D MAS exchange experiment with RFDR sequence during the mixing time
; to promote magnetization transfer though dipolar interaction.
; 12 loop counter for mixing time (Tmix=12*8*Trot).
; use define saturation for saturation loop
; use define rfdr for rfdr pulses during mixing time
;ns=8*n

"l1=td1/2"

"p2=2*p1"

"d6=16*1s/cnst31-p2/2"          ; Z-filter delay
"d7=0.5s/cnst31-p2/2-3u"        ; calculation of delay d7 and d8 between
180° pulse
"d8=1s/cnst31-p2-3u"            ; from the MAS frequency cnst31

#define saturation
#define rfdr
#define twoD

        ze                      ; clear data
10u     pl1:f1                  ; power level pl1
2       150u                    ; saturation loop
#ifdef saturation
        3u:f1 ph0
        p1:f1 ph0
        lo to 2 times 120
#endif
        d1                      ; recycle delay
        3u:f1 ph1
        p1 ph1                  ; 90° pulse (power level pl1)
        d0                      ; t1 time increment (starting with
d0=3u)
        2.5u:f1 ph3
        p1 ph3                  ; 90° pulse (power level pl1)
        d6                      ; Z-filter
#ifdef rfdr
3       d7
        3u:f1 ph5
        p2 ph5                  ; 180° pulse
        d8
        3u:f1 ph6
        p2 ph6                  ; 180° pulse
        d8
        3u:f1 ph5
        p2 ph5                  ; 180° pulse
        d8
        3u:f1 ph6
        p2 ph6                  ; 180° pulse
        d8
        3u:f1 ph6
        p2 ph6                  ; 180° pulse
        d8
        3u:f1 ph5
        p2 ph5                  ; 180° pulse
        d8
        3u:f1 ph6
        p2 ph6                  ; 180° pulse
```

```
        d8
        3u:f1 ph5
        p2 ph5                     ; 180° pulse
        d7
        3u
        lo to 3 times l2
#endif
        d6:f1 ph4                  ; Z-filter
        p1 ph4                     ; 90° pulse (power level pl1)
        2u
        1u:f1 ph0
        2u
        1u adc ph31                ; start ADC with ph31 signal routing
        aq                         ; allow time for data sampling
        rcyc=2                     ; do NS scans
#ifndef twoD
  wr #0
#else
        30m wr #0 if #0 zd
        ip1                        ; increment phase ph1 by 90° for
Cosine/Sine part (States)
        lo to 2 times 2
        rp1                        ; reset phase ph1
        id0                        ; time increment and loop
        lo to 2 times l1
#endif
exit

ph0= 0
ph1= 0 2
ph3= 0
ph4= 0 0 1 1  2 2 3 3
ph5= 0
ph6= 1
ph31= 0 2 1 3  2 0 3 1
```

POST-C7

```
;POSTC7 pulse sequence for double quantum correlation spectroscopy
;power level pl11 for POSTC7 should match the rotary resonance
;condition : RF field frequency = 7* MAS frequency
;phase preset time = 0.35u
;120 loop counter for saturation loop
;12 loop counter for POSTC7 cycles
;cnst31 = MAS frequency
;States acquisition of the 2D dataset to obtain pure phase 2D spectrum
;ns 16*n

"l0=td1/2"

define loopcounter C7
"C7=7*12"

define pulse tau15                    ;calculation of pulse length
"tau15=((1s/cnst31)/7.0)-0.9u"        ;using the MAS frequency cnst31
define pulse tau14
"tau14=(tau15)/4.0"
define pulse tau16
"tau16=(3.0*(tau15))/4.0"

#include <solids.incl>

;*****************************
;*** Acquire Cosine part *****
;*****************************

1       ze                            ; clear data
        1m rp5                        ; reset phases
        1m rp11
        1m rp12
        1m rp13
        1m rp30
        1m rp31
        10u pl1:f1
        10u reset:f1
2       150u                          ; saturation loop
        1.8u:f1 ph0
        p1:f1 ph0
        lo to 2 times 120
        d1 protect                    ; recycle delay
        1.8u pl11:f1                  ; set power level pl11 for POSTC7

3       1.8u:f1 ph11^                 ; phase increment by step of
(360°)/7 (0Q->2Q excitation)
        tau14:f1 ph1                  ; 90° pulse (power level pl11)
        tau15:f1 ph2                  ; 360° pulse (power level pl11)
        tau16:f1 ph1                  ; 270° pulse (power level pl11)
        lo to 3 times C7
        d0                            ; t1 evolution (starting with
d0=3u)
4       1.8u:f1 ph12^                 ; phase increment by step of
(360°)/7 (2Q->0Q)
        tau14:f1 ph3                  ; 270° pulse (power level pl11)
        tau15:f1 ph4                  ; 360° pulse (power level pl11)
        tau16:f1 ph3                  ;  90° pulse (power level pl11)
        lo to 4 times C7
```

```
        d3 pl1:f1                    ; set power pl1 for observe
        3u:f1 ph6
        1.8u:f1 ph5
        p1:f1 ph5                    ; 90° pulse (power level pl1)
        2u
        1u:f1 ph0
        2u
        1u adc ph30                  ; start ADC with ph30 signal routing
        aq                           ; allow time for data sampling
        1m rpp11                     ; reset phase ph11 and ph12 pointers
        1m rpp12
        1m ip11*900                  ; increment ph11 by step of 90°(phase
cycling)
        rcyc=2                       ; do NS scans
        10m wr #0 if #0 zd           ; write file


;*************************
;*** Acquire Sine part *****
;*************************

5       ze                           ; clear data
        1m rp5                       ; reset phases
        1m rp11
        1m rp12
        1m rp13
        1m rp30
        1m rp31
        10u pl1:f1
        10u reset:f1
        1m ip12*450                  ; shift ph12 45 degree
6       150u
        1.8u:f1 ph0
        p1:f1 ph0
        lo to 6 times 120            ;saturation loop
        d1 protect                   ; recycle delay
        1.8u pl11:f1                 ; set power level for POSTC7
7       1.8u:f1 ph11^                ; 2Q excitation
        tau14:f1 ph1
        tau15:f1 ph2
        tau16:f1 ph1
        lo to 7 times C7
        d0                           ; t1 evolution
8       1.8u:f1 ph12^                ; 2Q reconversion
        tau14:f1 ph3
        tau15:f1 ph4
        tau16:f1 ph3
        lo to 8 times C7
        d3 pl1:f1                    ; set power level pl1 for observe
        3u:f1 ph6
        1.8u:f1 ph5
        p1:f1 ph5                    ; 90° pulse
        2u
        1u:f1 ph0
        2u
        1u adc ph31                  ; start ADC with ph31 signal routing
        aq                           ; allow time for data sampling
        1m rpp11                     ; reset phase ph11 and ph12 pointers
        1m rpp12
        1m ip11*900                  ; shift ph11 90 degree (phase cycling)
        rcyc=6                       ; do NS scans
        10m wr #0 if #0 zd           ; write file
```

```
        id0                     ; t1 increment

        lo to 1 times 10   ; t1 loop increment

exit

ph0= 0
ph1= +x
ph2= -x
ph3= +x
ph4= -x
ph5= 0 0 0 0 1 1 1 1 2 2 2 2 3 3 3 3
ph6= +x
ph11=(3600)     0   514 1029 1543 2057 2571 3086
ph12=(3600)   900 1414 1929 2443 2957 3471  386
ph30= 2 0 2 0 3 1 3 1 0 2 0 2 1 3 1 3
ph31= 0 2 0 2 1 3 1 3 2 0 2 0 3 1 3 1
```

POST-C9

```
; 2D exchange experiment with POSTC9 sequence during the mixing time
; to promote magnetization transfer though isotropic J-coupling.
; use phase preset time of 0.35u
; use #define saturation for saturation loop
; use #define POSTC9 for POSTC9 sequence during mixing time
; use #define TwoD for 2D correlation
; optimisation of power level pl11 to match the rotary resonance
; condition (RF field frequency = 6* MAS frequency) with 1D version
; 12 : number of C9 cycles
; d0=0.5u
; cnst31 = MAS frequency
; States acquisition of the 2D dataset to obtain pure phase 2D
spectrum
;ns 8*n
;--------------
; wl = 6*wr
;--------------


"l1=td1/2"

define loopcounter C9
"C9=9*12"

define pulse tau12                      ;calculation of pulse length using
the MAS frequency cnst31
"tau12=((1s/cnst31)/6.0)"       ; 360° pulse
define pulse tau11
"tau11=(tau12)/4.0"             ;  90° pulse
define pulse tau13
"tau13=((3.0*(tau12))/4.0)-1.8u"   ; 270° pulse - p18

"p18=1.8u"

#define saturation
#define POSTC9
#define twoD


        ze
10u     reset:f1
10u     pl1:f1                  ; power level pl1
2       150u
#ifdef saturation               ; saturation loop
        3u:f1 ph0
        p1:f1 ph0
        lo to 2 times 120
#endif
        d1                      ; recycle delay
        3u:f1 ph1
        p1 ph1                  ; 90° pulse (power level pl1)
        d0                      ; t1 time increment (starting with
d0=3u)
        2.5u:f1 ph2
        p1 ph2                  ; 90° pulse (power level pl1) store
magnetization along Z axix
        2u
#ifdef POSTC9
        1.8u pl11:f1            ; set power level pl11 for POSTC9
```

```
        1.8u:f1 ph0
3       tau11:f1 ph4                    ; 90° pulse (power level pl11)
        tau12:f1 ph5                    ; 360° pulse (power level pl11)
        tau13:f1 ph4                    ; 270° pulse (power level pl11)
        p18:f1 ph11^                    ; increment ph11
        lo to 3 times C9
#endif
        1.8u pl1:f1                     ; set power level pl1 for observe
        3u:f1 ph6
        1.8u:f1 ph3
        p1:f1 ph3                       ; 90° pulse (power level pl1)
        2u
        1u:f1 ph0
        2u
        1u adc ph31                     ; start ADC with ph31 signal routing
        aq                             ; allow time for data sampling
        1m rpp11                        ; reset phase ph11 pointer
        rcyc=2                          ; do NS scans
#ifndef twoD
  wr #0
#else
        30m wr #0 if #0 zd
        1m ip1                          ; increment phase ph1 by 90° for
Cosine/Sine part (States)
        lo to 2 times 2
        1m rp1                          ; reset phase ph1
        id0                             ; t1 time increment and loop
        lo to 2 times l1
#endif                                  ; twoD
exit


ph0= 0
ph1= 0 2
ph2= 0
ph3= 0 0 1 1  2 2 3 3
ph4= +x
ph5= -x
ph6= +x
ph11= (3600) 400 800 1200 1600 2000 2400 2800 3200 0
ph31= 0 2 1 3  2 0 3 1
```

refocused-INADEQUATE

```
; Refocused INADEQUATE 2D
; 2D states
; p1 : 90 degree pulse
; p2 : 180 degree pulse
; l20 saturation loop
; d10 about 4ms to be optimised
; cnst31 spinning frequency

"l1=td1/2"
"p2=2*p1"
"d10=l10*(1.0s/cnst31)-p1/2-p2/2"

#define saturation
#define twoD

#include <solids.incl>

1       ze
        10u reset:f1
        10u pl1:f1
2       250u
#ifdef saturation
        3u:f1 ph0
        p1:f1 ph0
        lo to 2 times l20
#endif                              ; saturation
        d1
        p1:f1 ph1
        d10
        (p2 ph2):f1
        d10
        (p1 ph3):f1
        d0
        (p1 ph4):f1
        d10
        (p2 ph5):f1
        d10
        go=2 ph31
#ifndef twoD
        wr #0
#else                       ;twoD
        30m wr #0 if #0 zd
        1m ip1
        1m ip2
        1m ip3
        lo to 2 times 2
        1m rp1
        1m rp2
        1m rp3
        id0
        lo to 2 times l1
#endif
exit

ph0=0
ph1= (8) 0 2 4 6
ph2= (8) 2 4 6 0  4 6 0 2  6 0 2 4  0 2 4 6
ph3= (8) 0 2 4 6
```

```
ph4=1
ph5=0
ph31= 0 2 0 2 2 0 2 0
```

Appendices 4 and 5

A Topas input file for the ZrP_2O_7 structure and a .cif file for the 2-[4-(2-hydroxy-ethylamino)-6-phenylamino-[1,3,5]triazin-2-ylamino]-ethanol structure are given on the CD on the inside of the back cover of this thesis.